FROM UNDERSTANDING TO BIOMIMICKING OF STRUCTURAL COLOR

DIAO YINGYING

(B. Sc, SHANDONG UNIV)

A THESIS SUBMITTED

FOR THE DEGREE OF DOCTOR OF PHILOSOPHY

DEPARTMENT OF PHYSICS

NATIONAL UNIVERSITY OF SINGAPORE

(2012)

DEDICATION

To my beloved parents and fiancé

ACKNOLEDGEMENTS

I would like to take this opportunity to acknowledge all the help, supports, discussions, and encouragements I have received while working on my thesis.

First and foremost, I would like to express my deepest and sincere gratitude to my supervisor, Prof. Liu Xiang-Yang, for his constant support, help and guidance over the past four and half years. This work would not have been possible without his persistent guidance and help. Prof. Liu's wide knowledge and his logical way of thinking help me to learn from nature and to develop many of ideas of this study. His encouragement and personal help have offered me the most valuable support throughout my PhD life, and have given me the enough courage to face the challenges during my study. He also reviewed and revised all my manuscripts word by word with greatest diligence and patient. I could not expect a better advisor and mentor for my PhD work.

In the course of my research, I have had the opportunity to interact with many people, and learn a lot from each other. Here, I would like to thanks Dr. Liu Ruchuan, who helped me a lot in the beginning of my research, as well as all my colleagues and friends Mr. Teo Hoon Hwee, Sin Yin, Du Ning, Tianhui, Rongguo, Guobin, Shaokun, Wanglei, Zhou Hu, Li Yang, Wang Hui, Linda, Zhiqiang, Yuan Bing, Hu Wen, Xiaodan, Gangqin, Wu Xiang, Yang Zhen, Andy, William, Tuan, Viet, Gongli, Desuo, Naibo, Jiafeng, Boyou, Wengong, Liyong, Xiaqing, Xiaoma, Xinjun, Hongzhi, Wangqian, Guanggeng. I am also very grateful to Dr. Shi Lei for giving me a lot of advices and practical instruction about my project.

I am indebted to my parents, older sister and younger brother for their deepest love and support throughout my life. My parents have always done their best to support and encourage me since I can remember. I am deeply grateful to my older

sister, she has not only taken the duty to take care of my parents but also care me a lot in these years. My younger brother's trust gives me a lot of courage to pursue my dream. I would like to give my special thanks to my beloved fiancé, YuZhan, for his love and help during the last two and half years.

Last but not least, I would like to express my acknowledgement to National University of Singapore for offering the scholarship to support my study.

LIST OF PUBLICATIONS

- *Mysterious coloring: structural origin of color mixing for two breeds of Papilio butterflies*
  Ying Ying Diao and Xiang Yang Liu
  OPTICS EXPRESS, **9**, 9232-9241 (2011)

- *Controlled colloidal assembly: experimental modeling of general crystallization and biomimicking of structural color (Feature Article)*
  Ying Ying Diao and Xiang Yang Liu
  ADVANCED FUNCTIONAL MATERIALS, **22,** 1354-1375 (2012)

- *Mimicking of bi-structural-color reflection*
  Ying Ying Diao, Xiang Yang Liu, Toh Guoyang William, Lei Shi and Jian Zi
  ADVANCED MATERIALS, Under Review

- *Switching on fluorescent emission by molecular recognition and aggregation dissociation*
  Naibo Lin, Xiang Yang Liu, **Ying Ying Diao**, Hongyao Xu, Chunyan Che, Xinhua Ouyang, Hongzhi Yang and Wei Ji
  ADVANCED FUNCTIONAL MATERIALS, **22**, 361-368 (2012)

- *Bring structural color to silk fabrics*
  Ying Ying Diao and Xiang Yang Liu
  ADVANCED MATERIALS RESEARCH, **442**,183-186 (2012)

- Modeling of Biomineralization and Structural Color Biomimetics by Controlled Colloidal Assembly in Bioinspiration: from nano to micro scales
  Xiang Yang Liu and **Ying Ying Diao** (in press)

- *Light-reflective structures and methods for their manufacture and use*
  Xiang Yang Liu and **Ying Ying Diao**
  SG - 810110-01-SG-PCT (2011)

- *Inverse opal structures and methods for their preparation and use*
  Xiang Yang Liu and **Ying Ying Diao**
  SG - 821277-01-US-REG (2012)

- *Fabrication of highly-ordered P3HT:PCBM nanostructures and its application as supercapacitive electrode*
  Yu Zhan Wang, Qian Wang, Hao Yu Xie, Li Peng Ho, Desmond Meng Fong Tan, **Ying Ying Diao**, Wei Chen and Xian Ning Xie
  NANO SCALE, 4, 3725-3728 (2012)

Table of Contents

ABSTRACT

Structural color caused by the interaction of light with nanoscale periodic structure, so-called photonic crystals, has attracted considered attention in a variety of research areas. Structural color is usually iridescent and metallic; moreover, it is brighter, more deeply saturated, free from photobleaching, and longer lasting, unlike traditional pigments or dyes. In the biological world, the colorful feathers of many birds (i.e. peacock), the wings of various butterflies and the elytra of many beetles are good examples of structural color. During the last two decades, many efforts have been devoted to mimicking natural structural color. However, the structural color produced by nature is much richer and more effective than we can produce so far. In this thesis, we focused to study some unique optical properties of natural structural color and invent new and effective methods to mimic structural color.

The structural origin of the coloration mechanisms and related extraordinary optical properties of the wing scales of two breeds of *Papilio* butterflies, namely *Papilio Ullysess* and *Papilio Blumei*, are explored. The precise ordered biophotonic nanostructures of the wing scales are characterized by scanning electron microscopy (SEM). Despite their structural similarities, the two breeds of *Papilio* butterflies do not exhibit any analogy in their optical performances. When illuminated with UV-Vis light, *P.Ullysess* gives rise to two reflection peaks, one is from concavities and the other is from ridges. These two spectral peaks shift their positions under different illumination angles (normal and 45^{o} incident light). In contrast, the spectra for the green scales of *P.Blumei* give one broad reflection peak, and the peak keeps the same under normal and 45^{o} incident light. The

optical microscopy images indicate that the cap shaped concavities on *P.Blumei*'s wing scales generate an abnormal bi-color reflection with strong polarization effect. Both of these two breeds of butterflies take advantage of colors mixing strategy: the blue color of *P.Ullysess* is mixed by the colors reflected from concavities and ridges; the green color of *P.Blumei* is produced by the biocolor reflection from concavities. The differences of their coloration mixing mechanisms and optical performances are due to the variations of their nanostructures. The investigation of the bi-structural-color mechanisms of these biologically photonic nanostructures may offer a convenient way for fabricating optical devices based on biomimicry. Besides of vivid structural color, ultra-black scales also appear in the butterfly wings. It is found that the complex nano-structures of the black wing scales assist its light absorption.

The bi-structural-color reflection may serves as mating and communicating signal in butterfly kingdom. Evidently, the construction of an effective and simple way to produce bi-structural-color reflection covering UV, visible and infrared ranges simultaneously may point to a new direction in multi-functional photonic materials engineering. Although the mimicking of bi-structural-color reflection has been reported, the fabrication was involved with a process of combined layer deposition techniques, which is complicated and less flexible. In this thesis, we report on the mimicking of bi-structural-color based on silk fibroin using a simple and inexpensive self-assembly method. Silk fibroin photonic crystals with inverse opal structure are fabricated through a colloidal crystal templating method. By taking advantage of the two photonic band gaps of the inverse opal structure, silk fibroin inverse opals with different spectral positions of bi-structural-color reflection (i.e. ultraviolet and visible peaks, ultraviolet and near infrared peaks, and

visible and near infrared peaks) are obtained by simply controlling their lattice constants. We also invent a new technology to construct photonic crystals on the surface of silk fabrics to demonstrate the potential applications of structural color in eco-dyeing and multi-functional silk fabrics.

The two reflection peaks of silk fibroin inverse opals are tuned by changing the lattice constants, however, for a ready-made inverse opal, tuning the reflection peaks is an issue. The in-line and continuous tuning of the peak positions of bi-structural-color reflection of a ready-made inverse opal is achieved by the humidity induced cyclic contraction of silk fibroin.

The understanding of structural origin of natural bi-structural-color reflection has broad biological implications, and the mimicking of bi-structural-reflection using silk fibroin would have potential applications in bio-coating materials, biomedical and cosmetic applications. Especially, the humidity responsive silk photonic crystal may find great opportunities as active color units in the fabrication of flexible display media in the future.

Organic fluorescent dyes-based biological devices are used widely for measurements in optoelectronic, life-science research, drug discovery and materials coating. It is desirable to identify and effective way to dynamic control the fluorescence emission. To achieve this, the fluorescent emission of Rhodamine 6G is dynamically controlled by combing the dyes into silk fibroin inverse opals. The fluorescence emission can be strongly enhanced by coupling the emitters into inverse opal structure. Moreover, the fluorescence enhancement increases linearly with the increscent of the thickness of the inverse opals (the NO. of layers) with a factor of 2. By adjusting the band gaps of the photonic crystals to overlap the fluorescence emission spectrum, the fluorescence emission is inhibited. Due to the

high promising property of silk fibroin in the field of bio-technology, the combination of fluorescent dyes and silk fibroin photonic crystals broaden applications of fluorescent dyes in biological systems. Such a fluorescence enhancement and inhibition mechanism controlled by biomaterial would be invaluable to the future design in biomedical devices.

LIST OF TABLES

LIST OF FIGURES

LIST OF ABBREVIATIONS

1D	One Dimension
2D	Two Dimension
3D	Three Dimension
PC	Photonic Crystal
PBG	Photonic Band Gap
EM	Electron Microscope
SEM	Scanning Electron Microscope
PS	Polystyrene
CRT	Cathode Ray Tube
TMM	Transfer Matrix Method
FDTD	Finite Difference Time Domain
FCC	Face-Centered Cubic
PWE	Plane Wave Expansion
TEM	Transmission Electron Microscope
UV	Ultra Violet
IR	Infra Red
FFT	Fast Fourier Transformation
VIS	Visible
ALD	Atomic Layer Deposition
RPC	Responsive Photonic Crystal
RH	Relative Humidity
FRET	Fluorescence Resonance Energy Transfer
PFE	Photoinduced Fluorescence Enhancement
SPR	Surface PlasmonResonance
P. Ullysess	Papilio Ullysess
P. Blumei	Papilio Blumei

CHAPTER 1

Introduction

1.1 What is structural color?

Color production in nature takes advantage of either pigmentation or structural coloration. Color produced from pigmentation is also called chemical color, which comes from the selectively absorbed certain wavelengths of light and reflected or scattered other wavelengths by pigments. Structural color, also called physical color, is caused by complicated interaction between light and microstructures with featured sizes comparable to the visible wavelengths. In this case, fundamental optical processes such as reflection, refraction, interference, diffraction and scattering are the basic physical originations of structural color.

The phenomenon of structural color has been discovered for a long time, and many efforts have been devoted to identify the optical properties and coloration mechanisms. Probably, the oldest scientific description on structural color appeared in "Micrographia" written by Hooke (1665)[1]. Later, Newton (1704) described in "Opticks" that the colors of iridescent peacock arose from the thinness of the transparent part of feathers[2]. The complete understanding of the concept was accessible after the invention of the electron microscope (EM), with which the dedicated nanostructures of the structural color can be observed. Thus, the relationship between the nanostructures and optical properties of structural

color can be established, and the coloration mechanisms are much easier to understand.

Compared with the colors arise from pigments, structural color possesses many interesting features since it is produced structurally. Generally, structural color is of high brightness and saturation and is hence sometimes called metallic color. It may display iridescence[3], i.e., a color changes as the angle of view or illumination. The variations of structures or contrast of refractive indices may alter or destroy structural color, which can be achieved by applying pressure or infiltrating liquids in air voids of the nanostructures. In contrast to pigmentary coloration, structural color never fade away provided that the corresponding photonic structure retain unchanged.

In recent years, structural color and relevant photonic structure have been subjected to extensive studies because of their scientific and practical importance[3-10]. The study of structural color may render tremendous important information related from evolution, biological functions, structural formation, to strategies of light steering. On the other hand, structural color may have potential applications in a variety of industries including photonics, display, painting, and textile, *etc.* Natural photonic structures and the ingenious ways of color production may have been a great source of inspiration in our design and fabrication of new optical materials and devices for future technological applications.

1.2 Mechanisms of structural coloration

Nowadays, most of the structural colors in nature are considered to originate from the following four fundamental optical processes: 1) interference, 2) diffrac-

tion, 3) scattering and 4) photonic crystals. Herein, we will describe the principles of these optical processes.

1.2.1 Interference

Thin-film interference is one of the simplest structural coloration and is widely distributed in nature[11]. A soap bubble in sunlight is a common example. Consider a light beam is incident on a thin layer of thickness d and refractive index n at the angle of θ as shown in Fig. 1.1a. The light beam is either reflected or transmitted at the upper surface. The transmitted beam at the upper surface will once again be reflected or transmitted when reaching the lower surface. The reflected beam at the lower surface will also encounter reflection or transmission at the upper surface. Then the reflected light beams from the two surfaces would interfere with each other. The optical path difference for the two reflected light beams depends on the incident angle θ, the film thickness d and the refractive index of the film n, given by $2ndcos\theta$. In the calculation of the optical path difference, one should consider an abrupt phase change of π when a light beam is reflected from a low-refractive-index medium to a high-refractive-index medium; in this case, an extra contribution $\lambda/2$ should be calculated to the optical path difference. Constructive interference occurs when the optical path difference is an integral number of wavelengths. On the other hand, destructive interference happens when the optical path difference is a half integral number of wavelengths. Considering phase changes upon reflection at both the upper and lower surfaces, the condition for constructive interference for $n_1 < n < n_2$ or $n_1 > n > n_2$ is given

$$2nd \cos\theta = m\lambda \qquad (1.1)$$

where λ is the light wavelength in vacuum, n_1 and n_2 are the refractive indices of the upper medium and lower medium, respectively, m is an integer. For $n_1 < n > n_2$ or $n_1 > n < n_2$, the condition for constructive interference of a thin film becomes

$$2nd \cos\theta = (m + 1/2)\lambda \qquad (1.2)$$

For a given film, the reflection reaches its maximum when the wavelengths satisfying the above constructive interference conditions, giving rise to structural coloration. From equations *1.1*&*1.2*, it is obvious that the optical path difference increases with increasing incident angle. As a result, the wavelengths of reflection peaks undergo a blue shift when increasing the incident angle, leading to iridescent structural coloration.

Multilayer interference is qualitatively understood as the case where a pair of thin layers piles up periodically. Consider two layers designated as *A* and *B* with thicknesses d_A and d_B and refractive indices n_A and n_B, respectively (Fig. 1.1b). We assume $n_A > n_B$ for the present. If we consider a particular pair of layers, the phases of the reflected light both at the upper and lower interfaces between *B* and *A* change by π. Thus, multilayer interference, as in thin-film interference, can be applied as *Eq. 1.3* for constructive interference, with the angles of refraction in layers *A* and *B* as θ_A and θ_B, respectively.

$$2 (n_A d_A \cos\theta_A + n_B d_B \cos\theta_B) = m\lambda \qquad (1.3)$$

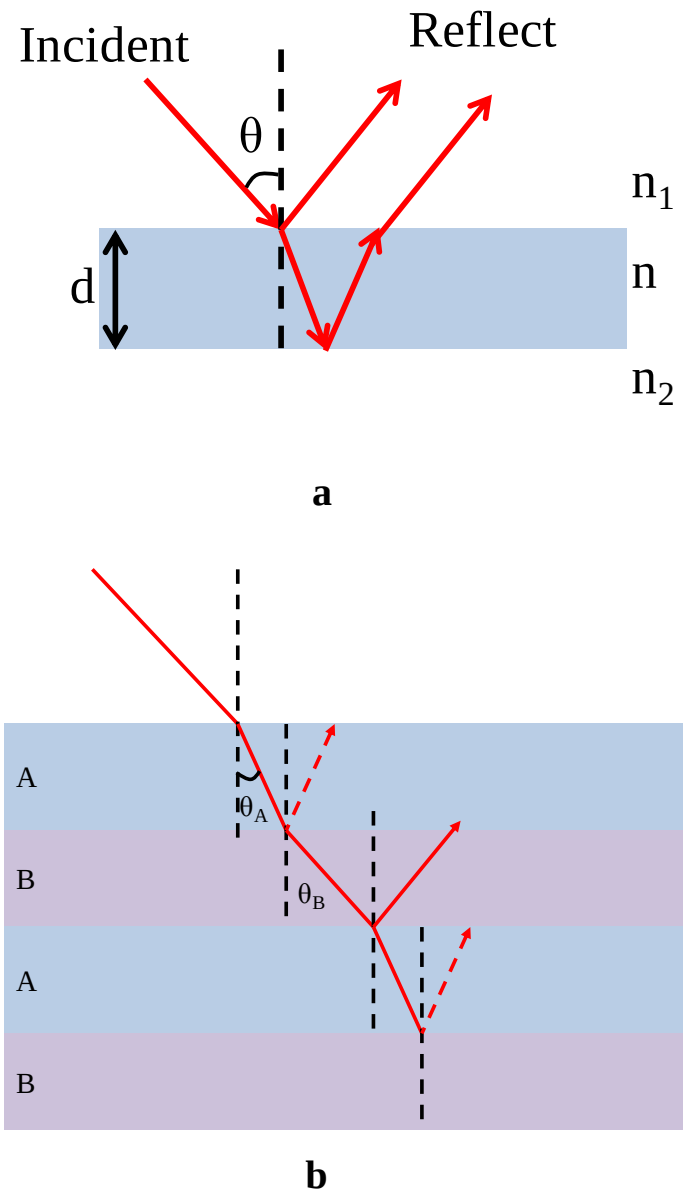

Figure 1.1. a Thin-film interference. A thin-film with a thickness of d and refractive index of n is sandwiched between a upper medium with a refractive index of n_1 and a lower medium with a refractive index of n_2. The refracted angle with respect to the surface normal in the thin-film is denoted by θ. b Interference in a multilayer structure.

1.2.2 Diffraction

Diffraction occurs when light waves travel through a medium with a varying refractive index, such as a diffraction grating. A diffraction grating is an optical component with a regular pattern (Fig. 1.2). The form of the light diffracted by a grating depends on the structure of the elements and the number of elements present, but all gratings have intensity maxima at angles θ_m which are given by the grating equation

$$d\ (\sin\theta_i + \sin\theta_m) = m\ \lambda \qquad (1.4)$$

Where θ is the angle at which the light incident, d is the separation of grating elements, and m is an integer which can be positive or negative. For a fixed wavelength, diffraction occurs at certain diffracted angles that satisfies the grating equation. For fixed incident and diffracted angles, light with wavelengths that satisfy the grating equation can be strongly diffracted, leading to coloration.

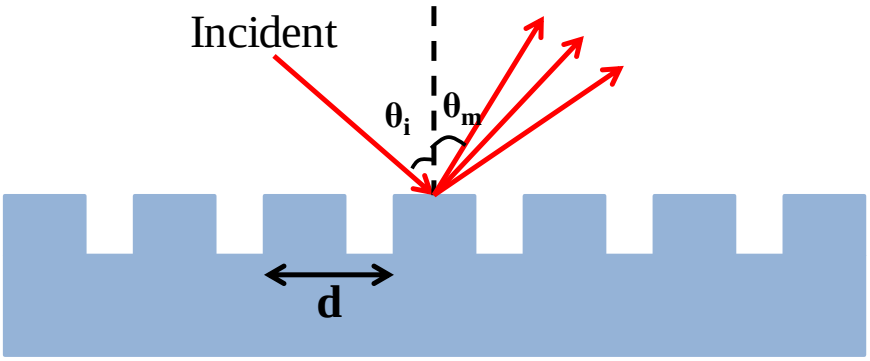

Figure 1.2. Diffraction by a grating consisting of a periodic surface. The incident angle is θ_i, the diffracted angle is θ_m, and the ridge spacing is d.

1.2.3 Scattering

Light scattering is a form of scattering in which light is the form of propagating energy which is scattered. Light scattering can be thought of as the deflection from a straight part, for instance by irregularities in the propagation medium, particles, or in the interface between two medium. Light scattering may strongly depend on the light wavelength, the geometry and the arrangement of the irregularities. According to the arrangements of irregularities, light scattering can be incoherent or coherent, which is determined by the coherent length of illuminating light. For natural light such as sunlight, its coherent length is about a few microns. When the separations of scatters are larger than the coherent length, it can be considered as incoherent scattering. On the other hand, if the separations of scatters are smaller than the coherent length, light scattering is coherent since scattered light may interfere each other and even cause strong resonances. The blue color of the sky is caused by scattering from molecules since shorter wavelength light such as violet and blue is scattered much more that the longer wavelength light.

1.2.4 Photonic crystals

For thin films, multilayers, and diffraction gratings, their coloration can be understood simply by interference and diffraction. In the biological world, there exists much more complicated photonic structures, e.g., periodic photonic structures in two- and three- dimensions (2D/3D), so-called photonic crystals (PCs). Actually, multilayers and diffraction gratings are examples of one dimensional (1D) photonic crystals.

Photonic crystals are composed of periodic dielectric or metallo-dielectric nanostructures that affect the propagation of electromagnetic waves (EM) in the same way as the periodic potential in a semiconductor crystal affects the electron motion by defining allowed and forbidden electronic energy bands. Essentially, photonic crystals contain regularly repeating internal regions of high and low dielectric constants. If the depth of refractive index modulation of photonic crystal is sufficient, a photonic band gap (PBG) can open up. This gives rise to distinct optical phenomena such as inhibition of spontaneous emission, high-reflecting omni-directional mirrors and low-loss-waveguiding, *etc*. When the photonic band gaps of these materials locate in the visible range (400-700nm), the interaction between the light and microstructures will produce the so-called structural color. To understand the coloration mechanism of structural color in a quantitative way, numerical simulations by solving Maxwell's equations must be conducted. The simulation methods will be introduced in Chapter 2.

1.3 Examples of natural structural color

A wide variety of structural colors can be found in nature, among which the most famous examples are the vivid colors of some species of butterfly wings and the peacock feathers[13-17]. Metallic reflection from the elytra of beetles and the iridescent stripe in some kinds of fish are also typical natural structural colors[18-20]. In the following, we will discuss the coloration mechanisms of some examples of natural structural colors.

1.3.1 Butterfly wings

Certain species of butterflies exhibit typical blue and green structural colors, which are known to be produced by the nano-structures in their wing scales[21]. These structures show some variations based on two different central design principles.

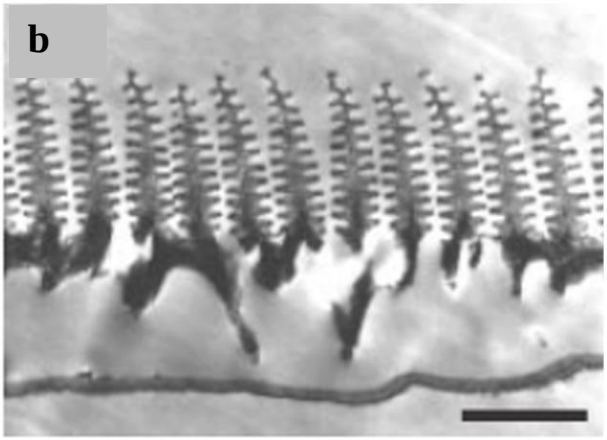

Figure 1.3. a, Real color image of the blue iridescence from a *M. rhetenor* wing. b, Transmission electron micrograph (TEM) image showing the multi-layers structure of the discreate riges on wing-scale of *M. rhetenor* wing (Reproduced from [10]).

The first, named as class 1 or *Morpho* type, comprises of a multi-layer structure within the discrete ridged structures on the surface of scales that cover the wings[6, 22, 23]. *Morpho* butterfly (Fig. 1.3a) bearing brilliant blue color in its wings are the

most suitable creature to explain the complicated features of the structural colors in nature. As shown in Fig. 1.3b, the cross section of a ridge consists of a lamellar structure of 8-10 alternative layers of cuticle and air, which form a multi-layer structure[10]. The iridescent blue color of *Morpho rhetenor* butterfly is attributed to the multilayer interference of the multi-layers of cuticle and air of the ridges on the wing scales.

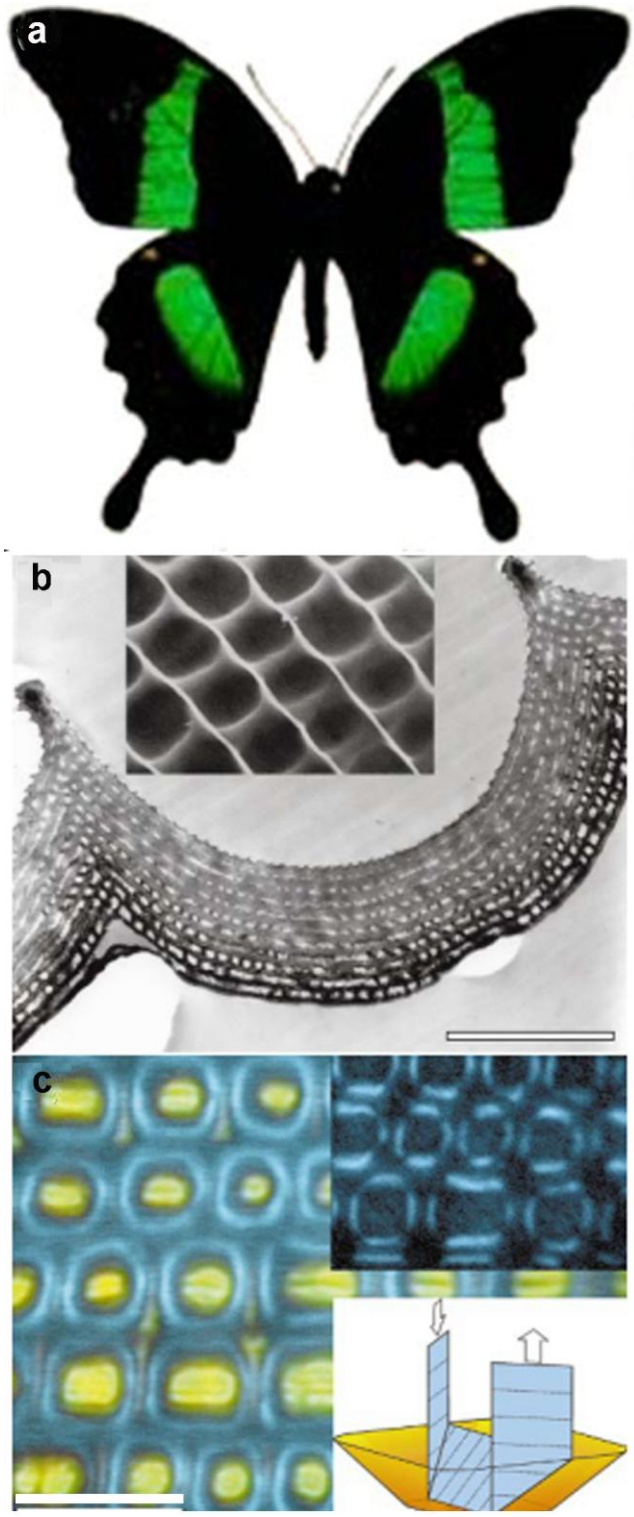

Figure 1.4. Modulated multi-layering leads to dual color in *P. palinurus*. (a), Real color image of the green color from *P. palinurus*. b, TEM image showing a cross section through one concavity on a *P. palinurus* iridescent scale. Inset; a scanning electron microscope (SEM) image of the surface of an iridescent scale. Scale bar, 1 μm. c, Real-color image showing the dual-color nature of the reflectivity from

the surface of the *P. palinurus* iridescent scale, taken using unpolarized light in an optical microscope. Top inset, image of the same region taken with crossed polarizers. Bottom inset, illustration of the mechanism by which polarization is converted through bi-reflection from orthogonal sides of a concavity. Scale bar, 12 μm. (Reproduced from [14])

The second, referred to class 2 or *Urania* type, comprises of continues multi-layers within the body of scales. One particular characteristic of class 2 type is the modulation of the profile of the multi-layer structure, which introduces concave structure into the scale. This specific concave structure can be found in many *Papilio* butterflies, and leads to some particular optical properties, such as polarization, colors mixing *etc*.[14,15] The Indonesian male *Papilio Palinurus* (Fig. 1.4a) butterfly has bright green coloration on its wing scales. Scanning electron micrographs of scales taken from the wings' colored regions show that their surfaces comprise a regular two-dimensional array of concavities, of about 4–6 μm in diameter and 0.5–3 μm at the greatest depth. Transmission electron micrographs of these scales in cross-section reveal that the scales comprises of a multi-layer structure with a concave profile (Fig. 1.4b). The modulation of the concavity generates an extraordinary of both yellow and blue iridescence, the blue component results from so-called retro-reflection process. The variation in color across each concave surface modulation is evident from optical microscopy. In reflection, the flat regions between and in each concavity appear yellow, and the inclined sides of each concavity appear blue under normally incident light (Fig. 1.4c). It is the juxtaposition of these yellow and blue regions that synthesizes the green coloration perceived by the human eye, as they are too small to be resolved individually. Such spatial-averaging color-stimulus synthesis has been reported in beetles, and it also forms the basis of color-television pictures and pointillistic

painting. The blue component cannot be back reflected from a single multilayer system inclined at 45^{o} to the incident direction. The effect is in fact caused by pair of orthogonal multilayer surfaces that lie on opposite sides of each concavity. Light incident along the scale perpendicular, reflected from one surface inclined at 45^{o}, is directed across the concavity to the opposite inclined surface, where it is returned back along the incident direction. These pairs of inclined surfaces with almost identical multi-layering have matched spectral reflectivity characteristics; this causes intense blue reflectivity through this bi-reflection.

1.3.2 Peacock feather

The male peacock tail contains spectacular beauty because of the brilliant, iridescent, diversified colors and the intricate, colorful eye patterns. Peacock feathers (Fig. 1.5a) serve as an excellent canonical example for investigating structural colors in avian feathers. A peacock feather consists of many barbs, each of which has a lot of branches called barbules. Fig. 1.5b is the green barbules under optical microscope. Fig. 1.5c shows the submicron structures of green barbules. The transverse cross sections reveal that a barbule consists of a medullar core enclosed by a cortex layer. Interestingly, the cortex of all different colored barbules contains a 2D photonic-crystal structure[24, 25] made up of melanin rods connected by keratin. Photonic-crystal structures in all different colored barbules are quite similar. In the blue, green, and yellow barbules, the lattice structure is nearly square, whereas in the brown barbules, it is a rectangular lattice. It was found that the cortex in different colored barbules, which contains a 2D photonic-crystal structure, is responsible for the coloration in peacock feathers. Coloration strategies in peacock feather are very ingenious and simple: controlling the lattice

constant and the number of periods in the photonic-crystal structure. Varying the lattice constant produces diversified colors. The reduction of the number of periods brings additional colors, causing mixed coloration.

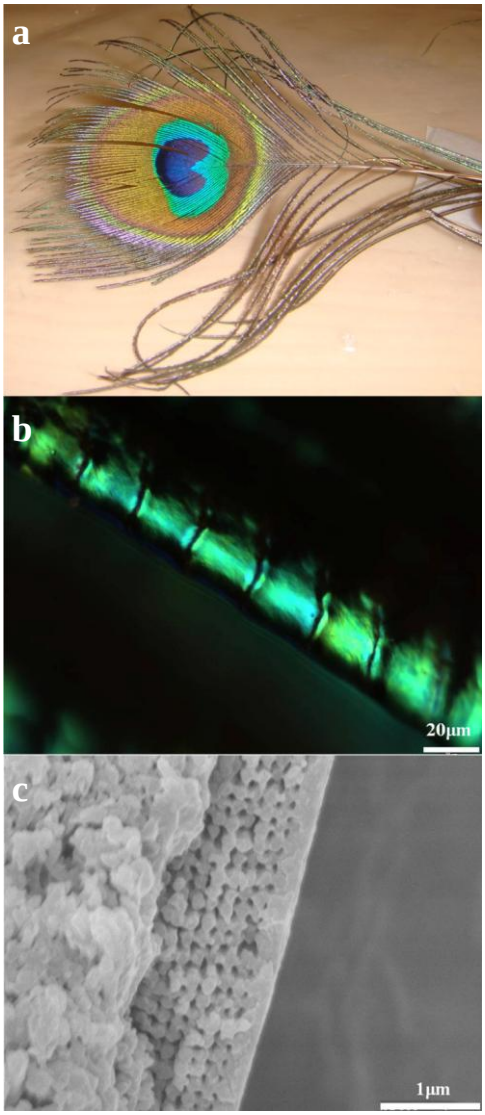

Figure 1.5. Structural color of peacock feather. a Picture of a peacock feather. b Optical microscope image of green barbules. c Scanning electron microscope image of the transverse cross section of green barbules.

1.4 The applications of structural color

Structural color has been closely connected with human life since the dawn of civilization. They have often been used for ornaments and decoration of accesso-

ries and furniture. Pearls are one of the most well-known natural jewels utilizing structural color. In recent years, structural colors have attracted great attention in a wide variety of research fields. One of the reasons is structural colors are deeply connected with rapidly growing fields of photonic crystals.

Photonic crystals attract many research interests from both theorists and experimentalists. These photonic crystal materials present interesting technological applications in photonics and electronics. As one catalog of photonic crystals, structural color materials have been the subject of extensive studies recently, because their applications have rapidly progressed in many fields related to vision such as display technology, cosmetics, and textile industries[26-29]. Arsenault *et al*. described a reflective flat-panel display technology based on the electrical actuation of photonic crystals[27]. These materials display non-bleachable structural color, reflecting narrow bands of wavelengths tuned throughout the entire visible spectrum by expansion and contraction of the photonic-crystal lattice. The material is inherently bright in high-light environments, has electrical bistability, low operational voltage, can be integrated onto flexible substrates, and is unique among all display technologies in that a continuous range of colors can be accessed without the need for color filters or optical elements. Structural color also can be applied in bio-technology, such as cosmetics, textiles, *etc.*

1.5 Strategies of mimicking natural structural color

During the last two decades, considerable efforts have been devoted to mimicking natural structural color[28-38]. However, to obtain such dedicated structures with structural color as seen in animal kingdom remains to be a big challenge. One way to acquire structural color was to adopt the nature structural color materials as

templates to replicate the nanostructures so as to obtain the optical properties[30,31]. Wang *et al.* examined the fine structure of the wing scale of a *Morpho Peleides* butterfly and replicated the entire configuration by a uniform Al_2O_3 coating through a low-temperature atomic layer deposition (ALD) process[30]. An inverted structure was achieved by removing the butterfly wing template at high temperature, forming a polycrystalline Al_2O_3 shell structure with precisely controlled thickness. Other than the copy of the morphology of the structure, the optical property, such as the existence of PBG, was also inherited by the alumina replica. Meanwhile, other replicating methods have also been employed to replicate the structures of natural photonic materials, including conformal-evaporated-film-by-rotation technique, soft lithography technique, etc. [31,38].

Colloidal crystals with photonic band gap lying in the visible range are another option for mimicking natural structural color. Inspired by natural photonic crystals with both structural color and specific wettability, researchers have fabricated colloidal crystals with controllable wettability and tunable structural colors[39-44]. The wettability can be adjusted by the intrinsic roughness of colloidal crystals in combination with the tunable chemical composition of latex surfaces. The structural colors can be tuned by changing the size of the colloidal spheres.

In spite of the easy fabrication and wide potential applications of colloidal crystals, they are very brittle and may disperse in water. Practical device requires that the crystal be either fixed in place or replicated by other more robust materials[45-49]. Alternative approach to mimic natural structural color is to replicate the colloidal crystal structure using a durable material creating inverse opal structure. By adjusting the dimensions of the pores, as well as the refractive index of the material, photonic band gap of the inverse opal structure can be tuned accordingly.

1.6 Motivations, scope and objectives of this thesis

1.6.1 Motivations and objectives

Up to now, the structural coloration mechanisms in nature have been investigated extensively. However, some particular optical properties and their structural originations are not fully understood yet. For instance, the structural color exhibited by *Papilio* butterflies is generally assigned to be iridescent as it is originated from ordered structures. To the best of our knowledge, no further efforts have been made to discuss the influence of *Papilio* butterflies' concavity structure on the angular reflectance property of their structural colors. Furthermore, the ridges on the surface of *Papilio* butterflies' wing scales are rare discussed in the literature.

As described in section 1.5, great accomplishment in mimicking of structural color has been made. However, the structural color produced by the animal kingdom is much richer and more effective than what we can produce artificially so far. Furthermore, it is especially difficult to mimic some unique optical properties of natural structural color, such as polarization, colors mixing etc. M. Kolle *et al.* used combined techniques to fabricate photonic structures with concave and multi-layer structure that mimic the colors mixing and polarization effect found on the colored wing scales of *Papilio Blumei*[34]. Nevertheless, this approach needs to fabricate complex nano-structures, wherein the two reflections come from different parts of the structure. This technique is costly and difficult to obtain different properties by tuning the structure. In this regard, the key challenges in future work to biomimic natural structural color turn out to be how to design and fabricate photonic crystals with the unique optical properties of natural structural color (i.e.

bi-reflection, polarization effect, iridescent/noniridescent *etc*) through a simple process. On the other hand, the growing demand for optical interfaces and sensors for biomedical applications is motivating research towards realizing biocompatible photonic components that offer a seamless interface between the optical and biological worlds. Therefore, another key issue to be addressed in this field is how to mimic the structural color using biocompatible and biodegradable materials.

In the biological world, many animals can change their coloration in response to environmental stimuli. For instance, the elytra golden color of beetles *Tmesisternus isabellae* is produced by a multilayer in scales which are densely imbricated on the elytra[18]. The adaptive values of color change are usually regarded as camouflage, signal communication, conspecific recognition, and reproductive behavior. To bio-mimic the responsive ability of natural structural color is also an interesting topic of our study.

The objectives of this thesis:

1. Explore the mechanisms of color mixing or bi-reflection of natural structural color.
2. Invent an effective way to bio-mimic the double structural color reflection. In this study, silk fibroin with inverse opal structure was chosen to mimic the structural-double-reflection effect.
3. Tune the reflection peaks of a given structural color material by external stimuli to achieve responsive photonic crystals.
4. Apply structural color to fabrics.
5. To further study the light control property of photonic crystals by combining fluorescent molecules into our silk fibroin inverse opals.

1.6.2 Scope of this thesis

In this thesis, we focused on exploring coloration mechanism of the bi-reflection effect of natural structural color and try to identify effective techniques to mimic the bi-reflection using biomaterials based on the understanding of the coloration mechanism of structural bi-reflection, and further to apply structural color in industry field by fabricating structural colored fabrics (Fig. 1.6).

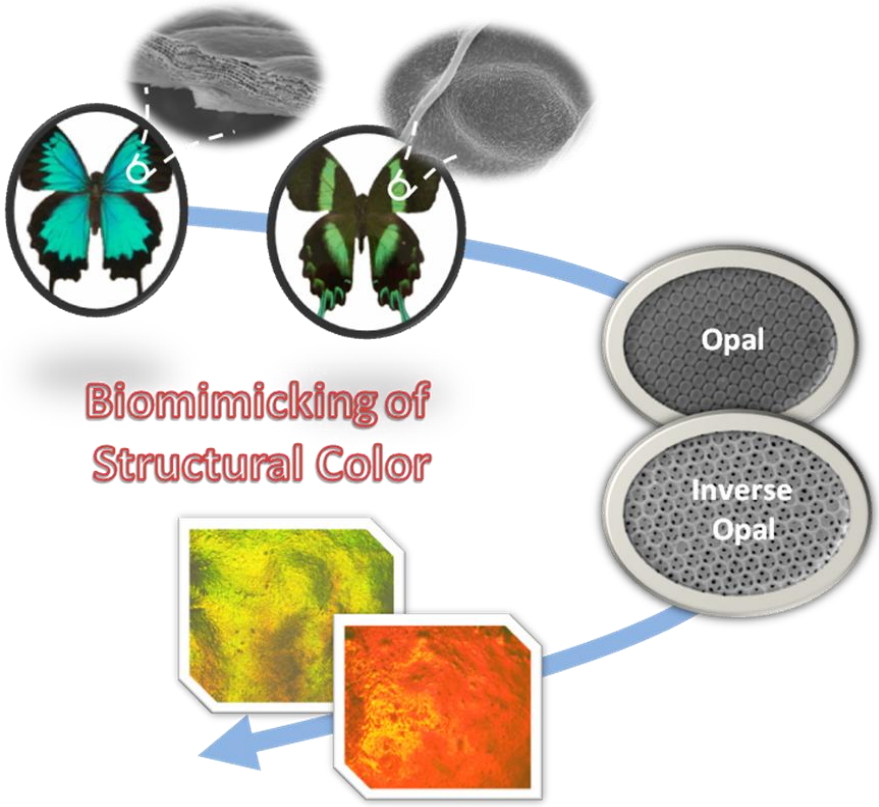

Figure 1.6. Schematic illustration of the scope of this thesis.

In Chapter 2, the fabrication, characterization and simulation methods of photonic crystals with structural color will be introduced. Specifically, evaporation-induced self-assembly method is adopted to fabricate colloidal crystals; silk fibroin inverse opals are fabricated through a colloidal crystal templating method. The optical and spectral properties of structural color are characterized by optical microscope and spectrometer, respectively. The micro-/nano-structures of the

structural color materials are examined by scanning electrom microscope. In this chapter, we will also introduce the plane-wave expansion method to theoretically predict the optical properties of structural color.

In Chapter 3, the coloration mechanisms and related extraordinary optical properties (e.g. polarization, bi-reflection) of the wing scales of two breeds of *Papilio* butterflies, namely *Papilio Ullysess* and *Papilio Blumei*, are explored. Both of these two breeds of butterflies take advantage of colors mixing strategy. The differences of the coloration mixing mechanisms and the optical performances in these two breeds of butterflies will be investigated. The role of the structures of the ridges and the concavities, as well as the profile of the concavities on the colors mixing and polarization effect will be examined. The investigation of the colors mixing mechanisms of these biologically photonic nanostructures may offer a convenient and simple way for fabricating optical devices based on biomimicry.

Chapter 4 will introduce how to mimic natural structural color by fabricating inverse opal structures. Specifically, silk fibroin inverse opals are fabricated to obtain the controllable bi-reflection by taking advantage of the particular characteristics of its photonic band structure. It is our intention to acquire biological materials with structural reflections in both ultraviolet and visible (UV/visible), visible and infrared (visible/IR), or ultraviolet and infrared (UV/IR) ranges of spectrum. Silk fibroin inverse opals with different pairs of bi-reflection peaks (i.e. UV and Visible peaks, UV and NIR peaks or Visible and NIR peaks) are obtained by simply controlling their lattice constants. Furthermore, the potential applications of silk fibroin based photonic crystals in eco-dyeing and multi-functionalizing silk fabrics are also demonstrated.

As discussed in Chapter 4, the two reflection peaks of a silk fibroin inverse opal can be tuned by changing its lattice constant. Nevertheless, for a ready-made silk fibroin inverse opal, adjusting the reflection peaks is a key issue. In Chapter 5, we will identify a simple and effective approach to tune the reflection peaks by external stimuli to achieve responsible structural color. The humidity induced cyclic contraction of silk is utilized to tune peak positions of bi-reflection of silk fibroin inverse opals in an in-line and continuous way.

Chapter 6 studies the light control property of photonic crystals by combing fluorescent dyes Rhodamine 6G (R6G) into silk fibroin inverse opals. We demonstrate that the fluorescence emission could be strongly enhanced by a factor of ~40 by combining the dyes into silk fibroin inverse opals, while within the photonic band gap (PBG) of the inverse opals, the fluorescence emission is inhibited. Therefore, the fully control of fluorescence emission from Rhodamine 6G can be achieved by the inverse opal structure.

Chapter 7 summarizes the results of this thesis and presents overall conclusions as well as recommended further studies that can be undertaken.

CHAPTER 2

Materials, Methods and Techniques

2.1 Materials

Silk is a highly desired textile that has spread throughout the world due to the smooth texture, shimmering appearance and strength of silk have made it. Natural silks derived from spiders or silkworms are the strongest natural fibres known to man and provide an organic alternative to materials such as steel or kevlar [50-52]. Recently, silk fibres obtained from the *Bombyx mori* silkworm are creating new opportunities by offering a widely available, robust, biocompatible and implantable material substrate. Silk fibres from a silkworm cocoon can be processed into various forms, ranging from gels, strands, sponges and blocks, through to foams and films[53-58]. Among the many possible material forms, silk films are of particular interest for optics and photonics applications because of their transparency and surface flatness, which are a direct result of the all-aqueous processing of the protein. In this thesis, silk fibroin films with inverse opal structure are fabricated to mimic natural structural color.

2.2 Methods

2.2.1 Colloidal crystal templates

Before we talk about the fabrication methods of inverse opal structure, we first introduce colloidal crystals, which serve as templates in fabricating silk fibroin inverse opals. Colloidal crystals, wherein the periodic modulation of the dielectric constant is realized by self-assembling mono-dispersed colloidal objects such as silica (SiO_2) or polystyrene (PS) microspheres into ordered arrays, turn out to be an effective approach to photonic crystal preparation[59-62]. The resulting photonic properties are determined not only by the symmetry and lattice constant of the crystal, but also the refractive index contrast between the colloids and the surrounding medium. The sizes of colloids are typically in the range of 100 nm to several μms. The self-assembly and fabrication of two- or three-dimensional (2D/3D) colloidal crystals have attracted intensive interest because their wide applications in photonic crystals[34,63-65], chemical and biochemical sensors[66,67], optoelectronic devices [68,69] and templates for colloidal nanolithgraphy[70]. Here, we focused on the fabrication of 3D colloidal crystals.

Several methods have also been widely employed to assemble highly ordered 3D crystals with large domain size, including sedimentation, repulsive electrostatic interactions, and physical confinement. Among these methods, sedimentation in a gravitational field seems to be the simplest approach for building 3D colloidal crystals[71]. A number of parameters must be carefully controlled to grow colloidal crystals with high quality, including the size, uniformity, and density of the colloids, as well as the rate of sedimentation. The main disadvantages of this method are the poor control over the structure and the thickness of the crystalline

arrays, the long preparation time, and the polycrystalline nature of the products. In the repulsive electrostatic interactions, highly charged colloids particles suspended in a solution can spontaneously self-organize into ordered structures, driven by the minimization of electrostatic repulsive interactions[72-76]. The colloidal crystals prepared using this method are typically non-close-packed, because the repulsive electrostatic interactions keep the particles away from each other. However, this method has very strict requirements regarding the experimental conditions such as the surface charge density, the colloidal concentration, and the ionic strength. In the physical confinement method, the colloidal suspension is left to a physical confinement to self-assemble into long-range-ordered crystalline structures[77-79]. Xia et al. demonstrated an effective way to fabricate colloidal crystals with domain sizes of square centimeters by using a specially designed packing cell[80-82]. This method is relatively fast, and it also provides tight control over the structures and the thickness of the 3D colloidal crystals.

In our study, the colloidal crystals are fabricated through evaporation-induced self-assembly (EISA) method[83,84]. Mono-dispersed polystyrene latex spheres with different diameters were used as received from the supplier (Duke Scientific). Colloidal suspensions are loaded on a silica/glass substrate, and incubate the suspensions inside an oven at 40^{o}C. With the evaporation of the suspensions, colloidal spheres would self-assemble into a 3D colloidal crystal with a face center cubic (FCC) structure (Fig. 2.1). This process is similar with the sedimentation method; the rate of evaporation is well controlled by the temperature.

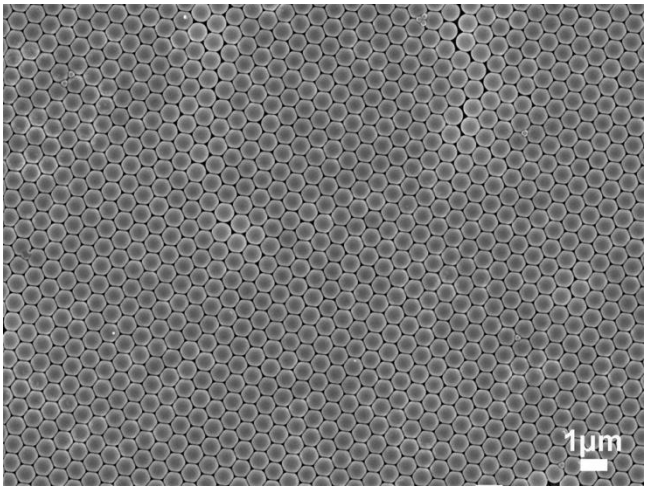

Figure 2.1. Colloidal crystal fabricated by evaporation-induced self assembly methods. The diameter of the colloidal sphere is 700 nm.

2.2.2 Fabrication methods of inverse opal structure

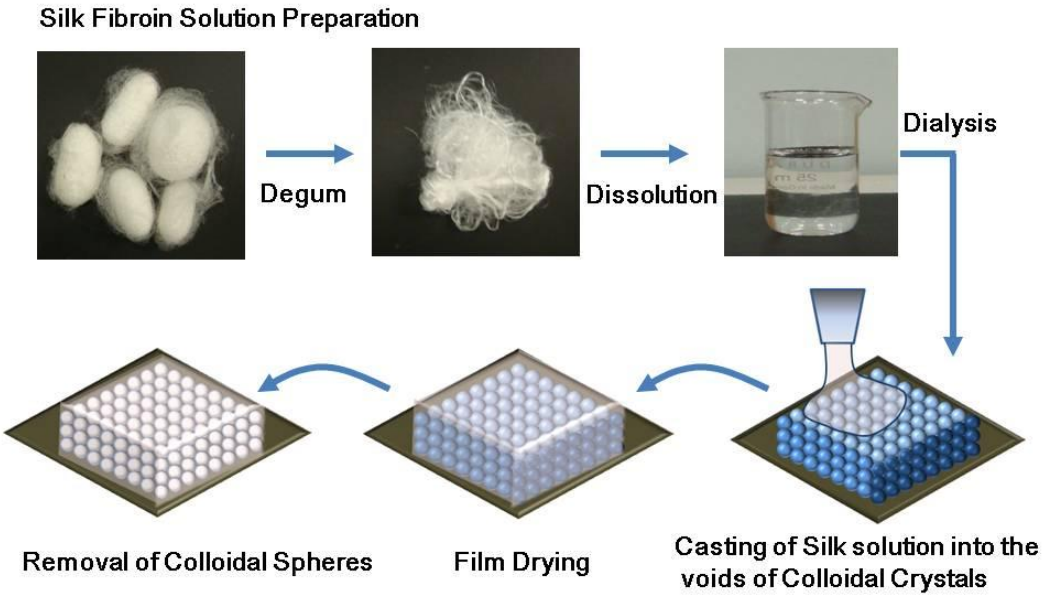

Figure 2.2. The procedures of fabricating silk fibroin inverse opals

In our work, we utilize silk fibroin to fabricate nanoporous materials with highly ordered crystalline structure. The templates we used were 3D colloidal crystals. The regenerated (2% w/v) silk fibroin solution was casted and penetrated into voids of the colloidal crystals by capillary force. The samples were then incubated (25^{o}C, 30% Humility) for 5 Hrs, ensuring the voids in the colloidal crystal were sufficiently filled and allowing the silk fibroin solution to dry slowly. In the third step of the process, PS particles were removed by immerse the samples into tetrahydrofuran (THF, received from Fluke) for 4-5 hrs. And then the samples were taken out to evaporate the THF (Fig. 2.2).

2.3 Experimental characterization techniques

2.3.1 Optical observations

Optical characterizations of structural color are conventionally conducted by optical microscopy under different magnifications. This is because the colored bodies are sometimes too small to be resolved by our naked eye. In some cases, a color perceived us is a mixed one, composed of differently colored small bodies which can be resolved by optical microscopy.

For normal observations, bright field reflection mode is used. We may also use polarization mode to get information on polarization effects of structural color. To characterize the fluorescence emission from a photonic crystal structure, fluorescence mode of optical microscopy is employed. Fig. 2.3 is a typical optical configuration for an optical microscopy.

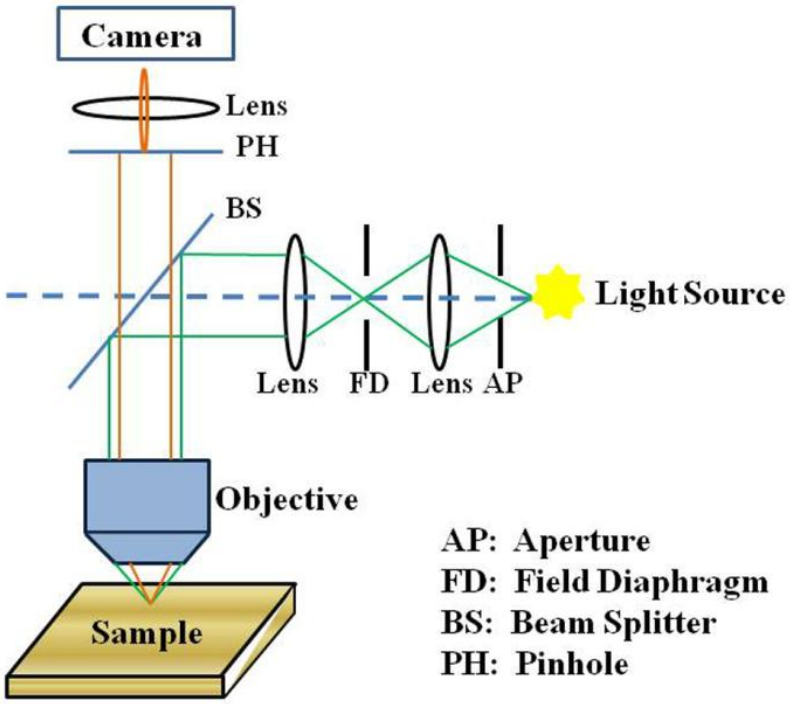

Figure 2.3. Schematic of optical microscopy.

2.3.2 Spectral measurement setup

The spectral characteristics of photonic structures offer important information on structural color. For spectral measurements, spectrometer is highly desirable from which reflection and transmission spectra can be obtained. In this study, ocean optics USB 2000 is employed, as shown in Fig. 2.4a. A home-made angle-resolved spectrometer (Fig. 2.4b) is utilized to characterize the angle-dependent optical properties of structural color. In this angle-resolved spectrometer, the incident angle θ can be adjusted by rotating the detection arm fixed on the lower stage of a rotational stage. Different spectra such as specular reflection (incidence at θ and detection at θ), scattering (incidence at θ and detection at other angles), backscattering (incidence at θ and detection at $-\theta$), and transmission can be obtained. In measurements of absolute reflectance, a reference standard, e.g.,

diffuse white, should be used in order to remove the influence of the characteristic wavelength dependence from the illuminate.

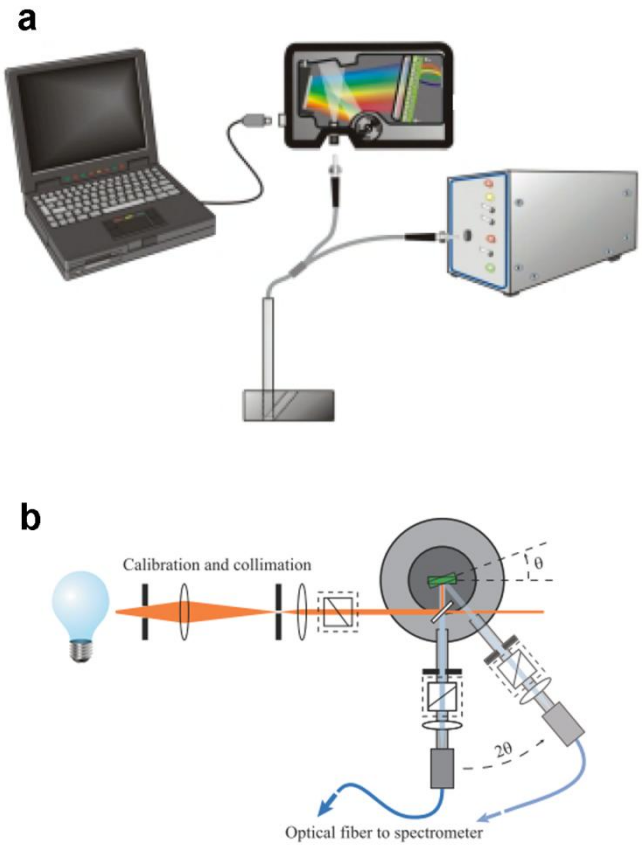

Figure 2.4. a, Schematic illustrations of spectrometer (Ocean Optics 2000) and b, angle-resolved spectrometer.

In general, a single part of the structurally colored parts of photonic materials (e.g., scales of butterflies and barbules of feathers), may even display different structural colors. In this sense, the microscopic spectral detections are necessary. In the experiment, a micro-spectrometer that can detect spectra of microscopic regions can be achieved by connecting the spectrometer with optical microscopy. The beam size and direction can be controlled by the optical microscope.

2.3.3 Micro- / Nano-structures characterization

The micro- / nano-structures of natural structural color and fabricated photonic crystals are characterized by scanning electron microscope (SEM).

In a typical SEM (Fig. 2.5), an electron beam is thermionically emitted from an electron gun fitted with a tungsten filament cathode. The electron beam, which generally has an energy ranging from 0.5 keV to 40 keV, is focused by one or two condenser lenses to a spot about 0.4 nm to 5 nm in diameter. The beam passes through pairs of scanning coils or pairs of deflector plates in the electron column, in the final lens, which deflect the beam in the *x* and *y* axes so that it scans in a raster fashion over a rectangular area of the sample surface.

When the primary electron beam interacts with the sample, the electrons lose energy by repeated random scattering and absorption within a teardrop-shaped volume of the specimen known as the interaction volume, which extends from less than 100 nm to around 5 μm into the surface. The energy exchange between the electron beam and the sample results in the reflection of high-energy electrons by elastic scattering, emission of secondary electrons by inelastic scattering and the emission of electromagnetic radiation, each of which can be detected by specialized detectors. The beam current absorbed by the specimen can also be detected and used to create images of the distribution of specimen current. Electronic amplifiers of various types are used to amplify the signals, which are displayed as variations in brightness on a cathode ray tube (CRT). The raster scanning of the CRT display is synchronized with that of the beam on the specimen in the microscope, and the resulting image is therefore a distribution map of the intensity of the signal being emitted from the scanned area of the specimen. The image is digitally captured and displayed on a computer monitor and saved to a computer's

hard disk. The magnification of a SEM can be controlled over a range of up to 6 orders of magnitude from about 10 to 500,000 times.

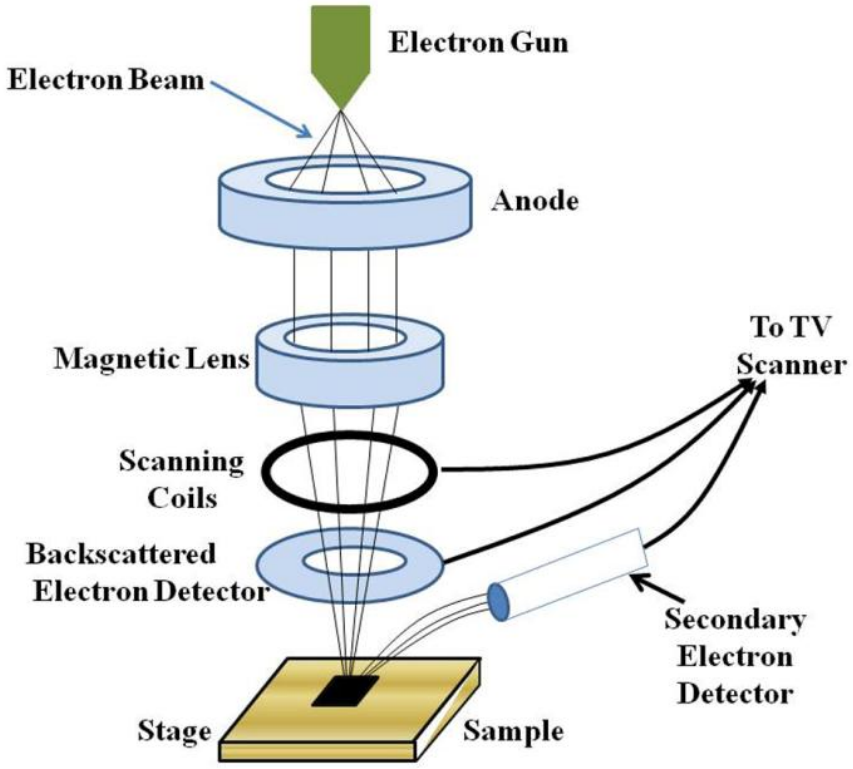

Figure 2.5. Schematic illustration of scanning electron microscope (SEM).

2.4 Theoretical analysis of the optical properties of photonic crystals

As introduced in chapter 1, structural color is produced by photonic crystals. Photonic crystals are composed of periodic dielectric or metallo-dielectric nanostructures that affect the propagation of electromagnetic waves (EM) in the same way as the periodic potential in a semiconductor crystal affects the electron motion by defining allowed and forbidden electronic energy bands. Essentially, photonic crystals contain regularly repeating internal regions of high

and low dielectric constant. Photons (behaving as waves) propagate through this structure - or not - depending on their wavelength. Wavelengths of light that are allowed to travel are known as modes, and groups of allowed modes form bands. Disallowed bands of wavelengths are called photonic band gaps. This gives rise to distinct optical phenomena such as inhibition of spontaneous emission, high-reflecting omni-directional mirrors and low-loss-waveguiding, amongst others.

Since the basic physical phenomenon is based on diffraction, the periodicity of the photonic crystal structure has to be of the same length-scale as half the wave-length of the EM waves i.e. ~350 nm (blue) to 700 nm (red) for photonic crystals operating in the visible part of the spectrum - the repeating regions of high and low dielectric constants have to be of this dimension.

The photonic band gap (PBG) is essentially the gap between the air-line and the dielectric-line in the dispersion relation of the PBG system. To design photonic crystal systems, it is essential to engineer the location and zise of the bandgap; this is done by computional modeling using any of the following methods..

1. Plane wave expansion method
2. Finite element method
3. Finite difference time domain method
4. Bloch wave method
5. Transfer matrix method

For natural photonic structures, analytical treatments are only possible for some particular cases, e.g., thin films[72]. To treat quantitatively, numerical simulations are absolutely necessary since natural photonic structures are usually of diverse and complexity. Analytical or numerical results can provide reflection, scattering,

transmission, and absorption spectra that can directly compare with experimental ones. Moreover, the mechanisms of structural coloration can be inferred from which we may unravel interesting light steering strategies and even new phenomena. With the development of computational algorithms and computer itself, various computational methods have been proposed to analyze the optical properties of photonic crystals numerically. Commonly used methods include transfer matrix method (TMM)[85-87], finite-difference time-domain (FDTD)[88,89], and plane-wave expansion (PWE)[90].

Transfer Matrix Method

In this study, TMM was used to analyze the coloration mechanism for multi-layer structures. The reflectance spectrum can be predicted by the transfer matrix method. The characteristic matrix of an assembly of *n* layers of films is calculated by multiplying the matrices of each individual film.

$$\begin{pmatrix} X \\ Y \end{pmatrix} = \left\{ \prod_{r=1}^{n} \begin{pmatrix} \cos\delta_r & \frac{i\sin\delta_r}{\eta_r} \\ i\eta_r \sin\delta_r & \cos\delta_r \end{pmatrix} \right\} \qquad (2.1)$$

where $\eta_r = N_r \cos\theta_r$, $\eta_{n+1} = N_{n+1}\cos\theta_{n+1}$, and $\delta_r = (2\prod N_r d_r / \lambda)\cos\theta_r$, Nr denotes the refractive index of the film, λ is the wavelength of incident light in vacumm, d_r is the thickness of the r^{th} film, θ_r is the external angle of incidence. The reflectance (R) of the assembly can readily be expressed as,

$$R = \frac{(\eta_0 X - Y)(\eta_0 X - Y)^*}{(\eta_0 X + Y)(\eta_0 X + Y)^*} \qquad (2.2)$$

Plane wave expansion method

The plane-wave expansion method is normally employed to calculate the band structure using an eigen formulation of the Maxwell [91], and thus solving for the eigen frequencies for each of the propagation directions and the wave vectors. Each of the eigenmodes for frequency ω and wave vector ***K*** is represented as:

$$E_{\vec{K}}^{\omega}(\vec{r},t) = \exp(-i\omega t)\sum E_{\vec{K},\vec{G}}^{\omega} \exp[i(\vec{K}-\vec{G})\bullet\vec{r}] \qquad (2.3)$$

where ω is the angular frequency, ***E*** is the electric field vector, ***G*** is the reciprocal lattice vector, and the sum extends over all reciprocal lattice vectors ***G*** . Figure 2.6 corresponds to the band structure of a 1D photonic crystal with air-core interleaved with a dielectric materials of relative permittvity 12.25, and a lattice period to air-core thickness ratio (d/a) of 0.8, is solved using 101 planewaves over the first Brillouin zone. In this study, the calculation of the band structure of fabricated colloidal crystals and silk fibroin inverse opals with the FCC structure was performed by a plane-wave expansion method.

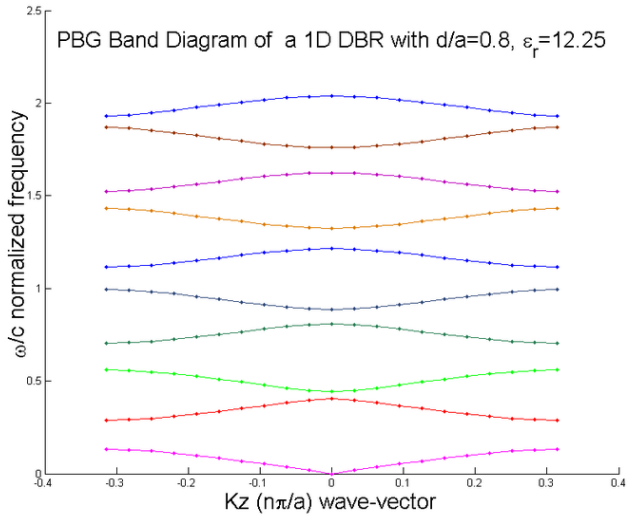

Figure 2.6. Band structure of a 1D photonic crystal, calculated using palne wave expansion technique (this figure is cited from wikipedia, http://en.wikipedia.org/wiki/Photonic_crystal).

CHAPTER 3

Structural Coloration Mechanisms and Structurally Assisted Blackness of *Papilio* Butterflies

3.1 Introduction

3.1.1 Structural color of butterfly wings

The coloration in the animal kingdom, as seen in birds' feathers and butterflies' wings, is often an additive mixture of structural colors[6,17,23,92]. The structural coloration is produced by physical interactions of light with biomaterials which have nano-structural variation in the refractive index on the order of the visible wavelength. The structural colors can be divided into two classes: iridescent and non-iridescent. The iridescent color normally is generated by reflection or scattering of light from an ordered array of scatters[5]. On the other hand, the non-iridescent color from the feathers of many birds is produced by quasi-ordered array of air vacuoles in the medullary keratin[93].

Certain species of butterflies exhibit typical blue and green structural colors, which are brighter and more deeply saturated than those typically arising from pigments. The structural coloration is known to be produced by the nano-structures in wing scales of these butterflies[94,95]. As we have mentioned in Chapter 1, these structures show some variations based on two different central design principles[21]. The first, named as class 1 or *Morpho* type, comprises of a multi-

layer structure within the discrete ridged structures on the surface of scales that cover the wings. The second, referred to class 2 or *Urania* type, comprises of continues multi-layers within the body of scales. One particular characteristic of class 2 type is the modulation of the profile of the multi-layer structure, which introduces concave structure into the scale. This specific concave structure can be found in many *Papilio* butterflies, and gives rise to some particular optical properties, such as polarization, colors mixing *etc.*[15]. *Papilio Ullysess* and *Papilio Blumei* are two species of butterflies exhibiting colorful scales with typical properties of structural colors. P. Vukusic *et al*. discussed the colors mixing and polarization effect of *Papilio Palinurus* butterfly [14,15]. However, some particular optical properties and their structural originations are not fully understood yet. For instance, the structural colors exhibited by *Papilio* butterflies are generally thought to be iridescent as they are originated from ordered structures. To the best of our knowledge, no further efforts have been made to discuss the effects of *Papilio* butterflies' concavity structure on the angular reflectance property of their structural colors. Also, the ridges on the surface of *Papilio* butterflies' wing scales are rare discussed.

Due to its wide applications in photonic crystals, cosmetics, and display technology[27,28], structural color has become the subject of extensive studies recently. We notice that some optical properties and visual ecology of butterflies are correlated with their behaviors, such as mating, aposematic communication, *etc.*[96,97]. Investigating the coloration mechanisms of these optical properties and the corresponding structures also has crucial implications for biomimicry, including color-stimulus synthesis, display technologies, various polarization applications [98,99].

In this chapter, the biophotonic nanostructures and optical properties for two species of *Papilio* butterflies, *Papilio Ullysess* and *Papilio Blumei,* will be investigated. We will explore their coloration mechanisms, especially the correlation between their nanostructures and optical properties (e.g. polarization, colors mixing). The role of the structures of the ridges and the concavities, as well as the profile of the concavities on the colors mixing and polarization effect will be examined. The reflectance spectra under normal and 45^{o} illumination of these two species of butterflies will be discussed as well. A deep and comprehensive understanding on this matter will help us not only to study some animal's behaviors, but also to mimic the structural colors in nature.

3.1.2 Black wing scales of butterfly

Besides the wing scales with vivid colors, ultra-black wing scales exists across the fore and dorsal wings of *Papilio* butterfly. Ultra-black surfaces with low reflectance are ubiquitous in animate systems. They form essential components of the visual appearance of most living species and can explicitly influence other biological functions such as thermoregulation.

Ultra-black surfaces that absorb 99.6% of incident light have recently been produced by chemical etching of electro-deposited nickel–phosphorus[100,101]. It was found that optimum phosphorus content and etching regime were required to produce the appropriate surface morphology to minimize this reflectivity and thus enhance the absorption. Such ultra-blackness is technologically crucial in areas associated with the operation of optical instruments, it is also important in natural systems. For instance, controlled absorption of incident solar radiation is the principal method of temperature regulation in most insects. The quality of

blackness, or the quality of light absorption on an insect's surface, will influence its wing and body temperature. The visual appearance of many brightly colored creatures is influenced by both the quality of the dark frame that surrounds their color regions as well as the absorbing medium beneath them. A strongly back-scattering substrate is required to create a saturated reflection of the structurally colored region in these creatures[102]. Therefore, there is a need for effective broad-band absorption to augment bright color.

The blackness associated with most of the opaque surfaces of low reflectivity has until now been attributed to strongly absorbing pigmentation alone. Here, we demonstrate that in addition to the requirement of absorbing pigmentation, complex nano-structures contribute to the low reflectance of certain natural surfaces[103]. In this chapter, we quantify the optical absorption associated with black wing regions on the butterfly *Papilio Blumei* and find that the nano-structure of the wing scales of these regions contributes significantly to their black appearance.

3.2 Results and discussion

3.2.1 Observation and spectral analysis of the structural colors in *Papilio* Butterflies

To a human observer, *P.Ulysess* and *P.Blumei* are distinct by their respective bright blue and green coloration (Fig. 3.1). To quantify the structural coloration of the butterflies' wings, the UV-Visible (λ =200-850nm) reflectance spectra for the two species of butterflies were measured and given in Fig. 3.2. In Fig. 3.2a, the reflectance spectra of *P.Ulysess* for both normal (black curve) and 45^{o} incident light (red curve) are shown. Two separated peaks can be identified from the

spectra of the two incident angles. Under normal incident light, a main peak locates at ~ 550nm and a small peak at ~380nm. However, the positions of the spectral peaks shift under 45^{o} incident light: the main peak shifts to ~350nm and the small peak to ~550nm. These apparent shifts of the spectral peaks indicate that the coloration in the blue scales of *P.Ulysees* is iridescent. And the two distinct spectral peaks of *P.Ulysess* suggest the possibility of colors mixing mechanism, which leads to the blue coloration in *P.Ulysess* wings. Unlike *P.Ulysess*, the reflectance spectra of *P.Blumei* for normal incident (black curve) and 45^{o} incident (red curve) light almost overlap with a broad peak ranges from 480nm to 620nm (Fig. 3.2b).

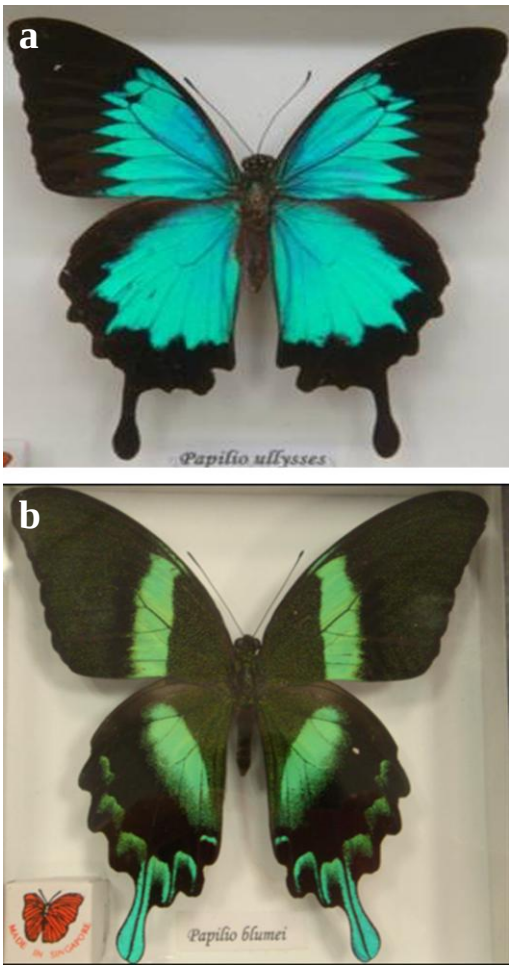

Figure 3.1. Photograph of (a) *P. Ullysess* and (b) *P. Blumei* butterflies showing their blue and green colors.

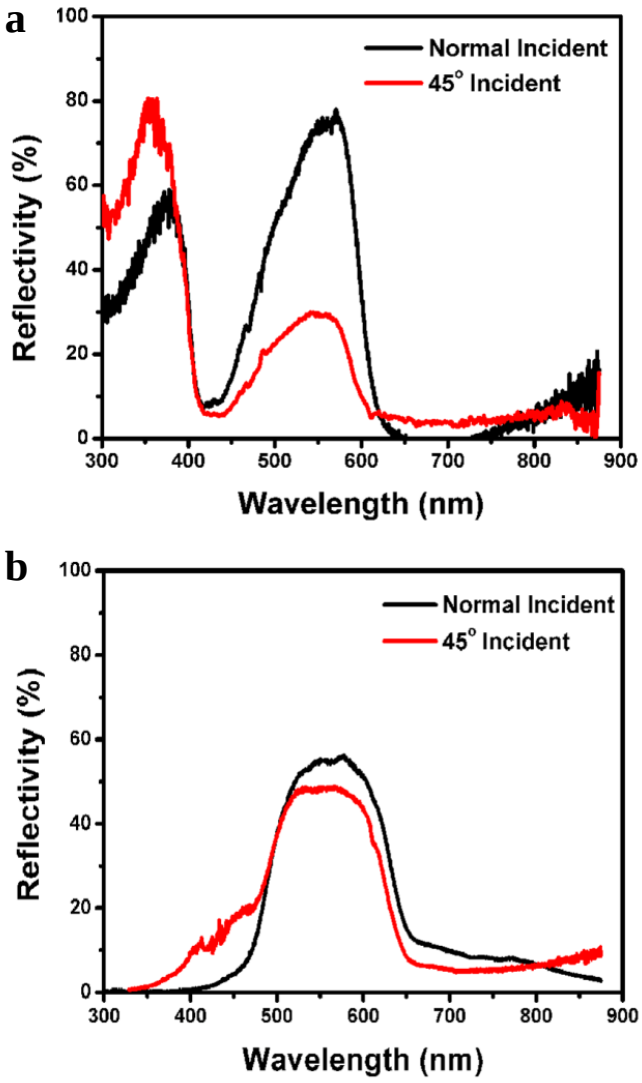

Figure 3.2. Measured reflectance spectra for (a) *P. Ullysses* and (b) *P. Blumei*, black lines indicate spectra for normal incident light while red lines are spectra for 45^{o} incident light

Here two questions need to be addressed. Firstly, which corresponding parts of the iridescent scales of *P.Ullysess* are responsible for the two distinct spectral peaks? Secondly, why does the spectrum remain the same at different incident angles for *P.Blumei*? In the following session, we will examine the microstructures and the related optical properties of the colorful scales for these two species of butterflies to answer these questions.

3.2.2 Structural characterization and optical properties of the structural colored wing scales of *Papilio* Butterflies

The microstructures of colorful wings of *P.Ulysses* and *P.Blumei* were characterized by field emission scanning electron microscope (FE-SEM) (Fig. 3.3). The surface of their wings is composed of millions of scales. The scales of *P.Ulysess* are of a size around $150 \times 90\ \mu m^2$, and consist of a fairly regular array of concavities (Fig. 3.3a). The profile of the concavities is almost flat (Fig. 3.4a). The ridges run through the full length of the scales with a periodicity of 4-5 μm. The details of the period structure of a ridge are displayed in Fig. 3.4b, and inset of Fig. 3.4b illustrate the structure schematically. The main ribs are of a thickness (d_1) of ~70nm with the inter-distance (D_1) of ~70nm. Two adjacent ribs are bound together by a row of smaller sub-ribs with a thickness of ~60nm (d_2) and an inter-distance of ~100nm (D_2). This configuration constructs a 2D array of 70nm × 100nm rectangular air squares surrounded by organic cuticle layers (the main and sub-ribs) with a periodicity of ~140nm (D_1+d_1) along its length direction and ~160nm (D_2+d_2) along the main ribs. This long-range ordered structure with a very small periodicity can be considered to be a 2D photonic crystal slab tilt about 30^o with respect to the surface of the scales[30]. Therefore, the ridges exhibit typical structures of class 1 or *Morpho* type. The scales of *P.Blumei* have a size of $\sim 180 \times 100\ \mu m^2$, and the surface also consists of a fairly regular array of concavities (Fig. 3.3b). Different from *P.Ulysess*, the concavities of *P.Blumei* are cap shaped, with 4-6μm in diameter, and their profile is much deeper than *P.Ulysess* (Fig. 3.4d). The inclined sides of each concavity tilt ~45^o with respect to the horizontal surface, and the opposites of each concavity are perpendicular to each other. The

ridges run through the full length of each scale with a periodicity of 7-8μm. Compared with that of *P.Ulysess*, the ridges are smaller and have no significant multi-layered structures (Fig. 3.4e).

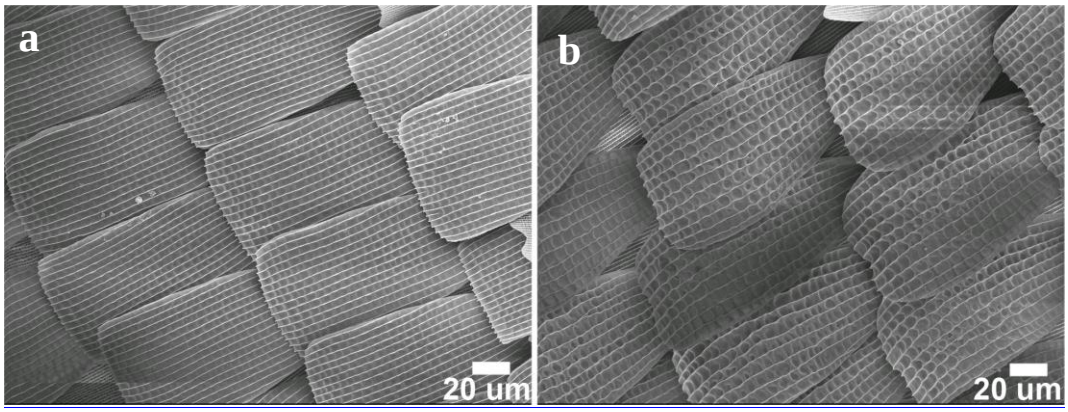

Figure 3.3. SEM images of the scales on the surface of (a) *P.Ullysess*, and (b) *P.Blumei* b.

To obtain the detailed structure of the scales, the transverse cross section structure was examined for the two species of butterflies. The transverse cross section for the scales of *P.Ulysess* consists of 21 alternative cuticle and air layers (Fig. 3.4c), which share almost the same thickness (~95nm). The section structure for the colorful scales of *P.Blumei* is similar with *P.Ulysess*, except the concavities' profile and the thickness of each layer (~110nm) (Fig. 3.4f). Therefore, the concavities for these two species of butterflies possess structural properties of class 2 type.

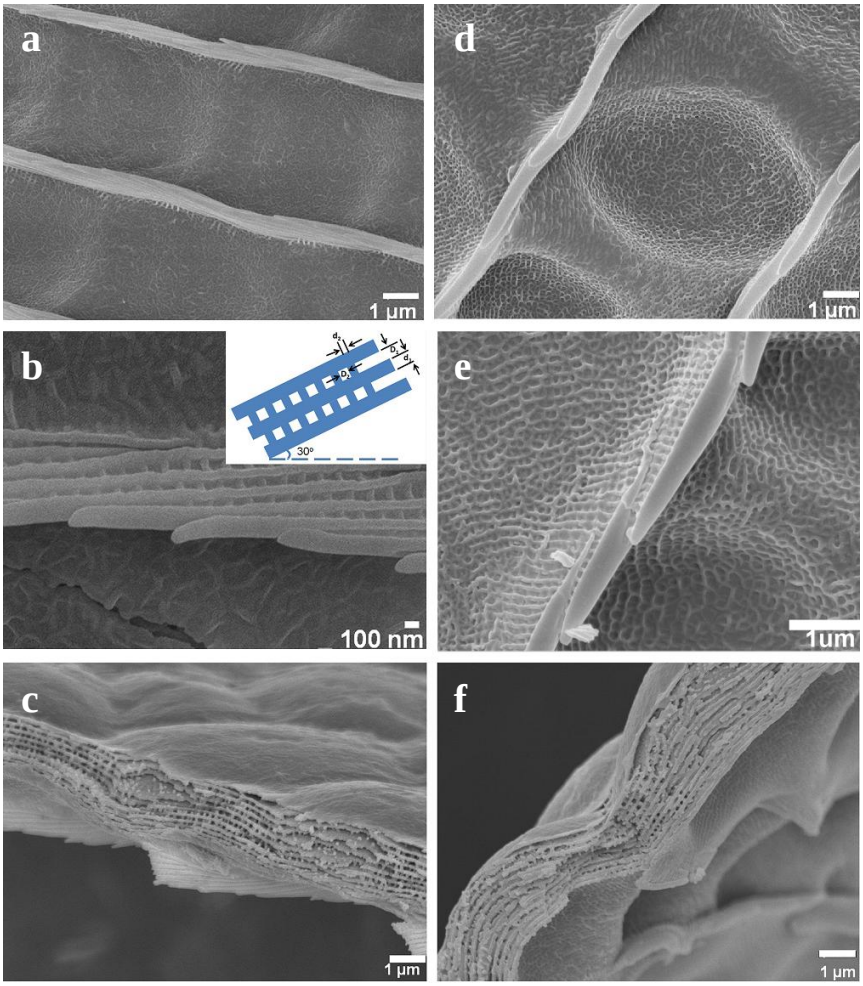

Figure 3.4. SEM images of the concavities (a), ridges (b) and transverse cross section (c) structures for *Papilio Ullysess*, SEM images of the concavities (d), ridges (e) and transverse cross section f structures for *Papilio Blumei.*

The optical microscopy images of the two species of butterflies under normal incident light and linear polarized light were carried out in order to acquire their optical properties (Fig. 3.5). When illuminated and observed at normal incident light, the concavities in *P.Ulysess* appear to be green and the flat portions between and in the concavities of *P.Blumei* reflect yellow. Furthermore, in *P.Blumei*, the inclined sides around concavities reflect blue light. However, upon crossing an input linear polarizer with an exit analyzer, the green reflected light in *P.Ulysess* and the yellow color in *P.Blumei* almost disappear while the deep purple (near-UV) color reflected by ridges in *P.Ulysess* and the blue color in *P.Blumei* reflect

back. This implies that the purple and the blue reflected light are not altered by the polarizers.

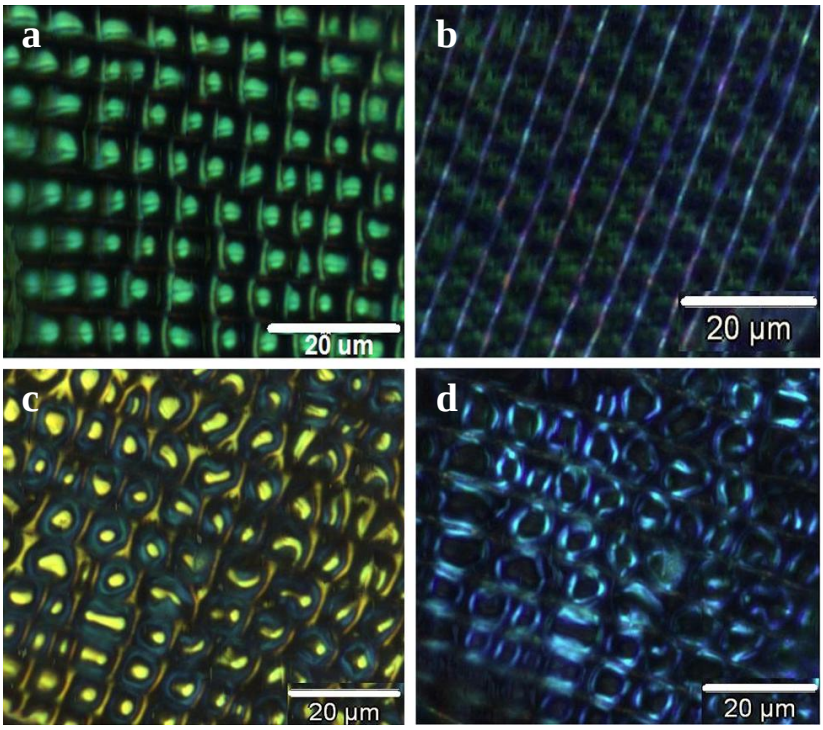

Figure 3.5. Optical microscopy images of the butterflies. (a) Bright field image and (b) taken under crossed polarizers for *P.Ullysess.* (c) Bright field image and (d) taken under crossed polarizers light for *P.Blumei*. Scale bar: 20µm

As mentioned, there are two peaks in the reflectance spectra of P.Ulysess. Therefore, the blue coloration perceived by human eyes is a mixture of these two peaks. Comparing with the optical microscopy image (Fig. 3.5a and Fig. 3.5b), under normal incident light, the main peak (550nm) is produced by the green colored concavities and the small peak (380nm) is produced by the deep purple colored ridges. In addition, the reflectance spectra for normal and 45^{o} incident light differ greatly, suggesting the coloration of the colorful scales in *P.Ulysess* is angle-dependent. In contrast, the reflectance spectra of *P.Blumei* are almost the same under normal and 45^{o} illumination light. The green color of P.Blumei is produced by mixing the yellow and blue colors reflected from the concavities. In

this process, the blue color undergoes a polarization conversion, meaning that a bi-reflection occurs from the inclined sides of the concavities.

3.2.3 Structural coloration mechanisms of the *Papilio* Butterflies

To obtain an in-depth understanding on the colors mixing strategies of these two species of butterflies, the coloration mechanisms were explored theoretically. Based on the plane-wave expansion method[104,105] as described in Chapter 2, the reflectance spectrum by a multi-layer structure can be predicted by the transfer matrix method.

To find the structural origin of the two characteristic peaks in the measured reflectance spectra for *P.Ulysess*, we first analyze the structure given in Fig. 3.3. The transverse cross section of the concavities reveals a multi-layer structure composed of 21 alternative cuticle and air layers. These cuticle and air layers share almost the same thickness (~95 nm). The refractive index of the cuticle layer is 1.56 [22]. For the air layer, it consists of disordered cuticle particles with a density (C) of ~20% (Fig. 3.6a). Thus, the effective refractive index of the air layer can be acquired based on the density of the cuticle particles: $n_{eff} = 1.56 \times C + (1-C) \approx 1.11$.

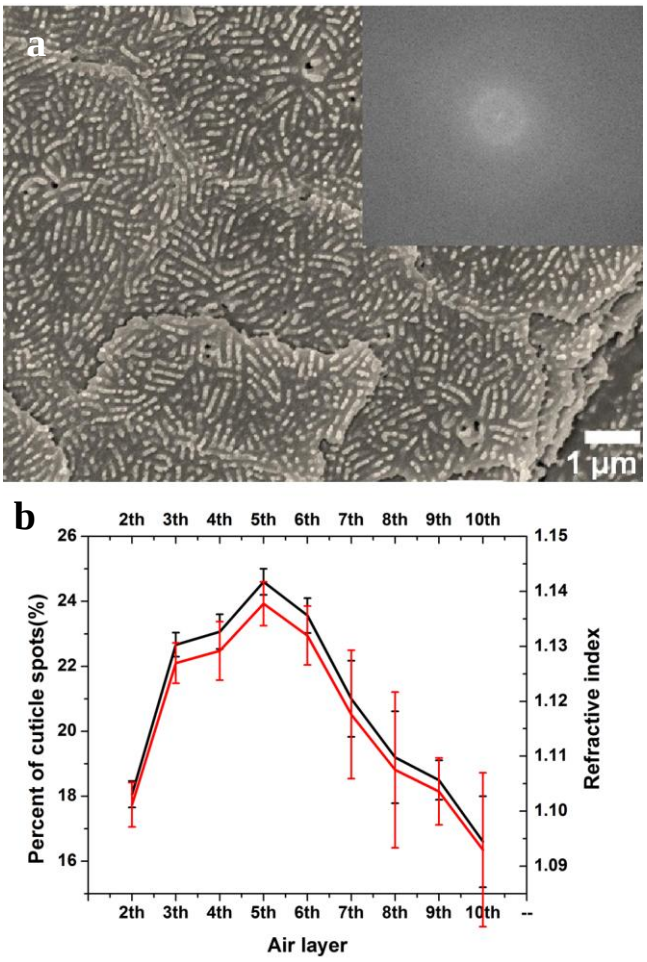

Figure 3.6. a: The air layer structures for the multi-layered scales, some cuticle particles distribute on the surface of the air layer. Inset is 2D Fast Fourier Transform of the image, which proves that the cuticle particles are randomly distributed. b: The densities of the cuticle particles on different layers are different, as well as the refractive indexes of the air layers. The value of density and refractive index increases from the first to fifth layer, and then decreases from the fifth to tenth layer.

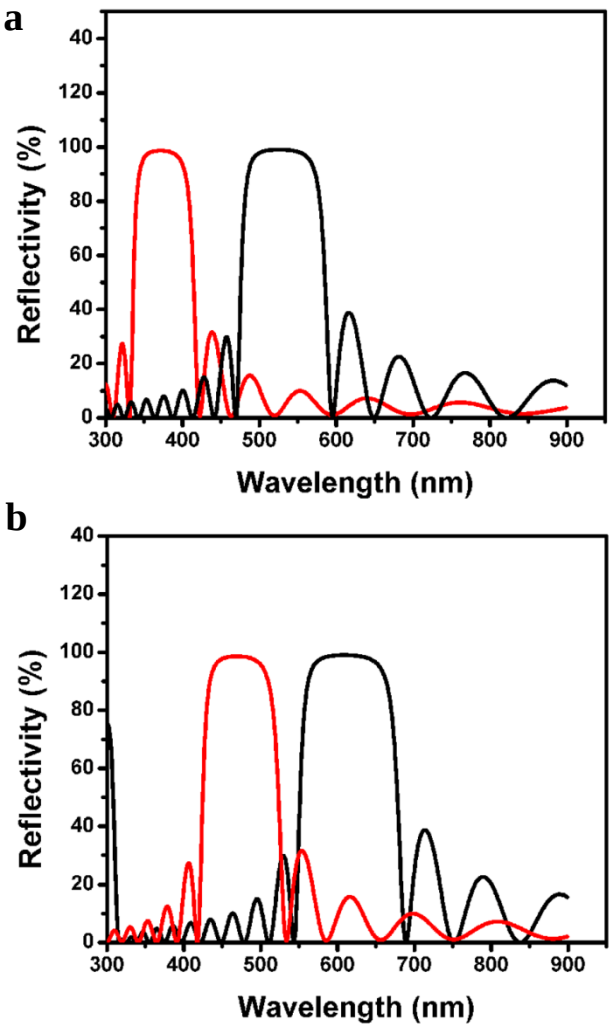

Figure 3.7. Theory calculated reflective spectra for (a) *P.Ulysess* and (b) *P.Blumei* according to the multi-layer structures of their concavities, black lines are spectra for normal incident light and red lines are for 45^{o} incident light. For *P.Ulysess*, the spectral peak reflected by concavities is 550nm under normal incident light and 380nm under 45^{o} incident light. For *P.Blumei*, the spectral peak reflected by the flat portions of concavities is 600nm under normal incident and 450nm under 45^{o} incident light.

The reflection peak produced by the concavities can be calculated based on Eq. (1): ~550nm for normal incident light, and ~350nm for 45^{o} incident light (Fig. 3.7a). However, the situation for the ridges is totally different. As described in

section 3.2, the ridges can be considered as 2D photonic crystal slabs, and tilt ~30^{o} with the horizontal surface. The normal incident light interacts with the main ribs at 60^{o} (Fig. 3.8a), and produces a reflectance peak at ~380nm, while the 45^{o} incident light interacts with the main ribs at 15^{o} (Fig. 3.8b), and gives rise to a reflection peak at ~550nm. Therefore, the two spectra peaks originating from the concavities and the ridges could be observed for both normal and 45^{o} incident light. Under normal incident light, the main peak is at ~550nm (produced by concavities) and small peak at ~380nm (produced by ridges). Under 45^{o} incident light, the main peak shifts to ~350nm (concavities) and the small peak to ~550nm (ridges). These theoretical results are in excellent agreement with the experimental measurements (Fig. 3.2a). The spectral peaks of *P.Ullysess* for two illumination cases are summarized in Table 1.

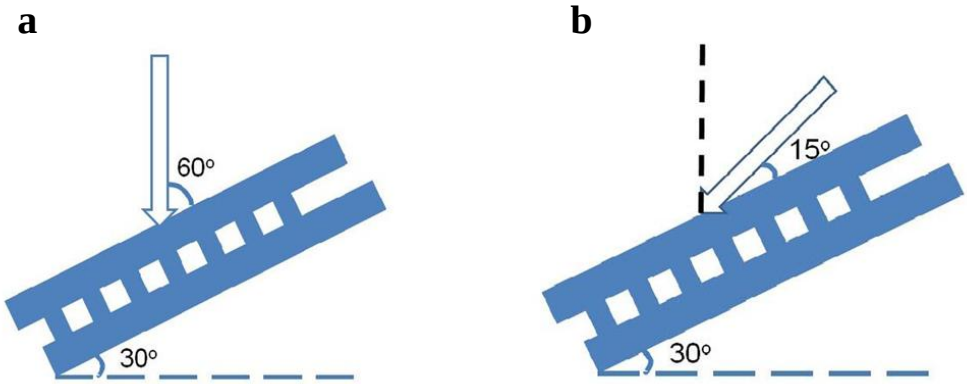

Figure 3.8. Illustration of the coloration mechanism of the ridge on the scale surface of *P.Ullysess*. (a) The normal incident light interacts with the main ribs at an angle ~60^{o}, and (b) ~15^{o} for the 45^{o} incident light.

Measurement &Theory	Main peak	Small peak
Normal incident	550nm (by concavity)	380nm (by ridge)
45^{o} incidence	350nm (by concavity)	550nm (by ridge)

Table 3.1. Illustration for the two reflection peaks of *P.Ullysess.*

The cap shaped concavities of *P.Blumei* are also composed of 21 alternative cuticle and air layers with a thickness of ~110nm. For normal incident light, the calculation predicts that the reflection peak resulted from the flat portions locates at 600nm (Fig. 3.7b), in agreement with the yellow color observed under optical microscopy. The inclined sides of each concavity tilt ~45^{o} with respect to the horizontal surface, and the opposites of each concavity are perpendicular to each other. As illustrated in Fig. 3.9a: the normal incident light, reflected from one 45^{o} side, travels across the concavity to the opposite orthogonal side, and then reflects backward in parallel to the original incident direction. The reflection peak originated from the inclined sides of the concavity is 480nm, in accordance with the blue color observed under optical microscope. Through this bi-reflection process, the blue reflected light undergoes a polarization conversion. As a result, it survives upon the crossed polarizers (Fig. 3.5d). Under 45^{o} light, the reflection peak arising from the flat portions is 480nm (blue color); while the inclined sides is incident normally by the light, and gives rise to a reflection peak locating at 600nm (yellow color) (Fig. 3.9b). Therefore, for normal and 45^{o} incident light, the cap shaped concavities both produce yellow and blue colors. These two colors mix up the green coloration caught by human eyes. This gives answer to the question why the reflectance spectra are almost overlapped for these two cases illumination. In Table 2, we summarize the reflectance peaks for *P.Blumei* in two cases illumination.

We notice that many studies show that the eyes of the butterflies have a duplicated gene, allowing them to see ultraviolet colors and distinguish the spectral properties and spatial distribution of the visual colors[106]. And also, they are sensitive to the polarized light. Therefore, the knowledge on the structural origina-

tion of the two reflection peaks and polarization property of butterfly wings would have broad biological implications[107,108]. Furthermore, with the understanding of the correlation between the optical properties and the corresponding structures, researchers could be able to find a way to mimic natural structural colors with designated properties. Evidently, the ability to mimic the structural color with its spectacular function will broaden the biomimicry field in the design of structural color materials targeted for ultra and smart performance.

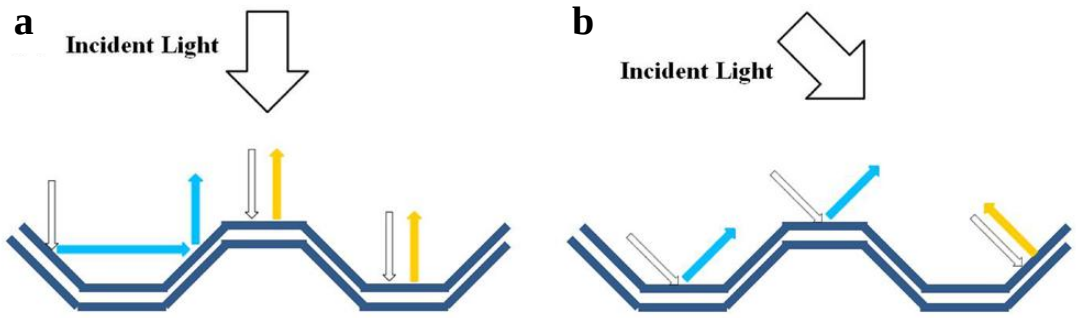

Figure 3.9. Illustration of the coloration mechanism of *P.Blumei*'s concavities under normal incident light (a) and 45^{o} incident light (b).

Measurement &Theory	Flat portions	Inclined sides
Normal incident	600nm (yellow)	480nm (blue)
45^{o} incidence	480nm (blue)	600nm (yellow)

Table 3.2. Illustration for the colors mixing mechanism of *P. Blumei*

3.2.4 Structurally assisted blackness in *Papilio Ulysess* butterfly wing Scales

A male *Papilio Blumei* butterfly was chosen for this study because it exhibits two regions of different blackness across parts of its wings as seen in Fig. 3.10; one region is deep matt black in appearance on fore wings whereas the other is

optically a much more lustrous black on dorsal wings. These black regions completely frame the intense green color of the inner regions of both fore and dorsal wings. Both the black parts of the fore and dorsal are hydrophobic surfaces: the contact angle of the blackness on fore wings is 127^{o} and 147^{o} for blackness on dorsal wings.

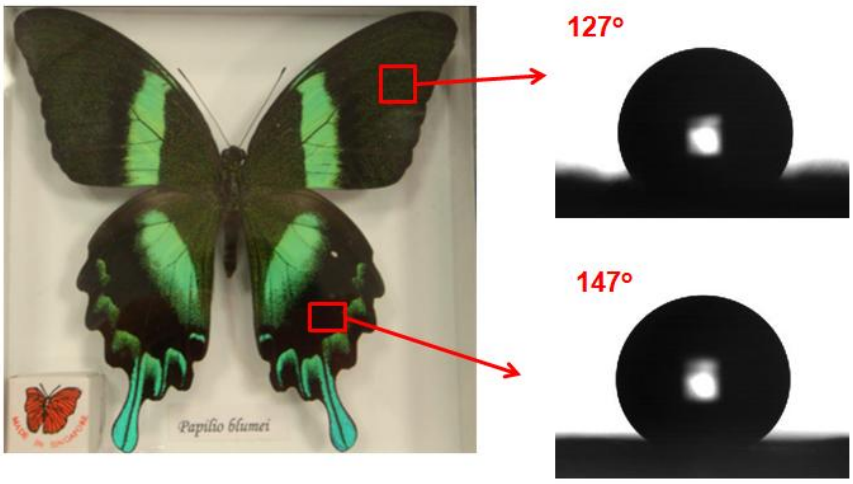

Figure 3.10. The black wing scales of *Papilio Bluei*, and their contact angles

Optical absorption spectra of the black scales on both fore and dorsal wings were measured using spectrometer (Ocean Optics, USB 2000). To examine the extent that microstructure played in the optical absorption associated with black wings, the optical experiments were repeated while the scale on its needle was immersed in butonal. This process matches the refractive index of the scale material to that of its surroundings and effectively eliminates the optical functions of the scales' nanostructure. Light incident on the wings will therefore only be subject to the absorption pigments within it, and not to any interference, scattering or diffractive effects associated with the scale nano-structure.

The data in Fig. 3.11 shows the difference in absorption between black region before and after the structure has been index matched by butonal. For black wing

from the matt black region of wing, the immersion in butonal causes a 50% decrease in the optical absorption of the scale; for black wings from the lustrous region, there is a 20% decrease in this absorption.

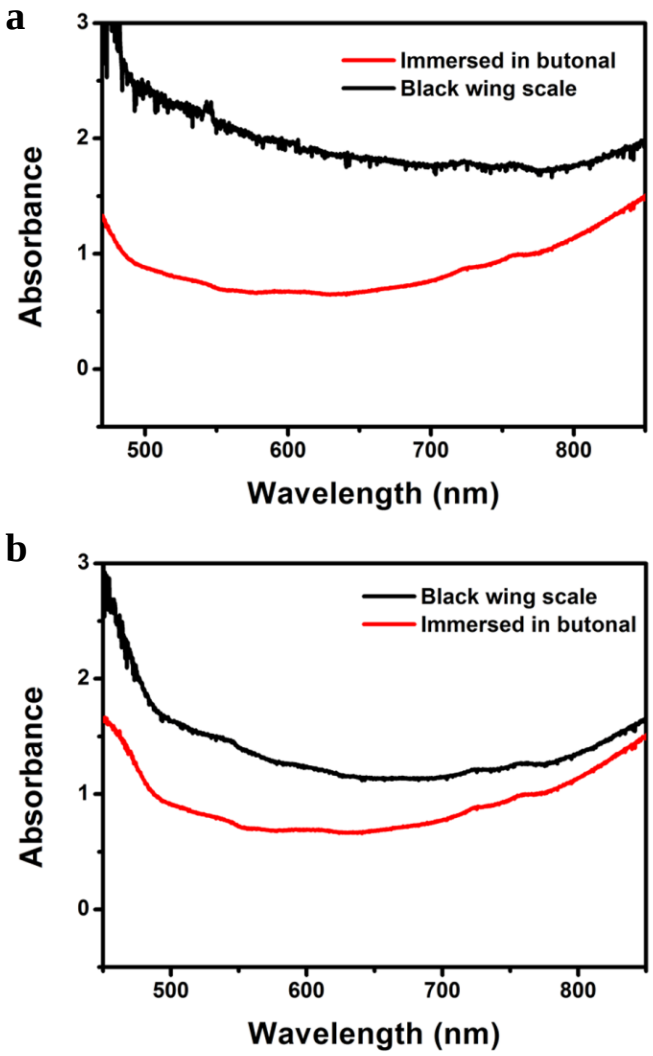

Figure 3.11. The wavelength-dependent absorption (at normal incidence), in air and immersed in butonal of black scales from the matt black region (a) and the lustrous black (b).

The evidence from the index-matching experiments clearly shows that effective removal of the scale structure (by immersion in index-matching fluid) reduces the optical absorption of the scale. Without such a nanostructure, even with the same quantity of absorbing pigment, each scale would be a less efficient absorber of

incident radiation; backscatter from the scales and wing substrate beneath these scales would create the appearance of a wing surface of inferior blackness.

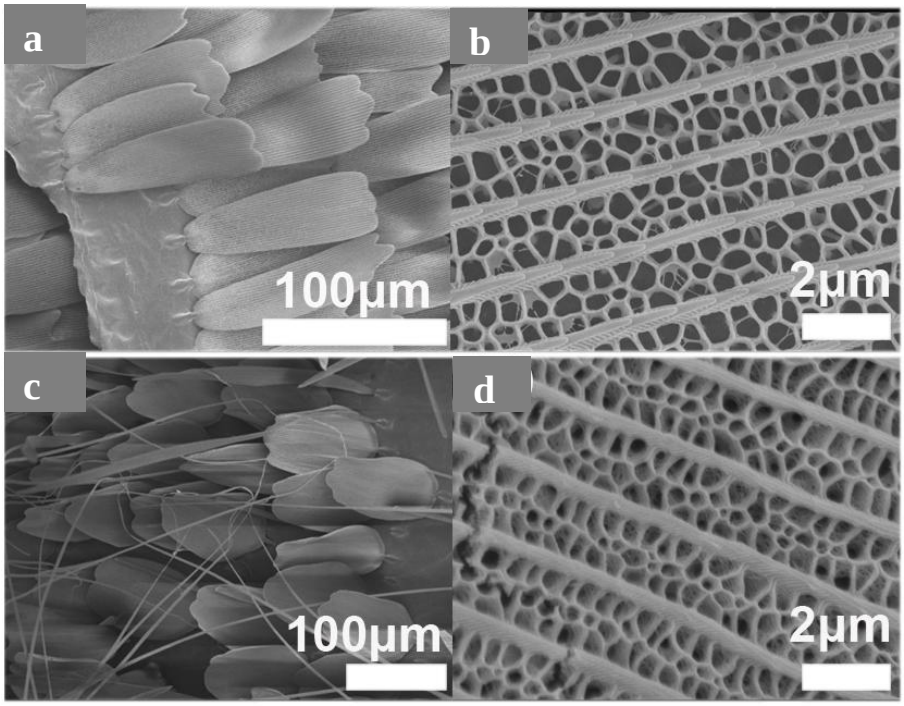

Figure 3.12. The nanostructure of the black sacles from two regions of wing of *Papilio Blumei*. (a), (b) SEM images of the surface of the wing scales from the lustrous black regions with low and high magnifications, respectively. (c), (d) SEM images of the surface of the wing scales from the matt black regions with low and high magnifications, respectively.

The structure of the black scales of *P. Blumei* (Fig. 3.12) is typical of deep matt and lustrous black scales found on many other Lepidoptera. Periodic ridges, of pitch 2–3 μm run the length of these scales. Between their ridging, scales from both regions exhibit a periodic lattice work of struts and walls that extend from the surface toward the scale substrate beneath. The change in optical absorption, on immersion in index-matching fluid, is different for both scale types. This is solely a consequence of their structural differences, which are particularly evident in images of the scale structures (Fig. 3.12b & d). The scales from the matt black region (Fig. 3.12c & d) clearly comprise a more intricate and densely distributed

lattice of cuticle than the scales from the lustrous black region (Fig. 3.12a & b). Light that is incident on this structure, therefore, is more efficiently scattered toward the diffusely distributed pigmentation.

3.3 Materials and experimental

The two species of *Papilio* butterflies, *P.Ullysess* and *P.Blumei* were bought from insets and butterfly kingdom of Singapore.

The reflectance and absorption spectra for butterfly wings were measured with an Ocean Optics USB2000 spectrometer attached to a PX-2 pulsed xenon light source (200-850 nm). All measurements were taken with R200-7 UV-VIS optic fiber reflection probe. The R200-7 consists of a tight bundle of 7 optical fibers in a stainless ferrule --- 1 illumination fiber surrounded by 6 read fibers. By placing the probe into a holder with vertical and 45^{o} inclined holes, which was above the sample with a certain distance, the reflected lights in different directions for normal and 45^{o} illumination were recorded and analyzed by OOIBase32 Spectrometer Operating Software.

Bright field and polarized optical images of the colorful scales were taken by a conventional optical microscope (Olympus BX61). The digital images were captured and analyzed by the acquired image processing software (analysis 5).

The surface morphologies, transverse cross section structures and the inter-layer structures of the colorful scales on butterfly wings were characterized by a field emission scanning electron microscope (FE-SEM; JEOL JSM-6700F), previous an Pt sputtering treatment of 5-10nm.

Additionally, a theoretical analysis for the two butterflies using transfer matrix method was carried out to better understand their coloration mechanisms.

3.4 Summary

Our experiment and calculation analysis reveal that the two species of butterflies wings exhibit bi-structural-color reflection. The blue wing scales of *P.Ulysess* reflect green and UV light, which is produced by concavities and ridges respectively. The green wing scales o *P.Blumei* is a mixture of yellow and blue colors reflected by the flat portions and inclined sides of concavities. By varying the nanostructures and the profile of their concavities, the two species of butterflies exhibit totally different optical properties. Under optical microscope, the flat concavities in *P.Ullysess*' wings create single color with no polarization effect. The concavities in *P.Blumei* generate a bi-reflection. Through a bi-reflection process, the blue color reflected from the inclined sides of *P.Blumei's* concavities undergoes a polarization conversion. When illuminated with UV-Vis light, *P.Ullysess* gives rise to two reflection peaks. One originates from the concavities, and the other from the ridges. These two peaks shift their positions under different illumination conditions (normal and 45^{o} incident light). On the other hand, *P.Blumei* reflects similar reflectance spectra under these two cases illumination due to the special profile of the concavities.

The evidence from light absorption experiment of the black wing scales of *Papilio Blumei* shows that nanostructure as found in many Lepidoptera assist in creating strong optical absorption and significantly enhances the appearance of black on their wings.

CHAPTER 4

Mimicking of Bi-Structural-Color Reflection and Bring Structural Color to Fabrics

4.1 Introduction

4.1.1 Bi-structural-color reflection in biological world

Structural colors caused by the interaction of light with certain materials of the nanoscale periodic structure, so-called photonics, have attracted considerable attention in a variety of research areas[5]. The potential applications range from decorations to display technologies[28,98]. Structural color has many characteristics that differ from those of chemical pigments or dyes. The unique colors originating from the physical structures are usually iridescent and metallic, and cannot be obtained by chemical dyes or pigments.

In the biological world, the colorful feathers of many birds (i.e. peacock), the wings of various butterflies and the elytra of many beetles are good examples of structural coloration[13,23,92,94]. Apart from the aforementioned properties, natural structural colors produced by these animals also give rise to additional optical properties. For instance, the brown barbules of peacock feathers adopt mixed structural coloration[13]; the green wing scales of *Papilio Blumei* produce polariza-

tion effect and bi-structural-color reflection[14]. In particular, bi-structural-color reflection is responsible for various crucial functions in the animal kingdom. The widespread evidence indicates that animal photoreceptors can distinguish different parts of the spectrum, even also sensitive to ultraviolet (UV) light[107]. It follows that the bi-structural-color reflection of certain butterflies cover both the visible and UV ranges, which may serve as communication and mating signals[106,107]. Evidently, the construction of an effective and simple way to produce multiple-structural-color reflection covering UV, visible and infrared (IR) ranges simultaneously may point to a new direction in multi-functional photonic materials engineering. Notice that although there have been numerous attempts in the mimicking of natural structural colors[30-35,37,45], no much attention has been focused on the bi-structural-color reflection.

Bi-structural-color reflection can be created by different manners in the biological world[14-15,110]. As we described in Chapter 3, under normal incident light, the blue scales *P. Ullysess* generate a bi-reflection peaks. The concavities on the wing scales show a visible reflection peak at wavelength of λ=550 nm, which gives rise to the green coloration; the ridges on the wing scales show a UV reflection peak at wavelength of λ=380 nm. The green wings of *P.Blumei* generate an abnormal bicolor reflection under optical microscope. The bright green colored areas on *P. Blumei* wing result from a juxtaposition of blue and yellow light reflected from different microscopic regions of concavities on the wing scales. The aforementioned bi-structural-color reflection produced by the two *Papilio* butterflies are of different structural origins: in *P.Ullysess* it is produced by two different types of ordered structures of the wing scales, while in *P.Blumei* it is produced by the

different illumination angles from different parts of the wing scales, which share the same ordered nano-structure.

M. Kolle *et al.*[35] employed the combined techniques of layer deposition techniques, i.e. colloidal self-assembly, sputtering and atomic layer deposition, to fabricate a concave and multi-layer structure in order to mimic the color mixing and polarization effect of the green wing scales of *P. Blumei*. The approach is advantageous in that they can fabricate a periodic dielectric structure on the surface, which can control the reflection angle at the different locations of the surface. However, in spite of the advantage of sculpting sophisticated nanostructures in a well controlled manner, a cost-effective manufacturing scheme to generate bi-structural-color reflection over a large area is hard to achieve owing to the complicity of fabrication and precision of control.

Here, we present a new approach to design and construct biomaterials of bi-structural-color reflection by taking advantage of the particular photonic band structure of inverse opals. This will not only simplify the processing procedures and overcome the limitations of previous approaches, but also be capable of tuning the wavelengths of bi-structural-color reflection peaks easily. The material to be adopted in this work is silk fibroin. Silk fibroin has recently emerged as a highly promising biomaterial in various applications (i.e. biomedical industry), owing to its excellent mechanical and optical properties, biocompatibility, biodegradability and implant ability[50,58,111-113]. In this regard, the rapid production of silk-fibroin inverse opals with bi-structural-color reflection in both UV and visible (UV/visible), visible and IR (visible/IR), and UV and IR (UV/IR) ranges will be demonstrated. We can implement the control of the wavelengths of bi-structural-color reflection peaks by adjusting the pore size of inverse opals.

4.1.2 Structural color in eco-dyeing engineering

With reference to the textile industry, coloring or dyeing of fabrics, especially silk fabrics, is challenging. In addition, color fading due to leaching or oxidation / bleaching is a typical problem in the industry. Fabricating structural color turns out to be another option in dyeing engineering. Compared with chemical color or pigments, structural color is brighter, more deeply saturated, free from photobleaching, and longer lasting[23]. There are also significant challenges for placing structural colors on fabric. Here, silk fabrics with structural color were fabricated to demonstrate the potential applications of silk-fibroin photonic structures in eco-dyeing engineering.

4.2 Results and discussion

4.2.1 Calculation of photonic band structure of colloidal crystal template and silk fibroin inverse opal

By analogy to electron waves in a crystal, light waves in a three dimensionally periodic structure should be described by band theory, which is known as photonic band structure. If the depth of refractive index modulation of photonic crystal is sufficient, then a photonic band gap (PBG) could open up[114]. The optical properties of photonic crystals, such as the number, position and width of reflection peaks, can be predicted from their photonic band structure. Our calculation of band structure of the colloidal crystal and silk fibroin inverse opal with a FCC structure was performed by the plane-wave expansion method for vector waves as described in Chapter 2[86,115]. Fig. 4.1 shows the band structure for the colloidal

crystal along high symmetry directions in the FCC *Brillouin* zone, the refractive index of colloid particles are taken as 1.59. A partial photonic band-gap (a/λ=0.6) exists along *Γ* to *L* direction.

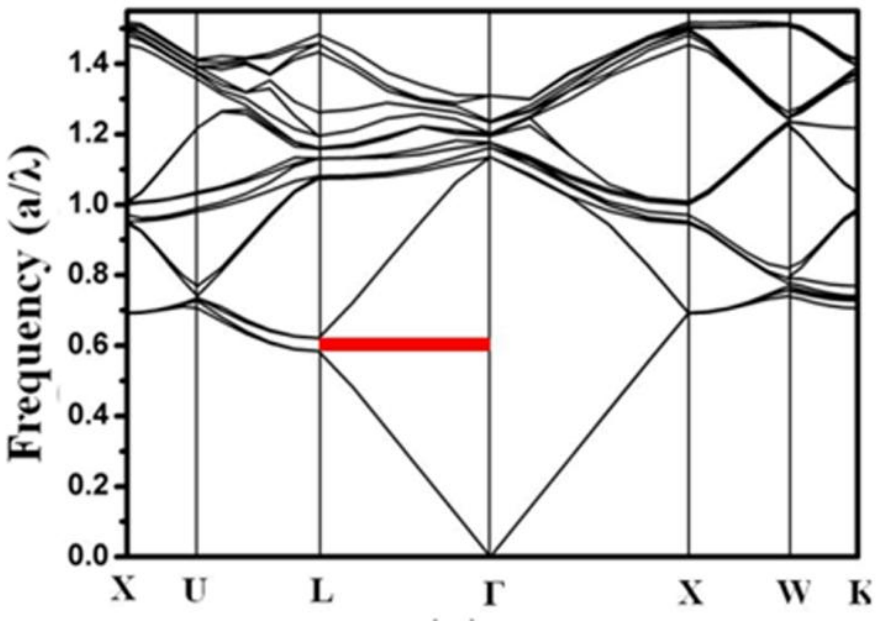

Figure 4.1: Photonic band structure of colloidal crystal

To show that a silk-fibroin inverse opal can produce bi-structural-color reflection, its photonic band structure is calculated as shown in Fig. 4.2a. In the calculations, the silk-fibroin inverse opal is assumed to consist of air spheres arranged in the face-centered cubic (FCC) lattice with silk fibroin filled in the remaining regions. The refractive index *n* of silk fibroin is 1.54, taken from Ref. 116. Obviously, there is no complete (for all directions) photonic bandgap due to the fact that the refractive-index contrast between silk fibroin and air is not big enough. However, along the *Γ*-*L* direction there exist two partial photonic bandgaps at different frequencies. For light incident along the *Γ*-*L* direction strong reflections are expected for frequency within the two partial photonic bandgaps, leading to bi-structural-color reflection at two different frequency or wavelength ranges. Note that the mid-gap frequencies of both partial photonic band gaps

increase along the direction from *L* to *U*, suggesting that the resulting bi-structural-color reflection is iridescent, in other words, the two reflection peaks will undergo a blue shift in wavelength for light incidence varying away from the *Γ*-*L* direction.

Obviously, we can implement the following approaches to adjust the bi-structural-color reflection offered by inverse opals. i) For an inverse opal, the positions of the two reflection peaks (λ_1 and λ_2) and their separation between them (λ) can be adjusted by changing the lattice constant *a* since the mid-gap frequencies are inversely proportional to *a*. ii) Once the lattice constant *a* is given, λ_1, λ_2 and λ can be adjusted by changing the refractive indices of the constituent materials. iii) If *a* and constituent materials are given, λ_1, λ_2 and λ can be changed by varying the illumination angle, similar to the case as indicated for *P. Blumei*.

For a silk-fibroin inverse opal, the mid-gap wavelength of the first partial photonic bandgap is at $\lambda_1 = 1.429a$, that of the second partial photonic bandgap occurs at $\lambda_2 = 0.685a$, and their separation is $\lambda = 0.744a$ (For more details see Methods). Therefore, to obtain a silk-fibroin inverse opal with visible/IR reflection peaks, the first peak ($\lambda_1 = 1.429a$) should be located within the IR region (> 700 nm) and the second ($\lambda_2 = 0.685a$) should fall into the visible region (400-700 nm) (Fig. 4.2b). In this case, a suitable lattice constant (584 nm < *a* < 1022 nm) should be adopted. Similarly, we can obtain silk-fibroin inverse opals having UV/IR or UV/visible reflection peaks by adopting corresponding lattice constants.

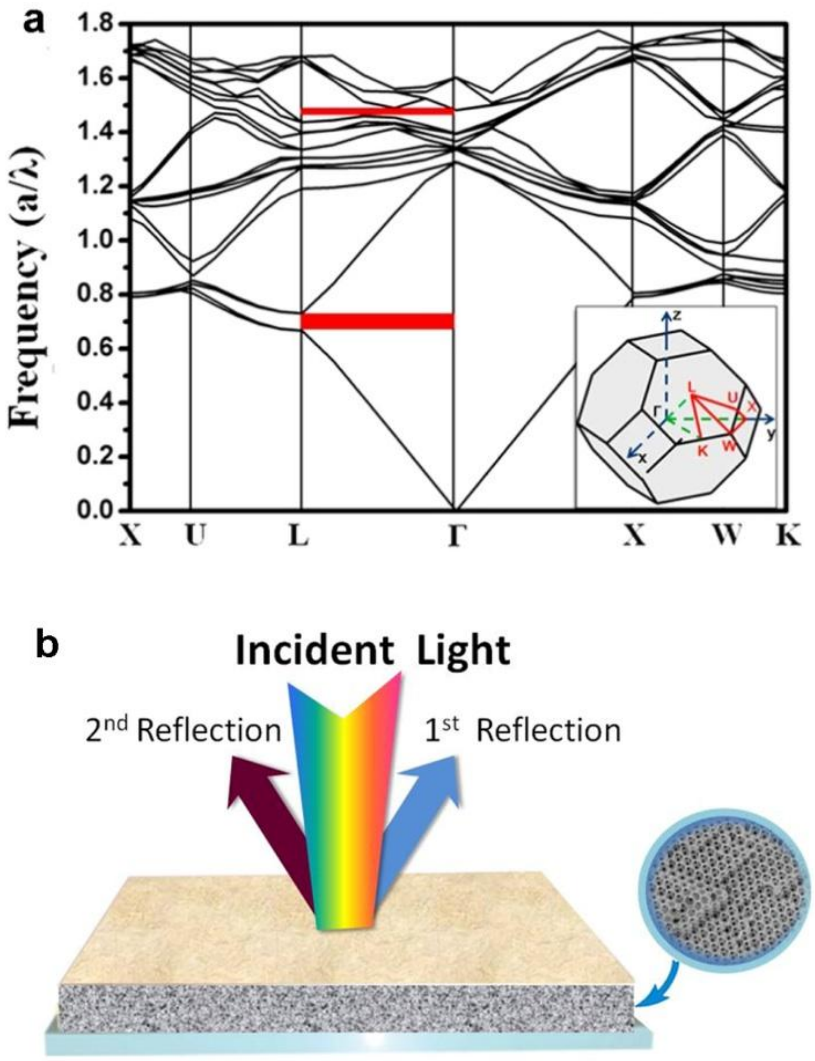

Figure 4.2. a, The calculated photonic band structure of a silk fibroin inverse opal along the high-symmetry points in its first *Brillouin* zone. Two photonic band gaps (red lines) occur along the direction from *Γ* to *L*, one locates at $\lambda_1 = a/0.7$ and the other at $\lambda_2 = a/1.46$, the inset is the first *Brillouin* zone of photonic crystal with the FCC structure. b, Illustration of the bi-reflection effect of the resulted silk fibroin inverse opal.

4.2.2 Colloidal crystal templates

Colloidal crystals with the FCC structure were grown from a given size of monodispered polystyrene colloidal spheres as described in Chapter 2. The growth of colloidal crystals on a given substrate is one of the rate determining steps to acquire silk fibroin inverse opal films, which were achieved through evaporation induced self-assembly process[117,118]. In this session, we focus to demonstrate the colloidal crystals with photonic band gap locate in the visible part. Fig. 4.3a shows the scanning electron microscopic image (SEM) of colloidal crystal fabricated by 240nm colloidal spheres. The sharp peaks of the Fast Fourier Transformation (FFT) in the image (the inset of Fig. 4.3a indicate the fact that the quality of the FCC colloidal crystal is high. Colloidal crystals prepared by polystyrene colloidal spheres of different diameters (D) have the same FCC structure, except the lattice constant. The reflectance spectra of 200nm colloidal crystal and 240nm colloidal crystal are shown in Fig. 4.3b. The reflection peak of 200nm colloidal crystal locates at ~460 nm, which reflect a blue structural color (Fig. 4.3c(i)), and the peak position of 240nm colloidal crystal is ~560nm, reflecting a green structural color (Fig. 4.23(ii)).

The reflection peak of the colloidal crystals can be directly compared with the band gap along the direction from Γ to L in the band structure. From the comparison (Table 4.1), the calculated band structure agrees well with the experimental observations.

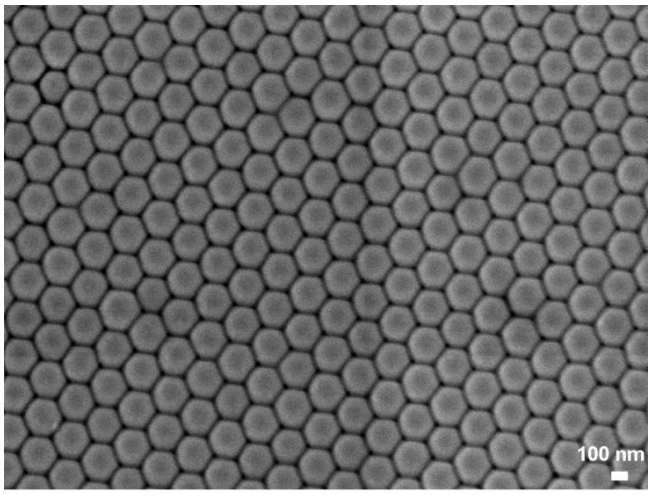

a

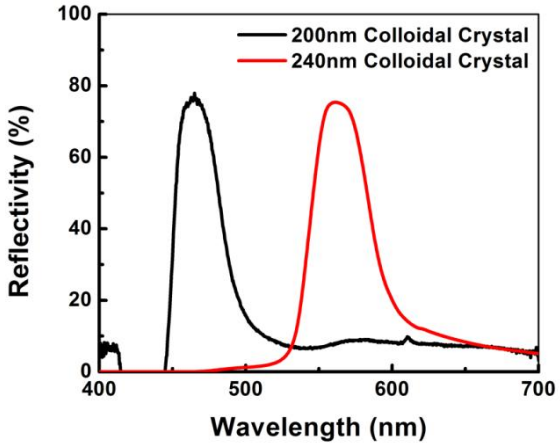

b

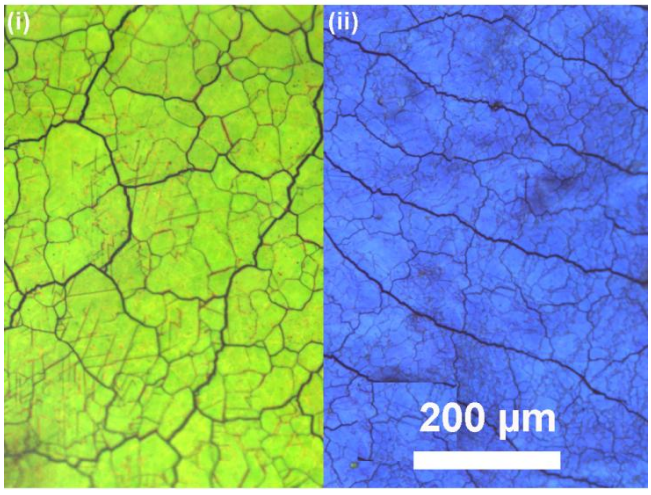

c

Figure 4.3. a, SEM images of 240nm colloidal crystal. b, Reflectance spectra of 200nm and 240nm colloidal crystals. c, Structural color reflected by 200nm and 240nm colloidal crystals.

Colloidal Crystal	Lattice Constant	Theory Calculated Band Gaps	Measured Reflection Peaks
	$a=D*\sqrt{2}$ (nm)	λ=a/0.6 (nm)	(nm)
200 nm	282.8	471	470 (blue)
240 nm	340	565	560 (green)

Table 4.1. Comparison of calculated band structure and measured reflection peak of colloidal crystal.

4.2.3 Silk fibroin inverse opals with bi-structural-color reflection

The procedure of fabrication of silk fibroin inverse opals is introduced in Chapter 2. Fig. 4.4 shows the scanning electron microscopic (SEM) images of a colloidal crystal template and a resulting silk-fibroin inverse opal fabricated using 700 nm colloidal spheres. The sharp peaks in the FFT pattern (the inset of Fig. 4.4a indicate that the quality of the FCC colloidal crystal is high. The SEM images of the silk-fibroin inverse opal at low and high magnifications are displayed in Fig. 4.4b and Fig. 4.4c, respectively, which show the highly ordered hexagonal structure. The sharp FFT pattern (the inset of Fig. 4.4b) also verifies the high quality of the inverse opal. The inset of Fig. 4.4c displays the details of one cavity in the inverse opal structure, where the three channels connecting to the adjacent pores can be seen. This is the corresponding structure giving rise to the bi-structural-color reflection in photonic crystals[119,120]. The transverse cross-section shown in Fig. 4.4d indicates that the thickness of the obtained silk-fibroin inverse opal is about 20 layers of ordered hollow silk-fibroin spheres. Notice that while the

cracking is a common issue in other inverse opals, silk-fibroin inverse opals display significantly improved perfection and the enhanced rupture/crack resistance due to the elastic nature of silk fibroin[121].

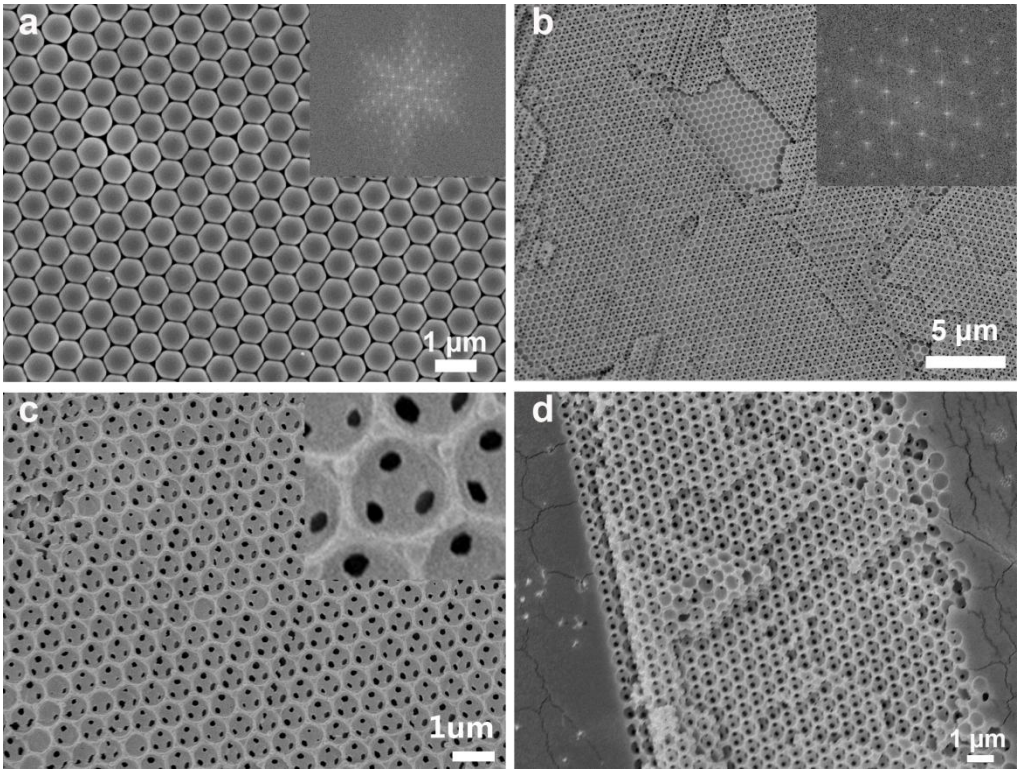

Figure 4.4. Scanning electron microscope (SEM) images of colloidal crystal and silk fibroin inverse opal fabricated by 700nm colloidal spheres. (a) SEM images of the colloidal crystal, the inset - the Fast Fourier Transformation (FFT). (b), (c) Images of the silk fibroin inverse opal with low and high magnifications. The inset in (b) is the FFT of the inverse opal structure. The inset in (c) is the detailed structure of one cavity of the inverse opal structure. (d) Transverse cross section structure of the silk fibroin inverse opal.

In the following, we exemplify that we can attain silk-fibroin inverse opals with bi-structural-color reflection located at UV/visible, UV/IR and visible/IR. In this concern, polystyrene colloidal spheres with different diameters (350 nm, 450 nm, 500 nm and 700 nm) are chosen. Fabricated silk-fibroin inverse opals are characterized both spectrally and optically, shown in Fig. 4.5. The first example is a silk-fibroin inverse opal fabricated with 350 nm colloidal spheres. As shown in Fig.

4.5a, two reflection peaks exist with one at UV (~285 nm) and the other at the visible (~590 nm), showing an orange structural color to our perception. The separation between the two peaks is λ=310 nm. The 450 nm silk-fibroin inverse opal (Fig. 4.5b) gives rise to one peak located in the UV range (~380 nm) and the other in the near IR range (~800 nm). Both are invisible to the human eye. The bi-structural-color reflection of the 500 nm silk fibroin inverse opal (Fig. 4.5c) shows that one peak is located in the visible (~ 430 nm) and the other in the near IR (~870 nm). The visible reflection peak gives rise to a purple structural color. The 700 nm silk-fibroin inverse opal (Fig. 4.5d) should display two reflection peaks with one peak (~ 620 nm) in the visible, producing a red color and the other in IR which is beyond the detection range of our spectrometer.

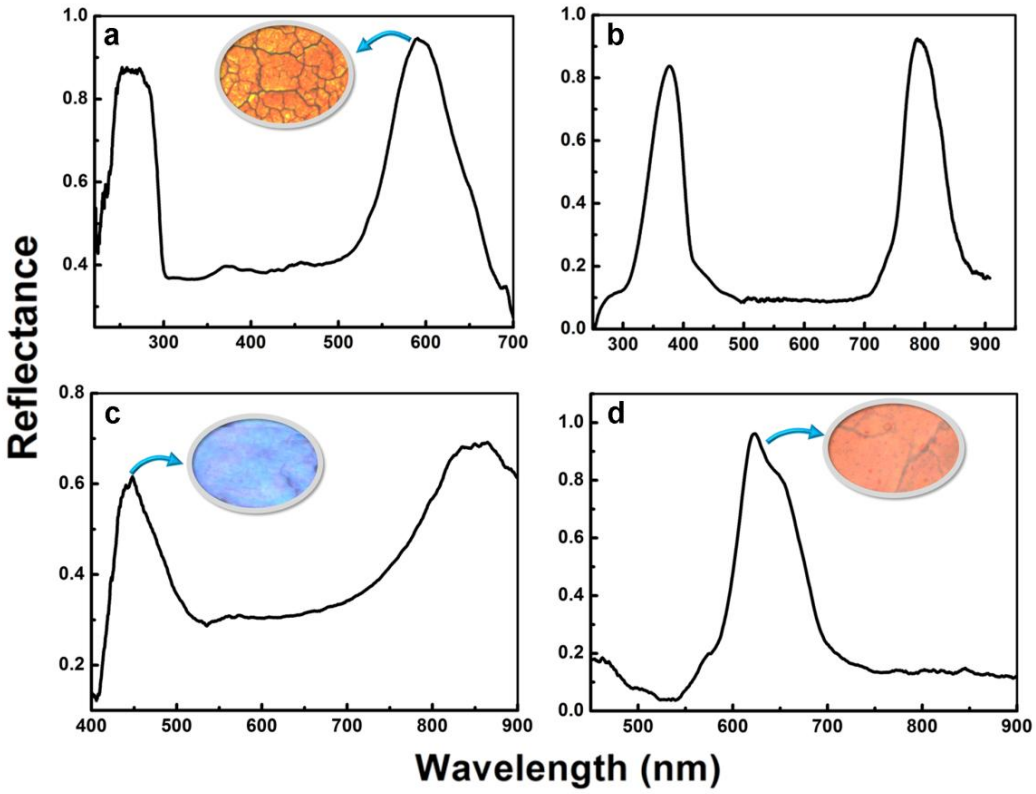

Figure 4.5. The measured reflectance spectra for silk fibroin inverse opals fabricated by 350nm (a), 450nm (b), 500nm (c) and 700nm (d) colloidal spheres, respectively. The inset of (a) is the orange color observed under optical micro-

scope for 350nm silk fibroin inverse opal, the insets of (c) and (d) are purple and red colors produced by 500nm and 700nm silk fibroin inverse opals.

As discussed before, the partial photonic bandgaps are direction-dependent. The two peaks of the bi-structural-color reflection should undergo a blue shift in wavelength with the incident angle changing from normal to oblique. Our experimental results show that as the incident light angle increases, the bi-reflection peaks vary approximately as $\lambda_0 \cos\theta$, where θ is the incident angle and λ_0 is the peak wavelength under normal incidence[118]. For the 700 nm silk-fibroin inverse opal, its angular reflection spectra are measured at different incident angles (0^o-60^o) with respect to the normal of the (111) plane (Fig. 4.6a). The 620 nm peak under normal incidence disappears quickly as θ increases to 15^o. With the further increment of incident angle, another peak appears once θ reaches 45^o. Both peaks undergo a blue shift with the increment of incident angle. The blue shift of the reflection peaks can be understood by the fact that the two partial photonic bandgaps increase their mid-gap frequency along the *L*-*U* direction, implying that the resulting reflection peaks should shift to low wavelengths with the increment of incident angle.

Silk-fibroin inverse opals prepared by polystyrene colloidal spheres of different diameters have the same FCC structure, except the lattice constant. We notice that although the radius of the air spheres in a silk-fibroin inverse opal is determined to a large extent by the radius of colloidal spheres, the SEM images reveal that the actual size of air spheres shrinks about 10-20% compared with the size of colloidal spheres, which also occurs in the preparation of other porous materials[122]. One consequence is that we have to consider the shrink of the lattice constant in the design of a silk-fibroin inverse opal. Moreover, when comparing the measured

reflection peaks with the calculated mid-gap wavelengths of the partial photonic bandgaps along the Γ-L direction, we should take the measured lattice constant. Table 4.2 gives the measured lattice constant of fabricated silk-fibroin inverse opals, and corresponding predicted and measured reflection peaks. It is obvious that the predicted reflection peaks agree well with the measured ones. This indicates ambiguously that the bi-structural-color reflection in silk-fibroin inverse opals stems indeed from the two partial photonic bandgaps along the Γ-L direction.

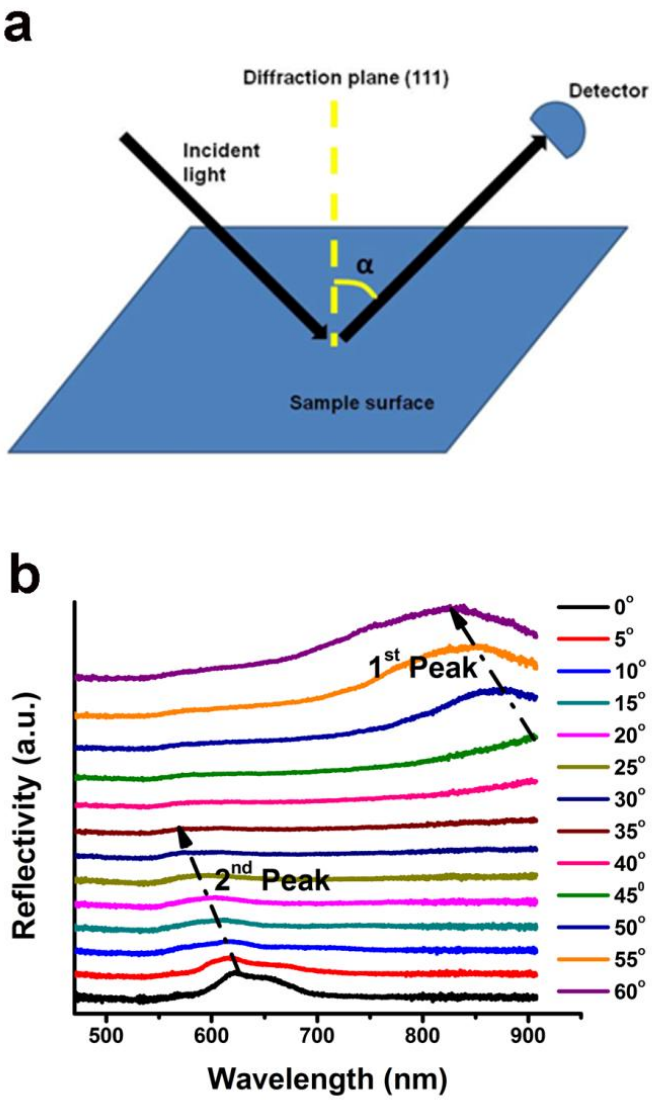

Figure 4.6. Angular resolved reflectance spectra of 700nm silk fibroin inverse opal. a, Geometry of the angle resolved reflectance spectroscopy, b, measured angular reflectance spectra for 700nm silk fibroin inverse opals.

Previously, the silk optical devices are limited to 1D and 2D micropatterning silk-fibroin films (for example, diffraction gratings, microlens arrays, 2D diffractive optics, *etc.*)[116,123,124]. Implementing 3D silk photonic crystals of the inverse opal structure, we can expand silk-fibroin optical devices to the 3D mode. The bi-structural-color reflection effect of silk-fibroin inverse opals can be made for bio-coating materials, tissue engineering and cosmetic applications, *etc.*[125,126]. Furthermore, their partial photonic bandgaps are not limited to the range from UV to near IR, and they can be easily extended to other parts of the spectrum, e.g. far IR, by simply adjusting their lattice constants.

Samples	Measured lattice constant	Calculated mid-gap wavelength		Measured reflection peaks
		λ_1 (1.429a)	λ_2 (0.685a)	
350 nm inverse opal	415 nm	592 nm	284 nm	285 nm & 590 nm
450 nm inverse opal	560 nm	810 nm	383 nm	380 nm & 800 nm
500 nm inverse opal	620 nm	885 nm	424 nm	430 nm & 870 nm
700 nm inverse opal	900 nm	1285 nm	616 nm	620 nm

Table 4.2. Measured lattice constant and comparison of the measured and calculated reflection peaks.

4.2.4 Bring structural color to silk fabrics

By fabricating the silk photonic crystals onto the surface of fabrics, we can produce multi functional fabrics in addition to the vivid structural colors[127]. For instance, we can acquire the UV protective textiles by adjusting the 2nd reflection peak in the UV range. Similarly, the thermal insulating performance can be achieved by locating the 1st reflection peak in the IR range, which will create auto cooling textiles in a hot summer if the structure is generated in the outer layer of textiles. On the other hand, it will preserve our body heat in a cold winter if the IR reflecting structure is generated in the inner layer of textiles.

The band-gaps or the respective reflection peaks will be tuned from ultraviolet to near-infrared by controlling the lattice constants of the photonic crystals. As illustrated in Fig 4.7, the three dimensional face centre cubic opal or inverse opal was constructed on the surface of the silk fabrics by materials assembly. Silk fibroin was used as binding materials to fix the opal or inverse opal on the silk fabrics. Silk fabrics with diversified colors were fabricated by controlling the lattice constants of the opals or inverse opals.

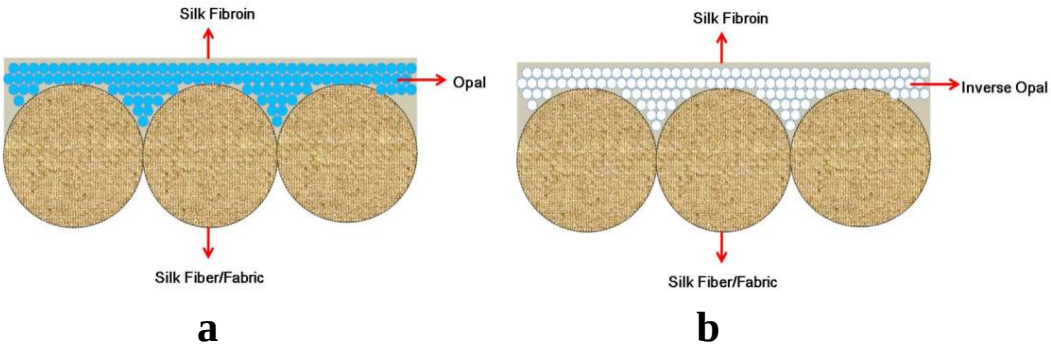

Figure 4.7: Illustration of the diagrams of the structural colored silk fabrics constructed by opal (a) and inverse opal (b).

The UV, visible and NIR reflection peaks indicate the potential applications of structural color in eco-dyeing engineering. The silk opal photonic crystals with a structure of polystyrene (PS) spheres arranged into the ordered FCC structure can be fabricated on the surface of silk fabrics (Fig. 4.8, see Materials and Methods). As mentioned, different reflection peaks (UV, Visible and NIR) of the silk-polystyrene photonic crystals can be achieved by changing the size of colloidal spheres (Fig. 4.9). As two examples, the red and golden colored silk opal fabrics in Fig. 4.8 were fabricated by 240nm and 270nm self assembled colloidal sphere photonic crystals, respectively.

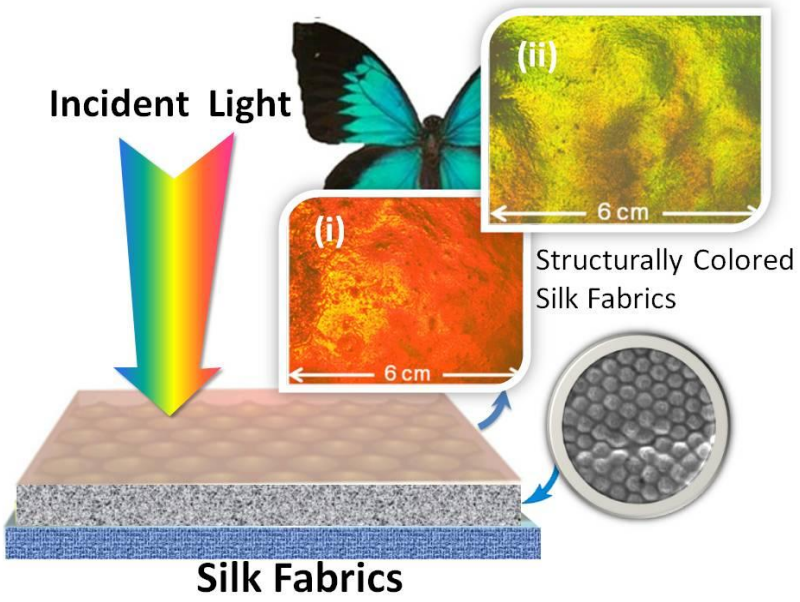

Figure 4.8. Creating silk fabrics with structural color. The silk photonic crystals, wherein PS spheres were arranged into ordered FCC structure inside silk matrix were created on the surface of silk fabrics. The two examples of structural colored silk fabrics withred (i) and golden (ii) colors were fabricated by 240nm and 270nm self assembled colloidal sphere photonic crystals, respectively.

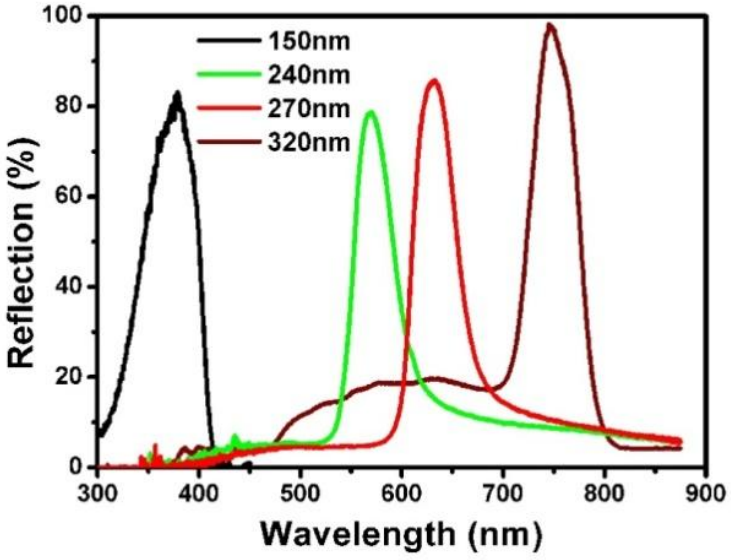

Figure 4.9. Measured reflectance spectra of the silk fabrics with different reflection peaks. The reflection peaks of silk-polystyrene photonic crystals locating in different parts of spectrum can be achieved by changing the size of colloidal spheres. The silk photonic crystal layers fabricated by 150nm colloidal spheres at the surface silk fabrics have a reflection peak at 370nm, which resides in the UV part. The reflection peaks of silk photonic crystals fabricated by 240nm and 270nm colloidal spheres are 560nm (gloden) and 630nm (red), respectively. While silk photonic crystal fabricated by 320nm colloidal spheres has a reflection peak locating at 750nm, which is inside the Near-Infrared part.

4.3 Materials and experimental

Silk fibroin solution preparation:

The production of silk fibroin solution is well documented elsewhere[128]. In general, it began with the purification of harvested cocoons. Sericin was removed from the fibroin strands by boiling the cocoons in a 0.5wt% aqueous solution of sodium biocarbonate for 45 mins. Then, the fibroin bundle was rinsed thoroughly in DI water for several times and allowed to dry overnight. The dried silk fibroin

was dissolved in a saturated solution of lithium bromide (9.3M/L) at 40^{o}C for 1h. The lithium bromide salt was then extracted from the solution through a water-based dialysis cassette for 3 days. And remained particulates were removed through centrifugation (10000rpm, 15mins). The whole process produces 4% w/v silk fibroin solution with excellent quality and stability. The required 2% w/v solution was gotten by diluting the original samples.

Fabrication of silk fibroin inverse opals:

The fabrication methods were described in Chapter 2.

The calculation of the band structures of silk fibroin inverse opals:

The numerical simulations were carried out using commercial software (RSoft Design). The first 20 bands were calculated for the first Brillouin zone of colloidal crystal and silk fibroin inverse opal. For colloidal crystal with a FCC structure, the refractive index of colloidal spheres was taken as 1.59. For the silk fibroin inverse opal, the FCC inverse opal structure was well described by overlapping the shells of silk fibroin, the thickness of silk fibroin shells (d_2) was assumed to be 0.1 with respect to that of air spheres (d_2). The refractive index of silk fibroin was taken as 1.54[31]. The photonic band gap (PBG) is essentially the gap between the air-line and the dielectric-line in the dispersion relation of the PBG system. The photonic band gap for colloidal crystal locates at $a/\lambda = 0.6$; there are two PBGs in the calculated band structure of silk fibroin inverse opal, the 1st order stop gap is at $a/\lambda = 0.7$, and the 2nd order stop gap occurs at $a/\lambda = 1.46$.

Fabricating silk photonic crystals on the surface of silk fabrics:

Polystyrene colloidal suspensions were loaded on the silk fabrics. Prior to loading, silk fabrics were treated through UV radiation for 20 mins to make them

hydrophilic. Self-assembly of the colloidal spheres occurred on the hydrophilic silk fabric surfaces. Then, silk fibroin solution (2% w/v) was loaded; the colloidal crystals were fixed on the surface of silk fabric with the drying of the silk fibroin solution.

Characterization of the synthesized colloidal crystals and silk fibroin inverse opals:

Field emission scanning electron microscope (SEM-JEOL 6700F) was used to characterize the micro-structures of the samples. Optical images were taken by Olympus (BX 61), reflectance measurements were carried out by UV-Vis spectrometer (Ocean Optics 2000) and a homemade angle-resolved reflectance spectrometer.

4.4 Summary

In summary, silk fibroin photonic crystals with the inverse opal structure were chosen to implement a simple and highly effective scheme for the bi-reflection production. Such a scheme takes advantage of two photonic band gaps in the band structure for inverse opals. The positions of the photonic band gaps (reflection peaks), as well as the separation between the two band-gaps can be simply adjusted by tuning the lattice constant of the inverse opal structure or the refractive index of materials. The bi-reflection covering UV/visible, UV/NIR, visible/NIR parts of the spectrum were fabricated by controlling the lattice constant of silk fibroin inverse opals. The strategies of fabricating silk based photonic crystals in eco-dyeing and multi-functionalizing silk fabrics are analyzed.

CHAPTER 5

Humidity Responsive Silk Fibroin Inverse Opal

5.1 Introduction

5.1.1 Responsive photonic crystals

Responsive photonic crystals (RPCs) are materials with photonic band-gap properties that can be tuned by external stimuli[129]. There is a strong demand for photonic materials with properties that can be tuned by external stimuli. These responsive photonic crystals have important applications in areas such as color displays, biological and chemical sensors, inks and paints, and many optically active components[44,130-132]. To create such materials, a stimulus-response mechanism needs to be coupled with the photonic crystal structure.

In the biological world, many animals including amphibians[133,134], insects[135-138]and aquatic animals[139-142]can change their coloration in response to environmental stimuli. For instance, the elytra golden color of beetles *Tmesisternus isabellae* is produced by a multilayer in scales which are densely imbricated on the elytra. This structural golden color can change to red in the dry state which is due to the water infiltration and swelling of the period of the multilayer[18]. The adaptive values of color change are usually regarded as camouflage, signal communication, conspecific recognition, and reproductive behavior.

5.1.2 Humidity induced cyclic contraction of silk

Supercontraction and cyclic contraction are two interesting inherent properties of the dragline spider silk. 'Supercontraction' describes the dramatic shrinking of dragline silk fibers when wetted[143-145]. In restrained silk fibers, supercontraction generates substantial stresses of 40–50 MPa above a critical humidity of ~70% relative humidity (RH). This stress may maintain tension in webs under the weight of rain or dew and could be used in industry for robotics, sensor technology, and other applications. Cyclic contractions allow the fiber act as a high performance mimic of biological muscles[146]. These contractions are actuated by changes in humidity alone and repeatedly generate work 50 times greater than the equivalent mass of human muscle. The simplicity of using wet or dry air to drive the biomimetic silk muscle fibers and the incredible power generated by silk offer unique possibilities in designing lightweight and compact actuators for robots and micromachines, new sensors, and green energy production. Cyclic contraction also occurs in silkworm silk. Subjecting silkworm silk fiber to high humidity from initial low humidity does not induce supercontraction, consistent with previous reported study due to its lack of proline amino acids[147]. Further cycling of humidity levels results a cyclical pattern of high and low tensile stresses respectively similar to that of spider dragline silk.

This cyclic response produces high forces, which are completely reversible, that can be precisely controlled through humidity alone. Cyclic contraction results from a reversible loss of water during drying. The mechanism behind supercontraction and cyclic contraction in spider silk is hypothesized in depth by Blackledge[146]. Given the high similarities between spider silk and silkworm silk in terms of them being semi-crystalline polymer amino acid composition[148], the

mechanism behind cyclic mechanism in silkworm silk would be similar to that in spider silk. In short, the initial exposure to humidity results in infiltration of water molecules into the silk fiber. The water molecule first binds itself to the random coil within the amorphous region disrupting the relatively weak hydrogen bonding. This relaxes the silk and explains the dip in the stress strain curve when silk is first expose to humidity at critical threshold of 70-75%. Upon drying immediately, water molecules are lost only from the random coil region, rebuilding hydrogen bonds in the process that immobilize the silk molecules, contracting the fiber in the process. Subsequent wetting results in water molecules binding itself to the random coil region and breaking the hydrogen bonds, therefore causes the silk fiber to relax. In short, high humidity in cyclic contraction causes the silk to relax if the mobilization of silk molecules enabled by moisture is limited to the random coils region within the silk, by breaking the relatively weak hydrogen bonds. Cyclic contraction is also observed in natural fibers such as cotton and hair whereas it is not observed in hydrophobic synthetic fibers such as polyethylene and acrylic[149]. This suggests that cyclic contraction depends on the hydrophilic nature of the constituent amino acids.

The cyclic contraction of silkworm fibers further enhanced the potential applications of silk muscles as they are already available in commercial quantities. Silk fibres from a silkworm cocoon can be processed into various forms, ranging from gels, strands, sponges and blocks, through to foams and films[124]. Among the many possible material forms, silk films are of particular interest for biomedical optics because of their transparency and surface flatness, which are a direct result of the all-aqueous processing of the protein. These silk films are fabricated by applying the water-based fibroin solution onto a substrate by either spin-coating or casting.

The solution is left to dry in air until it crystallizes into a film with a thickness that can be controlled to be from a few nanometres to hundreds of micrometres.

In this Chapter, we aim to bio-mimic the response ability of natural structural color by our silk fibroin inverse opals. As discussed in chapter 4, the two reflection peaks of a silk fibroin inverse opal can be tuned by changing its lattice constant, namely the size of colloidal spheres. Nevertheless, for a ready-made silk fibroin inverse opal, adjusting the reflection peaks is an issue. In the following, we will explore a simple and effective approach to tune the reflection peaks by external stimuli. In this regard, we will take the advantage of the humidity induced cyclic contraction property of silk to achieve responsive silk fibroin inverse opals.

5.2 Results and discussion

5.2.1 Humidity induced cyclic contraction of spider silk, silkworm silk and silk fibroin film

The cyclic contractions of spider silk and silkworm silk were performed using the setup as illustrated in Fig 5.1. To control humidity, the sample was put into a humidity chamber. The tensile stress was directly measured by a micro-mechanical tester. The mechanical response of the cyclic contractions of single silkworm silk fiber and spider silk fiber at high (80%) and low (30%) humidity levels were measured (Fig 5.2). The test began at a higher humidity level, the tensile stresses of silkworm silk fiber and spider silk fiber were measured as lower values, 2.5 MPa and 7 Mpa, respectively. Drying (30%) induces stress (contraction) of both silkworm silk (~25 MPa) and spider silk (~35 MPa). The fibers then

relax back to its original tension as humidity is subsequently increased and the cycles repeat itself. It follows that both the fibers do not show obvious fatigue even after approximate 11000 s (three repetitions) under tension.

Regenerated silk film preserved most if not all the composition of amino acids present in silkworm silk. Thus cyclic contraction should be observed in regenerated silk film. Fig 5.3 describes the cyclic contraction of regenerated silk film using the same setup as shown in Fig 5.1. The test began at a lower humidity level, initial drying induces stress (contraction) of ~5 MPa. The film then relaxes back to its original tension as humidity is subsequently increased and the cycle repeat itself. It follows that the silk fibroin film does not show obvious fatigue even after approximate 6500 s (three repetitions) under tension. Compared with silkworm fiber, the cyclic contraction of silk film is much smaller and the response time is longer. This might be caused by the random distribution of the β-crystals in silk film.

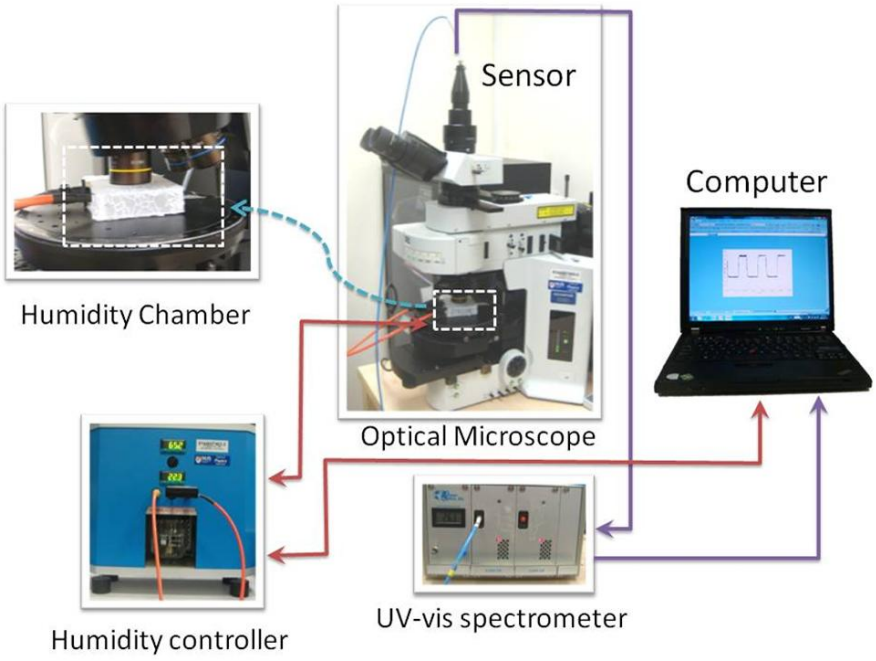

Figure 5.1. Experiment setup for the measurements of the cyclic contraction (i) and reflectance spectra (ii) of regenerated silk films under humidity controller.

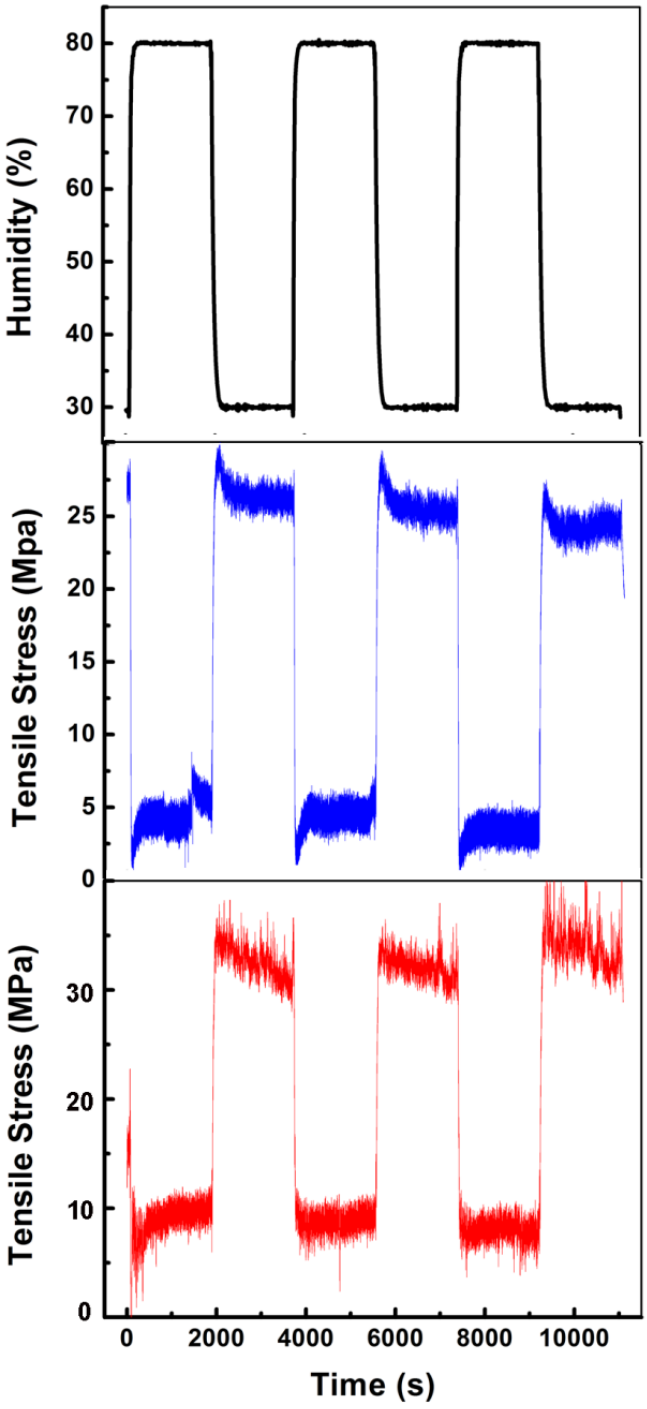

Figure 5.2. Cyclic contractions of silkworm silk fiber (blue line) and spider silk fiber (red line)

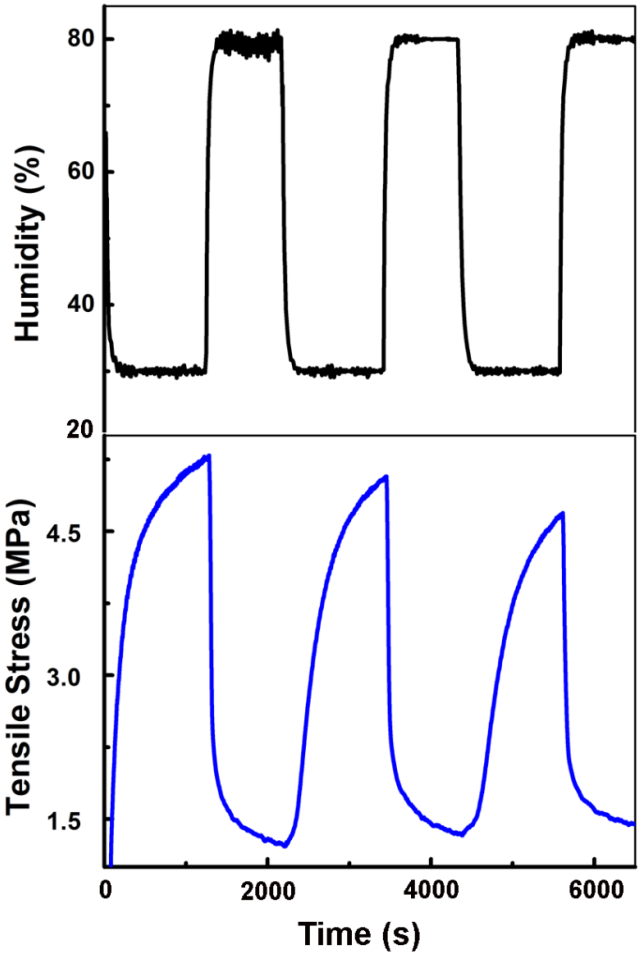

Figure 5.3. Cyclic tensile stress response of silk fibroin film to humidity (blue curve); measured reflection peaks for 350nm silk fibroin inverse opal with changes of humidity levels (red curve).

5.2.2 Humidity responsive silk fibroin inverse opals

Our purpose is to tune the optical properties of silk fibroin optical devices utilizing its cyclic contraction. To fulfill this, three-dimensional (silk fibroin inverse opal with structural color will be employed. As discussed in Chapter 4, there are two reflection peaks for silk fibroin inverse opals: one locates at λ_1 = a/0.7, and the other locates at λ_1 = a/1.46. In this study, silk fibroin inverse opals fabricated by 300nm and 350nm colloidal crystals are employed as their first reflection peaks locates in the visible part, which can be detected and character-

ized easily. The optical properties of the samples at different humidity levels were directly measured using the setup in Fig 5.1(ii), where an optical microscope (ii) was connected to a spectrometer.

The reflection spectra and optical microscope images of a 350 nm silk-fibroin inverse opal are obtained using the set-up illustrated in Fig. 5.1(ii). Our results indicate that the humidity induced cyclic contraction of silk-fibroin films can be utilized to precisely control the optical property of silk-fibroin inverse opals. As shown in Fig. 5.4 (red curve), the visible reflection peak of the 350 nm silk fibroin inverse opal exhibits a red shift with increasing humidity level. At a high humidity level, the decrease of the tensile stress would induce the swelling of silk fibroin, leading to the expansion of the silk-fibroin shells in the inverse opal (as illustrated in the inset of Fig. 5.6b). Besides, the water infiltration would change the refractive indices of the silk fibroin shells and air spheres. Therefore, the red-shift of the visible reflection peak of the 350 nm silk-fibroin inverse opal results from the water infiltration induced the swelling of silk-fibroin shells and the changes of refractive indices. On contrary, the reflection peak of the silk-fibroin inverse opal exhibits a blue shift with lowering of the humidity level. This will give rise to a precise tune of the reflection peak of a silk-fibroin inverse opal within a certain range. During the cyclic process, the shift of the reflection peak is also reversible. The structural-color change in silk-fibroin inverse opals at different humidity levels is quite similar to that of longhorn beetles *Tmesisternus isabellae*[18].

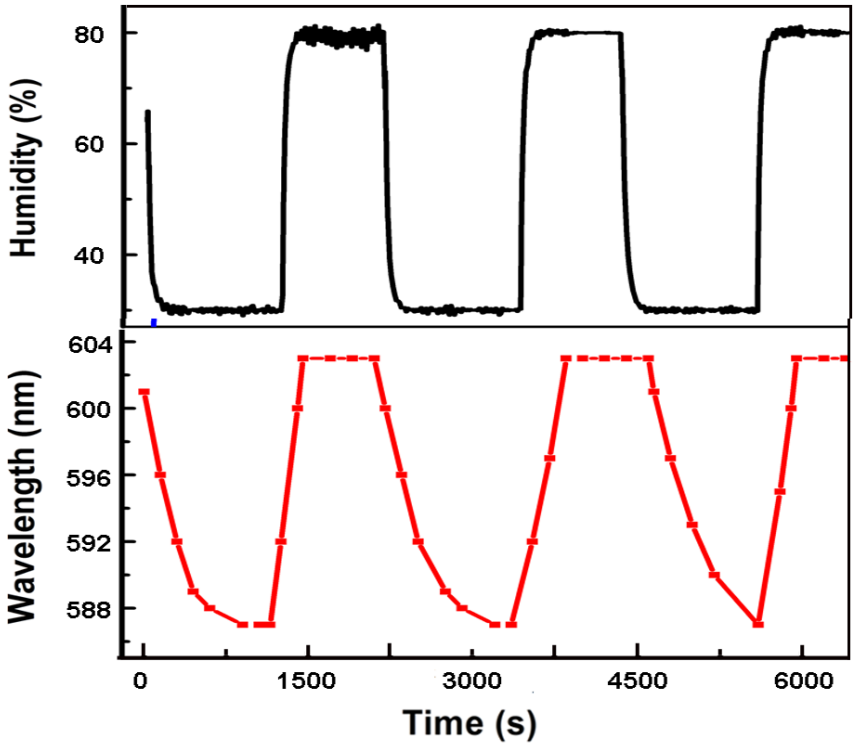

Figure 5.4. The responsible reflection peak of 350 nm silk fibroin inverse opal during the humidity cyclic process.

The reflectance spectra and optical images of the silk fibroin inverse opals under different humidity levels (from 30% to 80% with a segment of 10%, Fig 5.5) were recorded to characterize the humidity sensitive property of silk fibroin inverse opal. Fig 5.6a shows the selected reflection spectra of the 350nm silk fibroin inverse opal under different humidity levels. It is found that the spectrum undergoes a blue-shift with decrement of the humidity level, which is further proved by the structural color changes from orange (80% RH) to yellow reflection color (30% RH). The reflectance spectrum for the UV peak of 350 nm silk fibroin inverse opal under different humidity levels is also measured. As shown in Fig. 5.6b, the reflection peaks of the silk-fibroin inverse opal decrease almost linearly with lowering humidity level: The visible reflection peak of 350 nm silk fibroin

inverse opal shifts from 603 nm to 587 nm, and the UV peak shifts from 291 nm to 285 nm with lowering the humidity level from 80% to 30%.

Fig 5.6c shows the selected reflectance spectra of the 300nm silk fibroin inverse opal under different humidity levels. The spectra also undergo a blue shift with decrement of humidity levels. The structural color changes from green to blue as humidity lowering from 80% to 30%. The visible reflection peak of 300nm silk fibroin inverse opal shifts from 539 nm to 514 nm with lowering the humidity level from 80% to 30%; the UV peak of 300 nm silk fibroin inverse opal shifts from 246 nm to 258 nm. The reflection peak also shifts almost linearly with decrement of humidity levels (Fig. 5.6d).

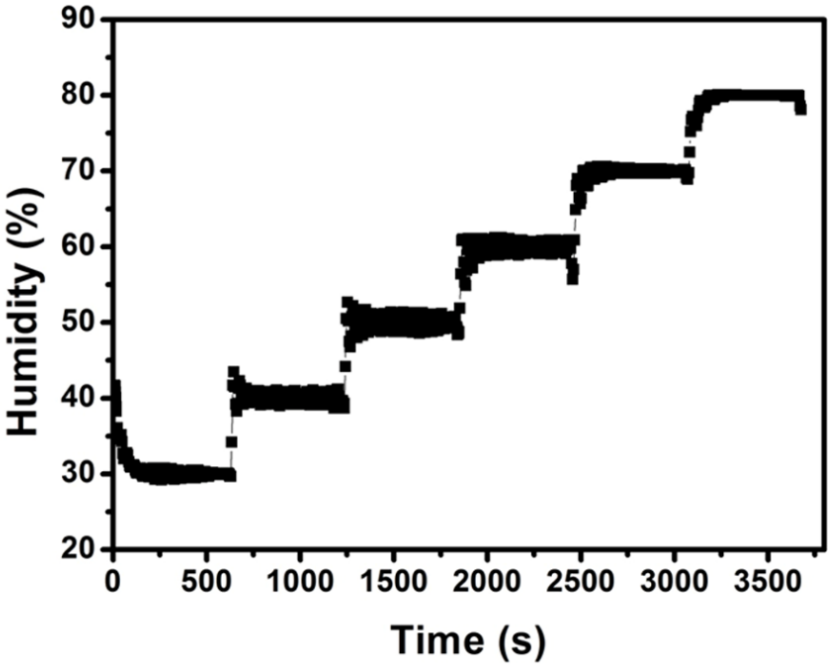

Figure 5.5. Step increment of humidity level from 30% to 80% RH.

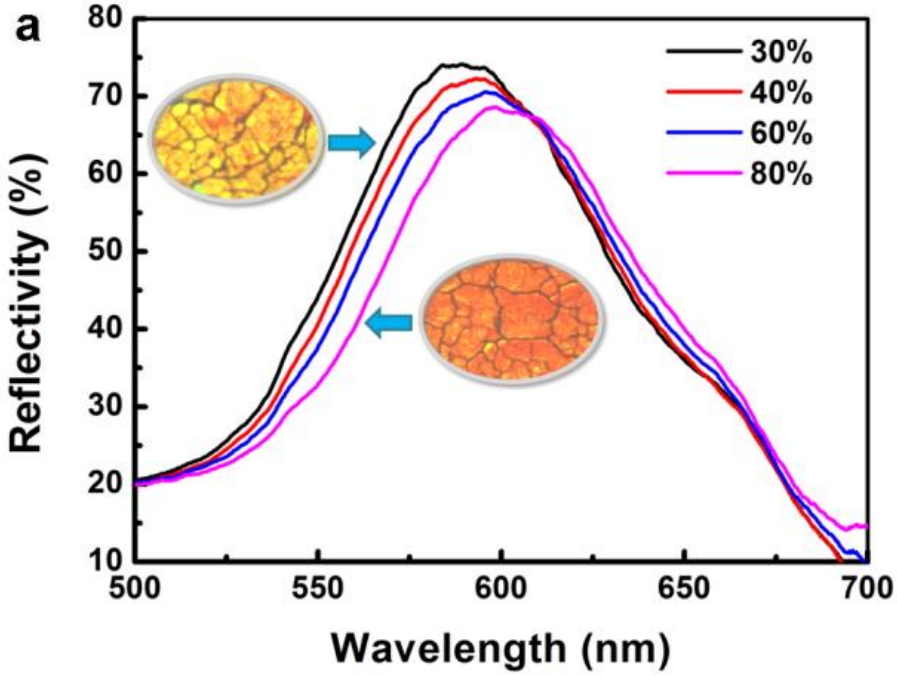
a
Reflectivity (%)
Wavelength (nm)
30%
40%
60%
80%
10
20
30
40
50
60
70
80
500
550
600
650
700

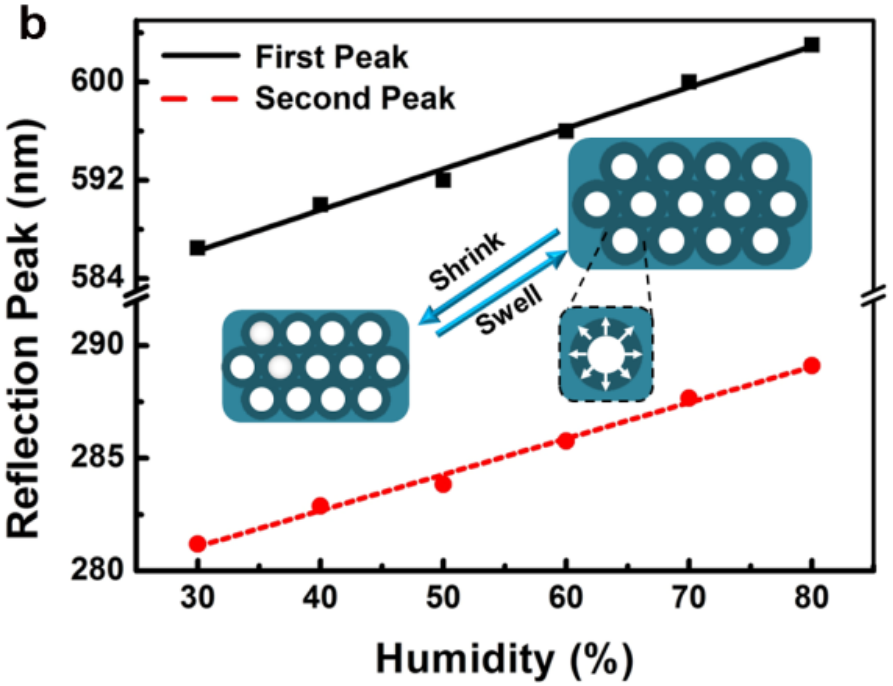
b
First Peak
Second Peak
Reflection Peak (nm)
Humidity (%)
Shrink
Swell
280
285
290
584
592
600
30
40
50
60
70
80

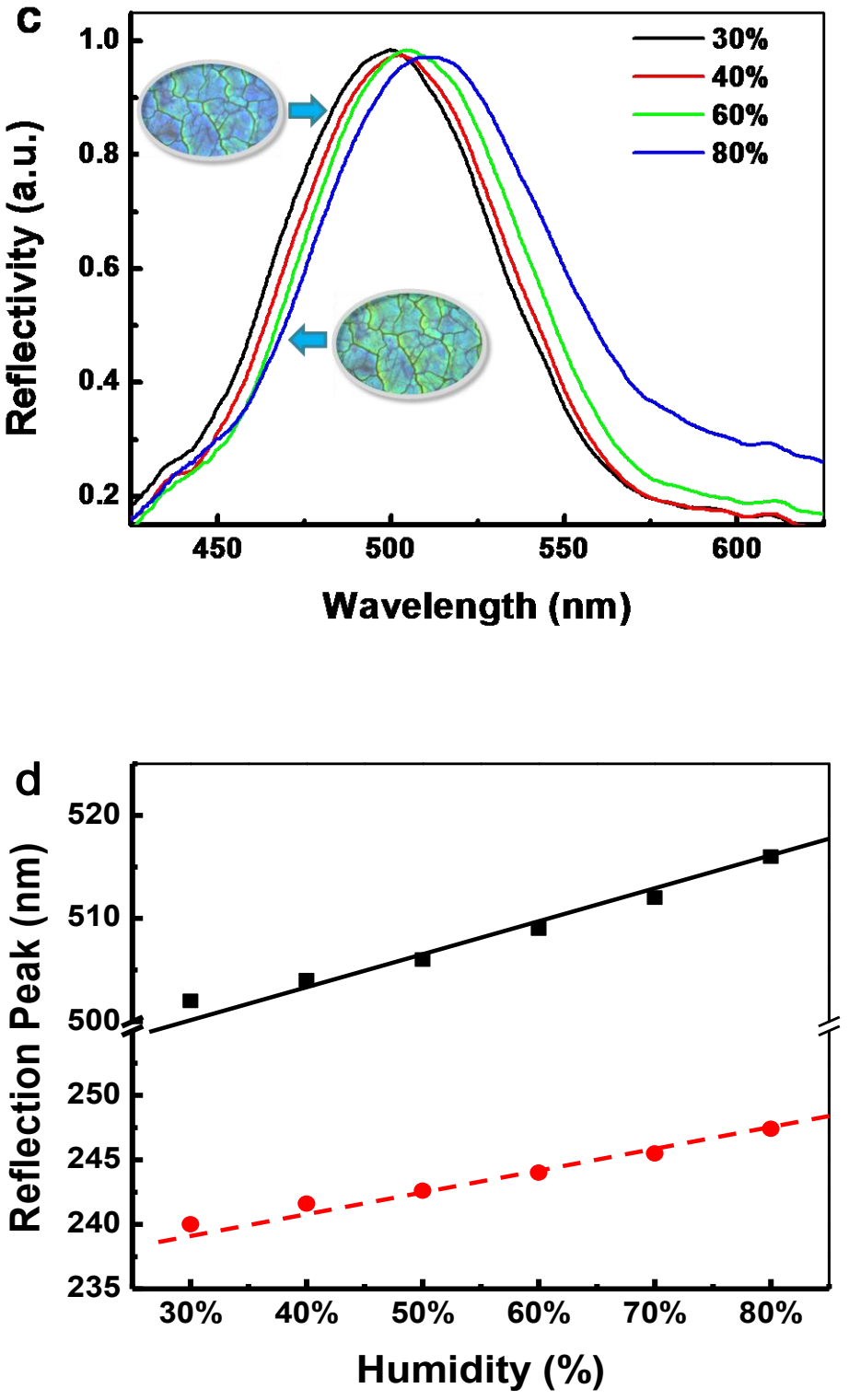

Figure 5.6. Reflectance spectra for 350 nm (a) and 300 nm (c) silk fibroin inverse opals under different humidity levels. The insets are optical microscope images for silk fibroin inverse opal under 30% and 80% humidity levels. Linear relationship between the reflection peaks and humidity levels for 350nm (c) and 300nm (d)

silk fibroin inverse opals. The inset in (b) is the illustration of the swelling and shrinking of the silk fibroin.

Notice that tunable photonic crystals, including opals and inverse opals, may be used in the future as optical switches for the full automation of optical circuits when significant improvements towards the quality of photonic crystals and their response time are realized. Vehicles covered with such materials may be able to dynamically change their colors and patterns to match their surroundings. Such materials might also be embedded in banknotes or other security documents for antifraud purposes. The hidden information cannot be revealed until an external stimulus is applied. The photonic effect can also be used as a mechanism to develop chemical and biological sensors for detecting target analyses by outputting optical signals. These types of crystals may also find great use as active color units in the fabrication of flexible display media, including both active video displays and rewritable paper that can be reused many times.

5.3 Experimental

To measure the stress generated by fibers and silk fibroin film under changing humidity levels, silk fiber (both spider silk fiber and silkworm silk fiber), silk fibroin film (thickness: 0.1 mm, width: 1.5 mm) fabricated by drying regenerated silk fibroin solution were adhered to cardboard mounts across 20mm gaps. Measurements of stress were performed using Instron S5762A (Model 5525X Mini Horizontal Test System) with a 0.5 N Load Cell. The Instron was custom fit with an in house built chamber that controlled humidity with a range of ~30–80% RH. Humidity in the environmental chamber was regulated by the triton technology

humidity generator and controller. The 350 nm and 300nm silk fibroin inverse opals were put into a custom humidity controlled chamber, the surface of which is transparent. The optical microscope images of the samples were captured by optical microscope (Olympus BX61), and the reflectance spectra were recorded by a spectrometer (Ocean Optics, USB 2000) which was connected to the optical microscope.

5.4 Summary

In this Chapter, it is found that not only the spider silk fiber and silkworm silk fiber, but also the silk fibroin film exhibit humidity induced cyclic contraction. Our experimental results indicate that humidity responsive silk fibroin inverse opals are achieved by taking advantage of the humidity induced cyclic contraction property of silk fibroin. At a high humidity level, the water infiltration induced swelling of silk fibroin shells in the inverse opal structure and changes of refractive indices would induce a red-shift of the structural reflection peaks of silk fibroin inverse opals. On the contrary, the structural reflection peaks would undergo a blue-shift with lowering the humidity level.

CHAPTER 6

Dynamic Control of Fluorescence Emission from Silk Fibroin Inverse Opal

6.1 Introduction:

Organic fluorescent dyes-based biological devices are used widely for measurements in optoelectronic, life-science research and drug discovery, with applications that include DNA gene expression analysis, protein microarrays for disease biomarker detection, cell imaging and materials coating[150-153]. Unfortunately, it can often be troublesome, limiting the performance of fluorescence in applications. Therefore, techniques that can dynamically control fluorescence light emission become essential in fluorescence applications. One aspect is to develop techniques that can more effectively excite and extract the light emitted by the fluorophores, therefore possibly leading to improvements in high-brightness light sources, and lowering of the detection limits in biological assays. Many strategies have been applied in pursuit of this aim, including fluorescence resonance energy transfer (FRET)[154,155], photoinduced fluorescence enhancement (PFE)[156,157] and surface plasmon resonance (SPR) of metal nanoparticles[158,159]. More recently, enhancement of fluorescence emission from probes on the surface of photonic crystals is studied[160,161]. On the other hand, inhibiting unwanted light emission and redistributing the energy into useful forms are desirable objectives for advances in some applications[162]. For example, in lasers, which are coherent light sources,

light emission that does not couple to the lasing mode raises the lasing threshold and becomes unwanted noise. As a result, there is a strong motivation to achieve dynamic control over the light emission: inhibit it when it is not desired or alternatively enhance it when it is required.

Fluorescence occurs when an orbital electron of a molecule, atom or nanostructure relaxes to its ground state by emitting a photon of light after being excited to a higher quantum state. The rate of this relaxation is determined by the photonic density of states and the electric-filed intensity at the position of emitters. Therefore, when trying to control fluorescence, it is important to control the number of optical modes and their spatial distribution relative to the emitter. In photonic crystals, which have a three- or two-dimensional periodic variation of their refractive index on a length-scale comparable to the wavelength of interest, the light emission is modified because the periodic structures can be used control optical modes. Especially, the band-gap of a photonic crystal can inhibit light propagation in a certain direction for a given frequency. Hence, PCs have been reported to dynamically control the spontaneous emission of embedded optically-active materials (dyes, semiconductors, *etc.*) [163-166]. If a material that ordinarily emits light is introduced into a 3D PC, the light emission will be completely inhibited. Additionally, enhancement of photoluminescence by PCs has been reported by photonic defects[167] and minimizing surface recombination losses of quantum dots at low temperature[168]. More recently, Klimov et al.[169] have reported amplified spontaneous emission in semiconductor nanocrystals uniformly coated on opal polystyrene surfaces by reducing the group velocity at the edge of the photonic band-gap. Ganesh *et al.*[170] demonstrated the enhanced fluorescence emission from quantum dots on a photonic crystal surface. The enhancement was

due to a combination of high-intensity near electric fields and strong coherent scattering effects, which were attributed to leaky eigenmodes of the PCs. Up to now, how to fully control the fluorescence emission, names as combine the two effects (inhibition and enhancement) in one system is still an open question in the fluorescence applications. Besides, how to construct a bio-compatible material with the aforementioned property is very important in bio-medical applications.

Silk fibers from silkworm are creating new opportunities in bio-technology field by offering a widely available, robust, biocompatible and implantable material, which can be processed into various forms, ranging from gels, strands and sponges, through to foams and films[55,58,171,172]. Among of the many possible material forms, silk fibroin films are of particular interest for optics and photonics applications [124]. In this chapter, we will study the "inhibition" and "enhancement" effects of the fluorescence by embedding organic fluorescent dye Rhodamine 6G (R6G) into silk fibroin inverse opals. We demonstrate that the fluorescence emission could be strongly enhanced by a factor of ~40 by combining the dyes into silk fibroin inverse opals, while within the photonic band gap (PBG) of the inverse opals, the fluorescence emission is inhibited. Therefore, the fully control of fluorescence emission from Rhodamine 6G can be achieved by the inverse opal structure.

6.2 Results and discussion:

6.2.1 Inhibition of fluorescence by silk fibroin inverse opals

The fluorescence dyes employed in this study is Rhodamine 6G. Its lasing range is 555 to 585 nm with a maximum at 566nm, which is often used as a tracer

dye within water to determine the rate and direction of flow and transport. The excitation radiation in this study is UV light. R6G are embedded inside silk fibroin inverse opals with different lattice constants. As discussed in Chapter 4 & 5, the visible reflectance spectrum of 350 nm silk fibroin inverse opal ranges from 560 nm to 590 nm, which overlaps with the lasing range of R6G. In this section, 350 nm silk fibroin inverse opal combined with R6G molecules is chosen to study the influence of PBG on the emission behaviors of fluorescence.

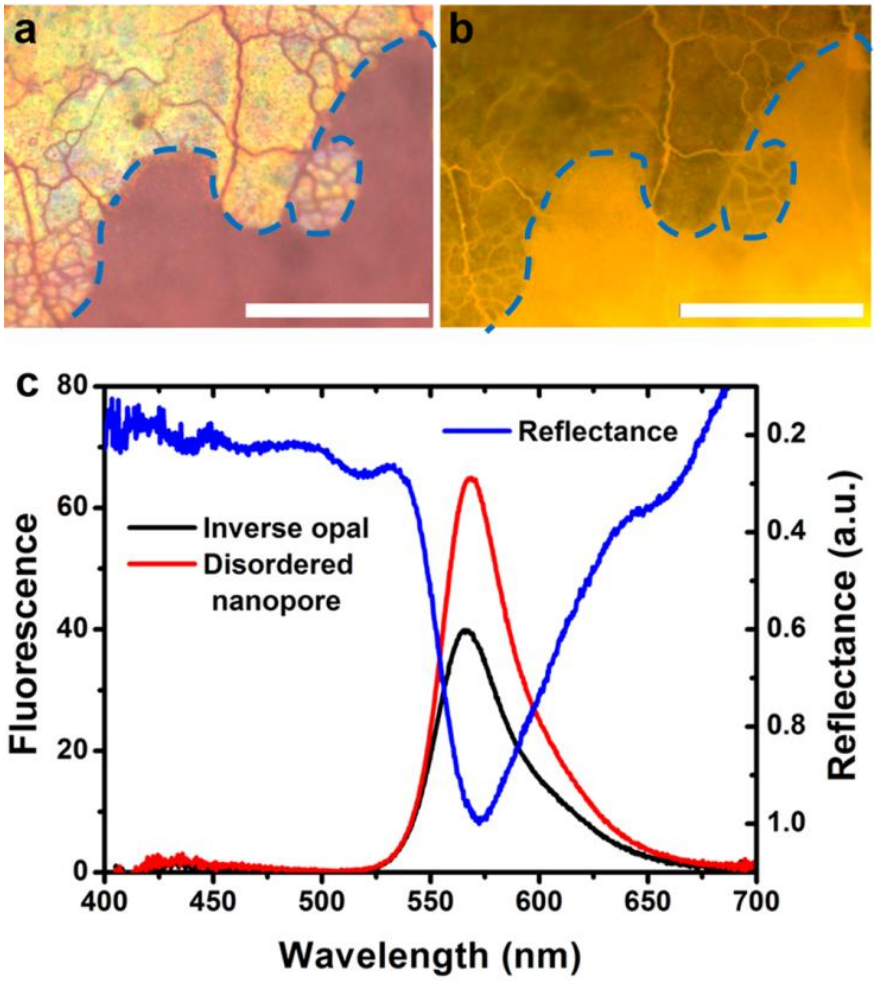

Figure 6.1. a, Bright field optical microscope image of the samples: the region with orange structural color has ordered inverse opal structure and the region without color has disordered structure. b, Fluorescence optical microscope image of the samples. Scale bar: 100 μm. c, Measured reflectance spectrum and fluorescence emission spectra for the samples.

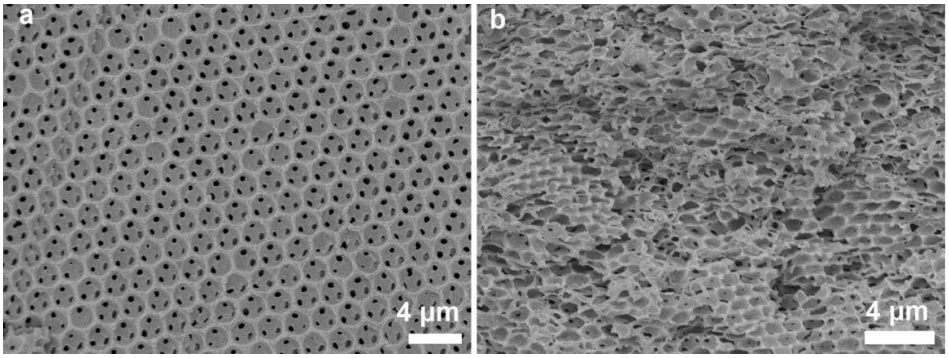

Figure 6.2. a, SEM image of 350 nm silk fibroin inverse opal structure. b, SEM image of the silk fibroin with disordered structure.

Fig. 6.1a is the bright field optical microscope image for the sample: the region with orange structural color is the 350 nm silk fibroin inverse opal, its SEM image is displayed in Fig. 6.2a. The region without structural color is the disordered silk fibroin nano-pore structure (Fig. 6.2b), which is considered to be the control sample. The fluorescence optical microscope image of the same regions are also captured (Fig. 6.1b). It is obvious that the disordered region is brighter than the ordered inverse opal region, meaning the fluorescence emission of R6G is inhibited by the ordered inverse opal structure. The reflection peak of the 350 nm silk fibroin inverse opal, measured with a light incident along its normal surface, locates at ~575 nm (Fig. 6.1c, blue line). The fluorescence emission spectra of the R6G embedded inside the inverse opal structure and disordered nano-pore structure are also measured (Fig. 6.1c, red and black lines). Same to the fluorescence optical microscope image, the emission intensity from the 350 nm inverse opal region is smaller than the control sample. As light transportation is not allowed in the PBG of a photonic crystal, the emission of the fluorophores cannot be extracted from the inside of the inverse opal, except those on the surface of the inverse opal. There should be a layer of silk fibroin above the inverse opal structure, and the emission from the 350 nm silk fibroin inverse opal structure as seen in the

fluorescence optical microscope image and fluorescence emission spectrum comes from this silk fibroin layer.

6.2.2 Enhancement of fluorescence from inverse opal structure

The experimental results in 6.2.1 indicate that the emission of fluorescent dyes can be inhibited by the band gaps of inverse opal structure. To demonstrate the enhancement of fluorescence emission from the inverse opal structure, we measured the fluorescence emission spectra of R6G embedded inside 500nm silk fibroin inverse opals with different NO. of layers. From the results in Chapter 4, the PBGs of 500 nm silk fibroin inverse opals do not overlap with the emission spectrum of R6G. 5 layers, 15 layers and 20 layers 500 nm inverse opals were fabricated with the same quantity of fluorophores and silk fibroin to carry out the measurement. As indicated in the scanning SEM images in Fig. 6.3, there exists a silk fibroin layer above the inverse opal structure, the thickness of this layer decrease with increment of the NO. of inverse opal layers. Besides, silk fibroin film embedded with the same quantity of R6G without inverse opal structure was employed as a reference. As could be seen from the fluorescence emission spectra in Fig. 6.4a, there is a remarkable fluorescence enhancement by embedding the fluorophores into the inverse opal structures. Moreover, the fluorescence intensity increases with the increscent of the layers of the inverse opal. Detailed analysis of the relationship between fluorescence intensity and the layers of inverse opal reveals that fluorescence emission intensity increases linearly with the increscent of the layers (the inset of Fig. 6.4a): a 10-fold enhancement for 5 layers, 30-fold enhancement for 15 layers and 40-fold enhancement for 20 layers silk fibroin inverse opals. As shown in the fluorescence optical microscope images (Fig. 6.3b),

the silk fibroin inverse opals are much brighter than the silk fibroin film, and the brightness increases gradually with increasing the layers. The enhancement property of fluorescence emission is also observable for silk fibroin inverse opals with different lattice constants.

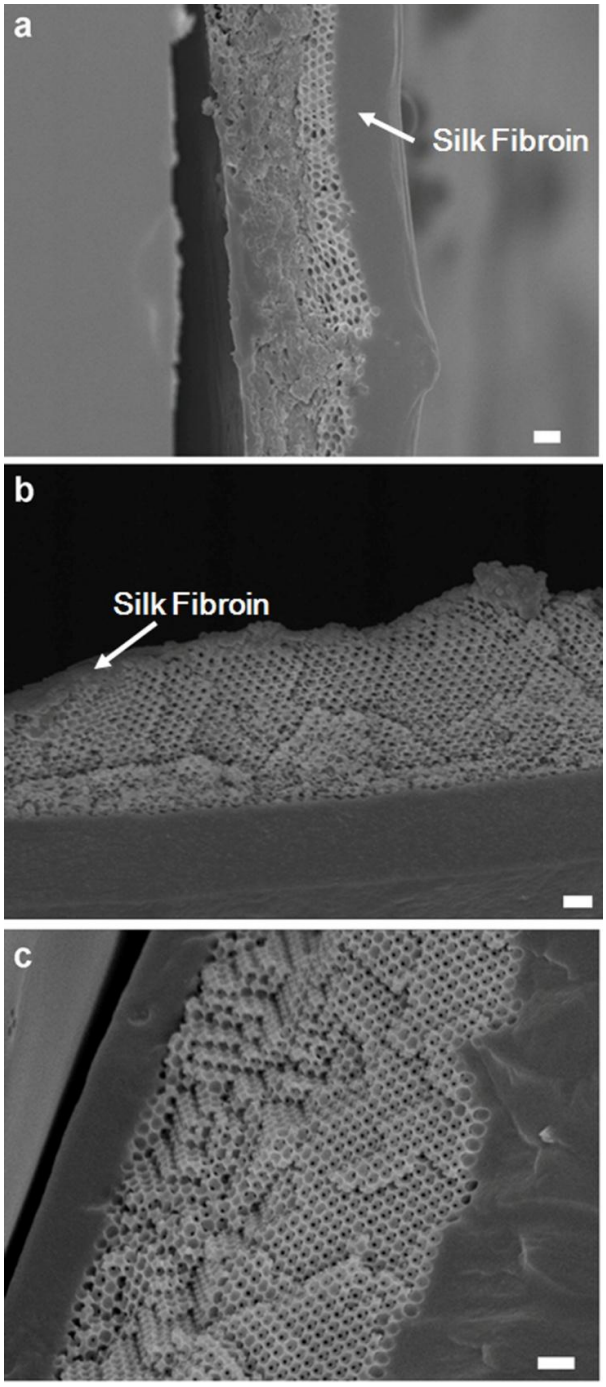

Figure 6.3. 500nm silk fibroin with different layers of inverse opal. 5 layers (a), 15 layers (b) and 20 layers (c). Scale bar: 1 μm.

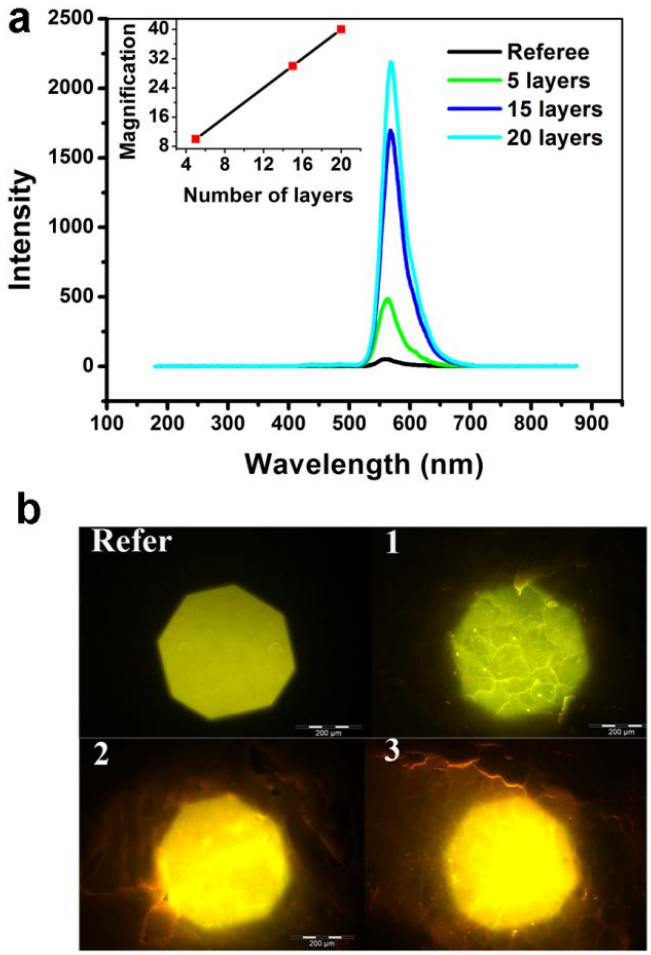

Figure 6.4. a, Fluorescence emission spectra of the R6G embedded into the silk fibroin inverse opals with different thicknesses. Inset of (a) indicates the relationship between the fluorescence emission enhancement and the thicknesses of the silk fibroin inverse opals. b, Fluorescence optical microscopy images of the silk fibroin film and silk fibroin inverse opals with different layers.

When a light wave incidents on an object, the light wave could be reflected, absorbed or transmitted. In our study, the UV radiation incidents on the samples, the absorbed light is utilized to excite the fluorophores, forming the fluorescence. Therefore, the ratio of the absorbance is very important in fluorescence emission. For the silk fibroin film (the reference sample) which is transparent, most of the excitation light is reflected or transmitted, only a small part of the incident light is absorbed and utilized to excite the fluorescent molecules (Fig. 6.5a). However, for

the silk fibroin inverse opal, most of the excitation light is absorbed and can be effectively utilized to excite the fluorescent molecules inside the sample (Fig. 6.5b). The efficient utilization of the incident excitation light leads to the enhancement of fluorescence emission by the inverse opal structure.

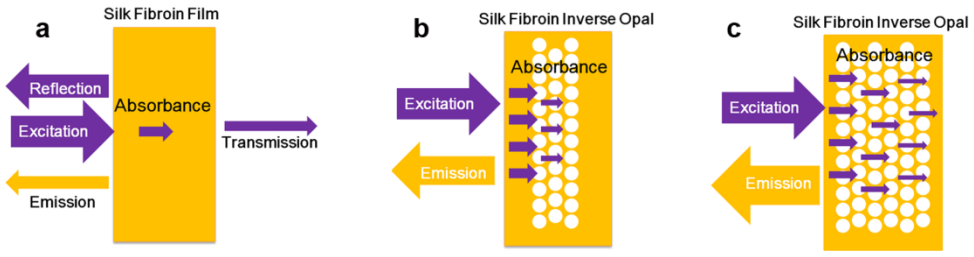

Figure 6.5. Schematic illustration of the excitation and emission of R6G in silk fibroin film (a), silk fibroin inverse opal with fewer layers (b) and more layers (c).

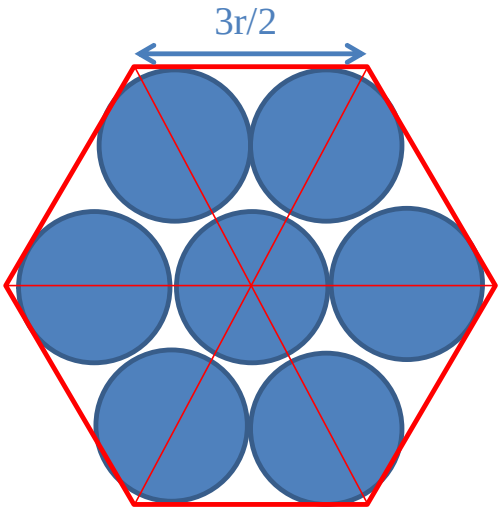

Figure 6.6. Schematic illustration of the increased surface area factor of silk fibroin inverse opal compared with solid silk fibrin film.

Due to the presence of the air spheres, the total air volume (surface area) of silk fibroin inverse opal is increased compared with silk fibroin film without inverse opal structure. A simplified physical model is constructed to make a rough esti-

mated of the ratio of the total surface area of a silk fibroin inverse opal over that a flat silk fibroin film, which is given by:

$$n \times 4\pi r^2 \Big/ 9\sqrt{3r^2}/4 = 3.22n \qquad (6.1)$$

Where n is the No. of layers of the silk fibroin inverse opals, r is the radius of the air spheres, $4\pi r^2$ is the surface area of hollow silk fibrin sphere, and $9\sqrt{3r^2}/4$ is the area of the projection of one sphere on solid silk fibroin film (Fig. 6.6). Fig. 6.5b and c exemplify the silk fibroin inverse opals with fewer and more inverse opal layers, respectively. Consistent with the SEM images, there is a silk fibroin layer above the inverse opal structure, and this layer is thicker in the silk fibroin inverse opal with less layers. As light flux can propagate more freely in air than in silk fibroin, the excitation UV light can transmit a longer distance in a silk fibroin with more inverse opal layers, therefore, more fluorophores can be excited, leading to the increment of the fluorescence emission intensity. From Eq. (6.1), the total surface area increases linearly with the No. of layers of the silk fibroin inverse opals. This result can explain why the fluorescence emission intensity increases linearly with the increscent of thickness of the silk fibroin inverse opals. From the experiment result, the slope between the fluorescence emission intensity and the thickness of the silk fibroin inverse opals is 2. The difference between the calculation and experiment results should be due to the existence of the silk fibroin layer above the inverse opal structure. According to the analysis, the volume factor has no relationship with the radius of air spheres; as a result, the fluorescence enhancement property of silk fibroin inverse opals is not related to their lattice constant, consisting with the experimental observations. The overall enhancement of fluorescence intensity comes from combination effects of en-

hanced excitation and increased surface area due to the presence of inverse opal structure[173,174].

6.3 Experimental

Sample preparation:

The samples used in this study are silk fibroin inverse opals embedded with fluorophores (R6G). The fabrication procedure of fluorescent silk fibroin inverse opals is similar as described in Chapter 4, the only difference is before casting and penetrating into the voids of colloidal crystals, silk fibroin solution is mixed with fluorescence dyes (10^{-4} mol/L).

Experimental setup:

Fluorescence optical images were captured by fluorescence optical microscope (Olympus BX 61) excited by UV light; fluorescence spectra under normal incident light is also captured by fluorescence optical microscope which is connected with a spectrometer (Ocean Optics USB 2000).

6.4 Summary

We studied the fluorescence emission of R6G embedded into silk fibroin inverse opals. The fluorescence emission can be strongly enhanced by coupling the emitters into inverse opal structure. Moreover, the fluorescence enhancement increases linearly with the increscent of the thickness of the inverse opals (the NO. of layers) with a factor of 2. By adjusting the band gaps of the photonic crystals to overlap the fluorescence emission spectrum, the fluorescence emission is inhibited. Due to the high promising property of silk fibroin in the field of bio-

technology[112,175,176], the combination of fluorescent dyes and silk fibroin photonic crystals broaden applications of fluorescent dyes in biological systems. Such a fluorescence enhancement and inhibition mechanism controlled by biomaterial would be invaluable to the future design in biomedical devices.

CHAPTER 7

Conclusions and Outlook

7.1 Conclusions

This thesis aims to investigate the mechanisms and find an effective way to mimic of the bi-structural-color reflection. Focus is given to explore the structural origin of bi-structural-color reflection for two species of *Papilio* butterflies. Silk fibroin inverse opals with two PBGs are fabricated to mimic the bi-structural-color reflection effect.

In Chapter 3, our experiment and calculation analysis reveal that the two species of *Papilio* (*P.Ulysess* and *P.Blumei*) butterflies wings exhibit of bi-structural-color reflection. The blue wing scales of *P.Ulysess* reflect green and UV light which is produced by concavities and ridges respectively. The green color seen from *P.Blumei* is a mixture of yellow and blue colors reflected by the flat portions and inclined sides of concavities. By varying the nanostructures and the profile of their concavities, the two breeds of butterflies exhibit totally different optical properties. Under optical microscope, the flat concavities in *P.Ullysess*' wings create single color with no polarization effect. The concavities in *P.Blumei* generate a bi-color reflection. Through a bi-reflection process, the blue color reflected from the inclined sides of *P.Blumei's* concavities undergoes a polarization conversion. When illuminated with UV-Vis light, *P.Ullysess* gives rise to two reflection peaks. One originates from the concavities, and the other from the ridges. These two peaks shift their positions under different illumination condi-

tions (normal and 45^{o} incident light). On the other hand, *P.Blumei* reflects similar reflectance spectra under these two cases illumination due to the special profile of the concavities. The function of nano-complex structures of the black wing scales in *P.Blumei* in light absorption was also discussed.

The construction of an effective and simple way to produce bi-structural-color reflection is the main aim of Chapter 4. The bi-structural-color reflection is successfully mimicked by fabricating silk fibroin inverse opals with two photonic band gaps. The positions of the photonic band gaps (reflection peaks), as well as the separation between the two band-gaps can be simply adjusted by tuning the lattice constant of the inverse opal structure or the refractive index of materials. The bi-reflection covering UV/visible, UV/NIR, visible/NIR parts of the spectrum are fabricated by controlling the lattice constant of silk fibroin inverse opals. The bi-structural-color reflection effect of silk-fibroin inverse opals can be made for bio-coating materials, tissue engineering and cosmetic applications; due to their biological and optical advantages of silk fibroin. By constructing silk based photonic crystals on the surface of silk fabrics, the potential applications of structural color on eco-dyeing and multi-functional fabrics are also demonstrated in this chapter.

As discussed in Chapter 4, the two reflection peaks of a silk-fibroin inverse opal can be altered by changing its lattice constant, namely the size of colloidal spheres. Nevertheless, for a ready-made silk-fibroin inverse opal, tuning the reflection peaks is an important issue. We presented a simple and effective approach to tune the reflection peaks by external stimuli in Chapter 5. In this regard, we take the advantages of the humidity induced cyclic contraction of silk fibroin to achieve responsive silk-fibroin inverse opals. Our results indicate that the humidity

induced cyclic contraction of silk-fibroin films can be utilized to precisely control the optical property of silk-fibroin inverse opals. At high humidity level, the water infiltration induced the swelling of silk fibroin shells in the inverse opal structure and changes of refractive indices induce a red-shift of the reflection peaks of silk fibroin inverse opals. On contrary, the reflection peaks of the silk-fibroin inverse opal exhibits a blue shift with lowering of the humidity level. This gives rise to a precise tune of the reflection peak of a silk-fibroin inverse opal within a certain range.

The understanding of structural origin of the two species of *Papilio* butterflies has broad biological implications. And the mimicking of bi-structural-reflection using silk fibroin opens up new opportunities in bio-coating materials, tissue engineering and cosmetic applications. Especially, the humidity responsive silk photonic crystal may find great applications as active color units in the fabrication of flexible display media in the future.

In Chapter 6, we studied the light controlling property of photonic crystals by combining fluorescent dyes into silk fibroin inverse opals. It was found that the fluorescence emission can be strongly enhanced by coupling the emitters into inverse opal structure. Moreover, the fluorescence enhancement increases linearly with the increscent of the thickness of the inverse opals (the NO. of layers) with a factor of 2. By adjusting the band gaps of the photonic crystals to overlap the fluorescence emission spectrum, the fluorescence emission is inhibited. Due to the high promising property of silk fibroin in the field of bio-technology, the combination of fluorescent dyes and silk fibroin photonic crystals broaden applications of fluorescent dyes in biological systems. Such a fluorescence enhancement and

inhibition mechanism controlled by biomaterial would be invaluable to the future design in biomedical devices.

7.2 Future work

Although we have conducted extensive investigation on the bi-structural-color reflection effect, and explored effective way to bio-mimic this effect, there are still some work need to be further done to fully apply its advantages to nature and industry.

1: In chapter 3, we discussed the structural colors mixing (double reflection) of two species of *Papilio* butterfly, however, there are more mysterious phenomena in nature than we can image. More efforts should be focused on exploring the special properties of natural structural color, such as the environmental responsive structural color, polarization sensitive structural color, *etc.*

2: As discussed in chapter 4, we have applied structural color to silk fabrics. However, a thick layer of colloidal crystal needs to be constructed on the surface of fabrics to achieve a high structural reflectivity, limiting its light and cozy performances. In the future work, try to improve the quality of photonic crystal and reduce its thickness need to be considered.

3. Due to the synthesis process of silk fibroin inverse opals with bi-structural-color reflection, it is hard to achieve samples with large quantity, limiting its industry applications. More effective and simple way need to be invented to synthesis bi-structural-color reflection materials in the future work.

4. In Chapter 5, we successfully tuned the reflection peaks of silk fibroin inverse opals by external stimuli: humidity, however, the response is not so obvious. Alternative way need to be adopted to achieve response photonic crystal with

excellent performance. For instance, PH responsive silk fibroin inverse opals could be fabricated by mixing PH sensitive polymers during the synthesis process, *etc*

5. The mechanisms of the fluorescent enhancement by combing the dyes into silk fibroin inverse opals need to further investigated and studied.

6. More efforts can be devoted to apply the silk fibroin with bi-structural-color effect in cosmetics by further improving the quality and quantity of silk fibroin inverse opals.7. The biomedical applications of the organic dyes in photonic crystals can be further studied by transplant them into tissues.

References

1. Hooke, R. *Micrographia* (Reprinted by Dover Publications, Inc., New York, 2003).
2. Newton, I. *Opticks* (Reprinted by Dover Publications, Inc., New York, 1992).
3. Fox, D. L. *Animal biochromes and structural colors* (University of California, Berkely, 1976).
4. Ghiradella, H. Light and Color on the Wing - Structural Colors in Butterflies and Moths. *Appl Optics* **30**, 3492-3500 (1991).
5. Berthier, S. *Iridescences: The Physical Colors of Insects* (Springer, New York, 2007).
6. Kinoshita, S., Yoshioka, S. & Miyazaki, J. Physics of structural colors. *Rep Prog Phys* **71**, 076401 (2008).
7. Parker, A. R. 515 million years of structural color. *J Opt a-Pure Appl Op* **2**, R15-R28 (2000).
8. Parker, A. R. Bird coloration, vol 1, Mechanism and measurements, vol 2, Function and evolution. *Tls-Times Lit Suppl*, 4-4 (2006).
9. Srinivasarao, M. Nano-optics in the biological world: Beetles, butterflies, birds, and moths. *Chem Rev* **99**, 1935-1961 (1999).
10. Vukusic, P. & Sambles, J. R. Photonic structures in biology. *Nature* **424**, 852-855 (2003).
11. Born, M., Wolf, E. *Principles of optics: electromagnetic theory of propagation, interference and drffraction of light* (Cambridge university press, Cambridge, 1999).
12. Rayleigh. L, On the Reflection of Light from a Regularly Stratified Medium. *Roy Soc Proc* **A93,** 565 – 577 (1917).
13. Li, Y. Z. *et al.* Structural origin of the brown color of barbules in male peacock tail feathers. *Phys Rev E* **72**, 010902 (2005).

14. Vukusic, P., Sambles, J. R. & Lawrence, C. R. Structural color - Color mixing in wing scales of a butterfly. *Nature* **404**, 457-457 (2000).

15. Vukusic, P., Sambles, R., Lawrence, C. & Wakely, G. Sculpted-multilayer optical effects in two species of Papilio butterfly. *Appl Optics* **40**, 1116-1125 (2001).

16. Wong, T. H., Gupta, M. C., Robins, B. & Levendusky, T. L. Color generation in butterfly wings and fabrication of such structures. *Opt Lett* **28**, 2342-2344 (2003).

17. Zi, J. *et al.* Coloration strategies in peacock feathers. *P Natl Acad Sci USA* **100**, 12576-12578 (2003).

18. Liu, F., Dong, B. Q., Liu, X. H., Zheng, Y. M. & Zi, J. Structural color change in longhorn beetles Tmesisternus isabellae. *Opt Express* **17**, 16183-16191 (2009).

19. Vukusic, P. Evolutionary Photonics with a Twist. *Science* **325**, 398-399 (2009).

20. Liu, F. *et al.* Inconspicuous structural coloration in the elytra of beetles Chlorophila obscuripennis (Coleoptera). *Phys Rev E* **77**, 012901 (2008).

21. Vukusic, P., Sambles, J. R., Lawrence, C. R. Optical classification of microstructure in butterfly wing scales. *Photonics Science News* **6**, 61-66 (2000).

22. Vukusic, P., Sambles, J. R., Lawrence, C. R. & Wootton, R. J. Quantified interference and diffraction in single Morpho butterfly scales. *P Roy Soc Lond B Bio* **266**, 1403-1411 (1999).

23. Kinoshita, S. & Yoshioka, S. Structural colors in nature: The role of regularity and irregularity in the structure. *Chemphyschem* **6**, 1442-1459 (2005).

24. Yoshioka, S., Kinoshita, S. Effect of Macroscopic Structure in Iridescent Color of the Peacock Feathers. *Forma* **17**, 169-181 (2002).

25. Yablonovitch, E. Inhibited Spontaneous Emission in Solid-State Physics and Electronics. *Phys Rev Lett* **58**, 2059-2062 (1987).

26. Xie, Z. Y., Sun, L. G., Han, G. Z. & Gu, Z. Z. Optical Switching of a Birefringent Photonic Crystal. *Adv Mater* **20**, 3601-3604 (2008).

27. Choi, S. S., Morris, S. M., Huck, W. T. S. & Coles, H. J. Simultaneous red-green-blue reflection and wavelength tuning from an achiral liquid crystal and a polymer template. *Adv Mater* **22**, 53-56, (2010)..

28. Arsenault, A. C., Puzzo, D. P., Manners, I. & Ozin, G. A. Photonic-crystal full-color displays. *Nat Photonics* **1**, 468-472 (2007).

29. Guthauser, B., Bergen, N., Radice, W. J., Brunswick, N. *Cosmetic compositions with structural color.* United States patent (1994).

30. Huang, J. Y., Wang, X. D. & Wang, Z. L. Controlled replication of butterfly wings for achieving tunable photonic properties. *Nano Lett* **6**, 2325-2331 (2006).

31. Chen, Y. *et al.* Iridescent large-area ZrO(2) photonic crystals using butterfly as templates. *Appl Phys Lett* **94**, 053901 (2009).

32. Ge, H. L., Song, Y. L., Jiang, L. & Zhu, D. B. One-step preparation of polystyrene colloidal crystal films with structural colors and high hydrophobicity. *Thin Solid Films* **515**, 1539-1543 (2006).

33. Xie, R. G. & Liu, X. Y. Controllable Epitaxial Crystallization and Reversible Oriented Patterning of Two-Dimensional Colloidal Crystals. *J Am Chem Soc* **131**, 4976-4982 (2009).

34. Wijnhoven, J. E. G. J. & Vos, W. L. Preparation of photonic crystals made of air spheres in titania. *Science* **281**, 802-804 (1998).

35. Kolle, M. *et al.* Mimicking the colorful wing scale structure of the Papilio blumei butterfly. *Nat Nanotechnol* **5**, 511-515 (2010).

36. Sato, O., Kubo, S. & Gu, Z. Z. Structural Color Films with Lotus Effects, Superhydrophilicity, and Tunable Stop-Bands. *Accounts Chem Res* **42**, 1-10 (2009).

37. Kim, H. *et al.* Structural color printing using a magnetically tunable and lithographically fixable photonic crystal. *Nat Photonics* **3**, 534-540 (2009).

38. Lakhtakia, A., Martin-Palma, R. J., Motyka, M. A. & Pantano, C. G. Fabrication of free-standing replicas of fragile, laminar, chitinous biotemplates. *Bioinspir Biomim* **4**, 034001 (2009).

39. Wang, J. X. *et al.* Simple fabrication of full color colloidal crystal films with tough mechanical strength. *Macromol Chem Physic* **207**, 596-604 (2006).

40. You, B., Wen, N. G., Shi, L., Wu, L. M. & Zi, J. Facile fabrication of a three-dimensional colloidal crystal film with large-area and robust mechanical properties. *J Mater Chem* **19**, 3594-3597 (2009).

41. Wang, J. X., Wen, Y. Q., Hu, J. P., Song, Y. L. & Jiang, L. Fine control of the Wettability transition temperature of colloidal-crystal films: From superhydrophilic to superhydrophobic. *Adv Funct Mater* **17**, 219-225 (2007).

42. Wang, J. X., Wen, Y. Q., Feng, X. J., Song, Y. L. & Jiang, L. Control over the wettability of colloidal crystal films by assembly temperature. *Macromol Rapid Comm* **27**, 188-192 (2006).

43. Wang, J. X., Zhang, Y. Z., Wang, S. T., Song, Y. L. & Jiang, L. Bioinspired Colloidal Photonic Crystals with Controllable Wettability. *Accounts Chem Res* **44**, 405-415 (2011).

44. Fudouzi, H. & Xia, Y. N. Colloidal crystals with tunable colors and their use as photonic papers. *Langmuir* **19**, 9653-9660 (2003).

45. Velev, O. D. & Kaler, E. W. Structured porous materials via colloidal crystal templating: From inorganic oxides to metals. *Adv Mater* **12**, 531-534 (2000).

46. Holland, B. T., Blanford, C. F., Do, T. & Stein, A. Synthesis of highly ordered, three-dimensional, macroporous structures of amorphous or crystalline inorganic oxides, phosphates, and hybrid composites. *Chem Mater* **11**, 795-805 (1999).

47. Holland, B. T., Blanford, C. F. & Stein, A. Synthesis of macroporous minerals with highly ordered three-dimensional arrays of spheroidal voids. *Science* **281**, 538-540 (1998).

48. Holland, B. T., Abrams, L. & Stein, A. Dual templating of macroporous silicates with zeolitic microporous frameworks. *J Am Chem Soc* **121**, 4308-4309 (1999).

49. Johnson, S. A., Ollivier, P. J. & Mallouk, T. E. Ordered mesoporous polymers of tunable pore size from colloidal silica templates. *Science* **283**, 963-965 (1999).

50. Altman, G. H. et al. Silk-based biomaterials. *Biomaterials* **24**, 401–416 (2003).

51. Vollrath, F. & Knight, D. P. The effect of spinning conditions on the mechanics of a spider's dragline silk. *Nature* **410**, 541–548 (2001).

52. Shao, Z. & Vollrath, F. Suprising strength of silk fiber. *Nature* **418**, 741(2002).

53. Wang, X., Kluge, J. A., Leisk, G. G. & Kaplan, D. L. Sonication-induced gelation of silk fibroin for cell encapsulation. *Biomaterials* **29**, 1054–1064 (2008).

54. Kim, U. J. et al. Silk-based biomaterials for tissue engineering. *Biomacromolecules* **5**, 786–792 (2004).

55. Jin, H. J., Fridrikh, S. V., Rutledge, G. C. & Kaplan, D. L. Electrospinning *Bombyx mori* silk with poly(ethylene oxide). *Biomacromolecules* **3**, 1233–1239 (2002).

56. Jin, H. J. et al. Water-stable silk films with reduced β-sheet content. *Adv. Func. Mater.* **15**, 1241–1247 (2005).

57. Wang, X., Kim, H. J., Xu, P., Matsumoto, A. & Kaplan, D. L. Biomaterial coatings by stepwise deposition of silk fibroin. *Langmuir* 21, 11335–11341 (2005).

58. Jiang, C. et al. Mechanical properties of roubst ultrathin silk fibroin films. *Adv. Func. Mater.* **17**, 2229–2237 (2007).

59. Shoji, S. & Kawata, S. Photofabrication of three-dimensional photonic crystals by multibeam laser interference into photopolymerizable resin. *Appl Phys Lett* **76,** 2668 (2000)

60. Xia, Y., Gates, B., Yin, Y. & Lu, Y. Monodispersed colloidal spheres: old materials with new applications. *Adv Mater* **12,** 693-713 (2000)

61. Schroden, R. C., Al-Daous, M., Blanford, C. F. & Stein, A. Optical properties of inverse opal photonic crystals. *Chem Mater* **14,** 3305-3315 (2002)

62. Lpez, C. Three-dimensional photonic bandgap materials: semiconductor for light. *J Opt A* **8,** R1 (2006)

63. Halaoui, L. I., Abrams, N. M. & Mallouk, T. E. Increasing the conversion efficiency of dye-sensitized TiO_2 photoelectrochemical cells by coupling to photonic crystals. *J Phys Chem B* **109,** 6334-6342 (2005)

64. Norris, D. J. & Vlasov, Y. A. Chemcial approaches to three-dimensional semiconductor photonic crystals. *Adv Mater* **13,** 371-376 (2001)

65. Vlasov, Y. A., Bo, X. Z., Sturm, J. C. & Norris, D. J. On-chip natural assembly of silica photonic bandgap crystals. *Nature* **414,** 289-293 (2001)

66. Hynninen, A. P., Thijssen, J. H. J., Vermolen, E. C. M., Dijkstra, M. & van Blaaderen, A. Self-assembly route for photonic crystals with a bandgap in the visible region. *Nat Mater* **6,** 202-205 (2007)

67. Holtz, J. H. & Asher, S. A. Polymerized colloidal crystal hydrogel films as intelligent chemical sensing materials. *Nature* **389,** 829-832 (1997)

68. Velev, O. D. & Kaler, W. In situ assembly of colloidal particles into miniaturized biosensors. *Langmuir* **15,** 3693-3698 (1999)

69. Joannopoulos, J. D., Villeneuve, P. R. & Fan, S. Photonic crystals: putting a new twist on light. *Nature* **1997**, 143-149 (1997)

70. Yamasaki, T. & Tsutsui, T. Spontaneous emission from fluorescent molecules embedded in photonic crystals consisting of polystyrene microspheres. *Appl Phys Lett* **72,** 1957-1959 (1998)

71. Yang, S. M., Jang, S. G., Choi, D. G., Kim, S. & Yu, H. K. Nanomachining by colloidal lithography. *Small* **2,** 458-475 (2006)

72. Arora, A. K**. &** Tata, B. V. R. *Ordering and Phase Transitions in Colloidal Systems* VCH, Weinheim (1996)

73. Pieranski, P. Colloidal crystals. *Contemp Phys* **24,** 25-73 (1983)

74. Van Negen, W. & Shook, I. *Adv Colloid Interface Sci* **21,** 119 (1984)

75. Asher, S. A., Flaugh, P. L. & Washinger, G. Crystalline Colloidal Bragg Diffraction Devices: The Basis for a New Generation of Raman Instrumentation. *Spectroscopy* **1,** 26-31 (1986)

76. Flaugh, P. L., Donnell, S. E. O. & Asher, S. A. Development of a new optical wavelength rejection filter: Demonstration of its utility in raman spectroscopy. *Appl Spectrosc* **38,** 847-850 (1984)

77. Carlson, R. J. & Asher, S. A. Characterization of optical diffraction and crystal structure in monodosperse polystyrene colloids. *Appl Spectrosc* **38,** 297-304 (1984)

78. VanWinkle, D. H. & Murray, C. A. Layering Transitions in Colloidal Crystals as Observed by Diffraction and Direct Lattice Imaging. *Phys Rev A* **34,** 562-573 (1986)

79. Pieranski, P., Strzelecki, L. & Pansu, B. Thin colloidal crystals. *Phys Rev Lett* **50,** 900-903 (1983)

80. Neser, S., Bechinger, C., Leiderer, P. & Palberg, T. Finite-Size Effects on the Closest Packing of Hard Spheres. *Phys Rev Lett* 79, 2348-2351 (1997)

81. Park, S. H., Qin, D. & Xia, Y. Crystallization of Mesoscale Particles over Large Areas. *Adv Mater* **10,** 1028-1032 (1998)

82. Park, S. H. & Xia, Y. Assembly of Mesoscale Particles over Large Areas and Its Application in Fabricating Tunable Optical Filters. *Langmuir* **15,** 266-(1999)

83. Gates, B., Qin, D. & Xia, Y. Assembly of Nanoparticles into Opaline Structures over Large Areas. *Adv Mater* **11**, 466-469 (1999)

84. Solomentsev, Y., Bohmer, M. & Anderson, J. L. Particle Clustering and Pattern Formation during Electrophoretic Deposition: A Hydrodynamic Model. *Langmuir* **13,** 6058-6068 (1997)

85. Born M. & Wolf, E. *Principles of Optics* (Cambridge Univ. Press, Cambridge, 1999)

86. Joannopoulos, J. D., Johnson, S. G., Winn, J. N. & Meade, R. D. *Photonic Crystals: Molding The Flow of Light* (Princeton University Press, Princeton, 2008)

87. Yeh, P. *Optical Waves in Periodic Media* (Wiley, New York, 1988)

88. Pendry J. B. & Mackinnon, A. Calculation of photon dispersion relations. *Phys Rev Lett* **69**, 2772-2775 (1992)

89. Bell, P. M., Pendry, J. B., Moreno, L. M. & Ward, A. J. A program for calculating photonic band structures and transmission coefficients of complex structures. *Comput Phys Commun* **85,** 306-322 (1995)

90. Yee, K. S. Numerical Solution of Initial Boundary Value Problems involving Maxwell's Equations in Isotropic Media. *IEEE Trans Antennas Propag* **Ap-14,** 302-307 (1966)

91. Taflove A. & Hagness, S. C. *Computational Electrodynamics: The Finite-Difference Time Domain Method* (Artech House, Norwood, MA, 2000).

92. Banerjee, S. & Dong, Z. Optical characterization of iridescent wings of Morpho butterflies using a high accuracy nonstandard finite-difference time-domain algorithm. *Opt Rev* **14**, 359-361 (2007).

93. Noh, H. *et al.* How Noniridescent Colors Are Generated by Quasi-ordered Structures of Bird Feathers. *Adv Mater* **22**, 2871-2880 (2010).

94. Kinoshita, S. *Structural colors in the realm of nature*. (world scientific publishing Co., singapore, 2008).

95. Tabata, H., Kumazawa, K., Funakawa, M., Takimoto, J. & Akimoto, M. Microstructures and optical properties of scales of butterfly wings. *Opt Rev* **3**, 139-145 (1996).

96. Pirih, P., Arikawa, K. & Stavenga, D. G. An expanded set of photoreceptors in the Eastern Pale Clouded Yellow butterfly, Colias erate. *J Comp Physiol A* **196**, 501-517 (2010).

97. Sweeney, A., Jiggins, C. & Johnsen, S. Insect communication: Polarized light as a butterfly mating signal. *Nature* **423**, 31-32 (2003).

98. Arsenault, A. C., Miguez, H., Kitaev, V., Ozin, G. A. & Manners, I. A polychromic, fast response metallopolymer gel photonic crystal with solvent and redox tunability: A step towards photonic ink (P-Ink). *Adv Mater* **15**, 503-507 (2003).

99. Labhart, T., Baumann, F. & Bernard, G. D. Specialized ommatidia of the polarization-sensitive dorsal rim area in the eye of monarch butterflies have non-functional reflecting tapeta. *Cell Tissue Res* **338**, 391-400 (2009).

100. Bernhard, C. (New York: Pergamon, 1965).

101. Brown, R. J. C., Brewer, P. J. & Milton, M. J. T. The physical and chemical properties of electroless nickel-phosphorus alloys and low reflectance nickel-phosphorus black surfaces. *J Mater Chem* **12**, 2749-2754 (2002).

102. Vukusic, P., Wootton, R. J. and Sambles, J. R. Remarkbale iridescence in the hindwings of the damselfy *Neurobasis chinensis chinensis* (Linnaeus) *Proc R Soc Lond* **271,** 595-601 (2004).

103. Vukusic, P., Sambles, J. R. & Lawrence, C. R. Structurally assisted blackness in butterfly scales. *P Roy Soc Lond B Bio* **271**, S237-S239 (2004).

104. Macleod, H. A. (Philadephia, PA: Institute of Physics Pub., Bristol, 2001).

105. Vasicek, A. *Optics of thin films* (New York, Interscience Publisher, 1960).

106. Lim, M. L. M., Land, M. F. & Li, D. Q. Sex-specific UV and fluorescence signals in jumping spiders. *Science* **315**, 481-481 (2007).

107. Briscoe, A. D. *et al.* Positive selection of a duplicated UV-sensitive visual pigment coincides with wing pigment evolution in Heliconius butterflies. *P Natl Acad Sci USA* **107**, 3628-3633 (2010).

108. Takeuchi, Y., Arikawa, K. & Kinoshita, M. Color discrimination at the spatial resolution limit in a swallowtail butterfly, Papilio xuthus. *J Exp Biol* **209**, 2873-2879 (2006).

109. Zi, J. *et al.* Coloration strategies in peacock feathers. *P Natl Acad Sci USA* **100**, 12576-12578 (2003).

110. Diao, Y. Y. & Liu, X. Y. Mysterious coloring: structural origin of color mixing for two breeds of *Papilio* butterflies *Opt Express* **19**, 9232-9241 (2011).

111. Du, N. *et al.* Design of superior spider silk: From nanostructure to mechanical properties. *Biophys J* **91**, 4528-4535 (2006).

112. Gupta, M. K. *et al.* A Facile Fabrication Strategy for Patterning Protein Chain Conformation in Silk Materials. *Adv Mater* **22**, 115-119 (2010).

113. Vollrath, F. & Knight, D.P. Liquid crystalline spinning of spider silk. *Nature* **410**, 541-548 (2001).

114. Economou, E. N. & Sigalas, M. M. Classical Wave-Propagation in Periodic Structures - Cermet Versus Network Topology. *Phys Rev B* **48**, 13434-13438 (1993).

115. Ashcroft, N. W. & Mermin, N. D. *Solid State Physics* (New York, 1976).

116. Lawrence, B. D., Cronin-Golomb, M., Georgakoudi, I., Kaplan, D. L. & Omenetto, F. G. Bioactive silk protein biomaterial systems for optical devices. *Biomacromolecules* **9**, 1214-1220 (2008).

117. Bogomolov, V. N. *et al.* Photonic band gap phenomenon and optical properties of artificial opals. *Phys Rev E* **55**, 7619-7625 (1997).

118. Vos, W. L. *et al.* Strong effects of photonic bands structures on the diffraction of colloidal crystals. *Phys Rev B* **53**, 16231-16235 (1996).

119. Vos, W. L. & van Driel, H. M. Higher order Bragg diffraction by strongly photonic fcc crystals: onset of a photonic bandgap. *Phys Lett A* **272**, 101-106 (2000).

120. Johnson, N. P., McComb, D. W., Richel, A., Treble, B. M. & De la Rue, R. M. Synthesis and optical properties of opal and inverse opal photonic crystals. *Synthetic Met* **116**, 469-473 (2001).

121. Nakamae, K., Nishino, T. & Ohkubo, H. Elastic-Modulus of the Crystalline Regions of Silk Fibroin. *Polymer* **30**, 1243-1246 (1989).

122. Wang, D. Y. & Caruso, F. Fabrication of polyaniline inverse opals via templating ordered colloidal assemblies. *Adv Mater* **13**, 350-353 (2001).

123. Perry, H., Gopinath, A., Kaplan, D. L., Dal Negro, L. & Omenetto, F. G. Nano- and micropatterning of optically transparent, mechanically robust, biocompatible silk fibroin films. *Adv Mater* **20**, 3070-3072 (2008).

124. Omenetto, F. G. & KapLan, D. L. A new route for silk. *Nat Photonics* **2**, 641-643 (2008).

125. Gobin, A. S., Froude, V. E. & Mathur, A. B. Structural and mechanical characteristics of silk fibroin and chitosan blend scaffolds for tissue regeneration. *J Biomed Mater Res A* **74A**, 465-473 (2005).

126. Schmidt, C. & Petsitis, X. Interference effect pigments – new technologies in cosmetics products. *SOFW- Journal* **136**, 42-48 (2010).

127. Liu, X. Y. & Diao, Y. Y. *Light-reflective structures and methods for their manufacture and use.* SG - 810110-01-SG-PCT (2011).

128. Sah, M. K., Pramanik, K. Regenerated Silk Fibroin from B. mori Silk Cocoon for Tissue Engineering Applications. *IJESD*, **1,** 404-408 (2010)

129. Ge, J. P. & Yin, Y. D. Responsive photonic crystals. *Angew Chem Int Ed* **50**, 1492-1552 (2011)

130. Ge, J., Hu, Y. & Yin, Y. D. Highly Tunable Superparamagnetic Colloidal Photonic Crystals. *Angew Chem* **119,** 7572-7575 (2007)

131. Saito, H., Takeoka, Y. & Watanabe, M. Simple and precision design of porous gel as a visible indicator for ionic species and concentration. *Chem. Commun* 2126-2127 (2003)

132. Takeoka, Y. & Watanabe, M. Tuning Structural Color Changes of Porous Thermosensitive Gels through Quantitative Adjustment of the Cross-Linker in Pre-gel Solutions. *Langmuir* **19,** 9104-9106 (2003)

133. Rowlands, A. The influence of water and light upon the color change of sightless frogs (Rana temporaria). *J Exp Biol* **1,** 127–136 (1952)

134. Tattersall, G. J., Eterovick, P. C. & de Andrade, D. V. Tribute to R. G. Boutilier: skin color and body temperature changes in basking Bokermannohyla alvarengai (Bokermann 1956). *J Exp Biol* **209,** 1185–1196 (2006)

135. Hadley, N. F. Wax secretion and color phases of the desert Tenebrionid beetle Cryptoglossa verrucosa (LeConte). *Science* **203,** 367-369 (1979)

136. McClain, E., Seely, M. K., Hadley, N. F. & Gray, V. Wax blooms in Tenebrionid beetles of the Namib desert: correlations with environment. *Ecology* **66,** 112–118 (1985)

137. Hinton, H. E. & Jarman, G. M. Physiological color change in the Hercules Beetle. *Nature* **238,** 160–161(1972)

138. Vigneron, J. P. et.al. Switchable reflector in the Panamanian tortoise beetle Charidotella egregia (Chrysomelidae: Cassidinae). *Phys. Rev. E.* **76,** 031907 (2007)

139. Hanlon, R. T., Cooper, K. M., Budelmann, B. U. & Pappas, T. C. Physiological color change in squid iridophores I. Behavior, morphology and pharmacology in Lolliguncula brevis. *Cell Tissue Res* **259,** 3–14 (1990)

140. Cooper, K. M., Hanlon, R. T. & Budelmann, B. U. Physiological color change in squid iridophores II. Ultra structural mechanisms in Lolliguncula brevis. *Cell Tissue Res* **259,** 15–24 (1990)

141. M¨athger, L. M. & Denton, E. J. Reflective properties of iridophores and fluorescent 'eyespots' in the loliginid squid Alloteuthis subulata and Loligo vulgaris. *J Exp Biol* **204,** 2103–2118 (2001)

142. M¨athger, L. M., Land, M. F., Siebeck, U. E., & Marshall, N. J. Rapid color changes in multilayer reflecting stripes in the paradise whiptail, Pentapodus paradiseus. *J Exp Biol* **206,** 3607–3613 (2003)

143. Liu, Y., Shao, Z. Z. & Vollrath, F. Relationships between supercontraction and mechanical properties of spider silk. *Nat Mater* **4,** 901-905 (2005)

144. Gosline, J.M., Denny, M.W. & DeMont, M.E. Spider silk as rubber. *Nature* **309,** 551-552 (1984)

145. Yang, Z. T. et al., Supercontraction and backbone dynamics in spider silk: C-13 and H-2 NMR studies. J *Am Chem Soc 122, 9019-9025 (2000)*

146. Blackledge, T.A., et al. How super is supercontraction? Persistent versus cyclic responses to humidity in spider dragline silk. *J Exp Biol*, **212**, 1980-1988 (2009)

147. Jelinski, L. W. *et al.* Orientation, structure, wet-spinning, and molecular basis for supercontraction of spider dragline silk. *International Journal of Biological Macromolecules* **24**, 197-201 (1999)

148. Gosline, J. M., Guerette, P. A., Ortlepp, C. S. & Savage, K. N. The mechanism design of spider silks: from fibroin sequence to mechanicam function. *J. Exp.Biol.* ***202,*** 3295-3303 (1999)

149. Agnarsson, I., Dhinojwala, A., Sahni, V. & Blackledge, T. A. Spider silk as a novel high performance biomimetic muscle driven by humidity. *Journal of Experimental Biology* **212**, 1989-1993 (2009)

150. Friend, R. H. er al. Electroluminescence in conjugated polymers. *Nature* **397,** 121-128 (1999).

151. Tang C. W. & VanSlyke, S. A. Organic electroluminescent diodes. *Appl Phys Lett* **51**, 913 (1987).

152. Chan, L. H., Lee, R. H., Hsieh, C. F., Yeh, H. C. & Chen, C. T. Optimization of high-performance blue organic light-emitting diodes containing tetraphenylsilane molecular galss materials. *J Am Chem Soc* **124**, 6469-6479 (2002).

153. Mitschke, U. & Ba ̈uerle, P. The electroluminescence of organic materials. *J Mater Chem* **10**, 1471-1507 (2000).

154. Andrew, P. & Barnes, W. L. Energy transfer across a metal film mediated by surface plasmon polaritons. *Science,* **306**, 1002-1005 (2004)

155. Willard, D. M., Carillo, L. L., Jung, J. & Orden, A. V. CdSe−ZnS Quantum Dots as Resonance Energy Transfer Donors in a Model Protein−Protein Binding Assay. *Nano Lett.*, **1**, 469-474 (2001)

156. Maenosono, S., Modeling photoinduced fluorescence enhancement in semiconductor nanocrystal arrays. *Chem Phys Lett* **376**, 666-670 (2003)

157. Uematsu, T., Maenosono, S., & Yamaguchi, Y. Photoinduced Fluorescence Enhancement in Mono- and Multilayer Films of CdSe/ZnS Quantum Dots: Dependence on Intensity and Wavelength of Excitation Light. *J Phys Chem B* **109**, 8613-8618 (2005)

158. Hayakama, T., Furuhashi, K. & Nogami, M. Enhancement of 5D0-7FJ emissions of $Eu3^{+}$ ions in the vicinity of polymer-protected Au nanoparticles in sol−gel-derived B_2O_3−SiO_2 glass. *J Phys Chem B* **108**, 11301-11307 (2004)

159. Mohamed, M. B., Volkov, V., Link, S. & El-Sayed, M. A. The lightning gold nanorods: fluorescence enhancement of over a million compared to the gold metal. *Chem Phys Lett* **317**, 517-523 (2000)

160. Zhang, Y. Q. et.al. Solid-state fluorescence enhancement of organic dyes by photonic crystals. *J. Mater. Chem.*, **17**, 90-94 (2007)

161. Ganesh, N. et.al. Enhanced fluorescence emission from quantum dots on a photonic crystal surface. *nature nanotechnology* 2, 515-520 (2007).

162. Fujita, M., Takahashi, S., Tanaka, Y., Asano, T. & Noda, S. Simultaneous inhibition and redistribution of spontaneous light emission in photonic crystals. *Science* 308, 1296–1298 (2005).

163. Fujita, M., Takahashi, S., Tanaka, Y., Asano, T. & Noda, S. Simultaneous Inhibition and Redistribution of Spontaneous Light Emission in Photonic Crystals. *Science*, **308**, 1296-1298 (2005)

164. Wei, C., Liu, S., Deng, D. & Shen, J. Electrical field enhancement in guilded-mode resonance filters. *Opt Lett* **31**, 1223-1225 (2006)

165. Whittaker, D. M. Inhibited emission in photonic woodpile lattices. *Opt Lett* **25**, 779-781 (2000)

166. Ogawa, S., Imada, M., Yoshimoto, S., Okano, M. & Noda, S. Control of light emission by 3D photonic crystals. *Science* **305**, 227-229 (2004)

167. Ye, J. Y., Ishikawa, M., Yamane, Y., Tsurumachi, N. & Nakatsuka, H., Enhancement of two-photon excited fluorescence using one-dimensional photonic crystals. *Appl. Phys. Lett.* **75,** 3605 (1999)

168. Ryu, H. Y., Lee,Y. H., Sellin, R. L. & Bimberg, D. Over 30-fold enhancement of light extraction from free-standing photonic crystal slabs with InGaAs quantum dots at low temperature. *Appl. Phys. Lett.* **79,** 3573 (2001)

169. Maskaly, G. R. *et.al.* Amplified Spontaneous Emission in Semiconductor-Nanocrystal/Synthetic-Opal Composites: Optical-Gain Enhancement via a Photonic Crystal Pseudogap. *Adv. Mater.* **18,** 343-347 (2006)

170. Ganesh, N. *et.al.* Ehanced fluorescence emission from quantoum dots on a photonic crystal surface. *Nature Nanotechnology* **2,** 515-520 (2007)

171. Wang, X., Kluge, J. A., Leisk, G. G. & Kaplan, D. L. Soft tissue augmentation using silk gels: An in vitro and in vivo study. *Biomaterials* **29,** 1054–1064 (2008).

172. Kim, U. J. et al. Structure and properties of silk hydrogels. *Biomacromolecules* **5,** 786–792 (2004).

173. Wei, C., Liu, S., Deng, D. & Shen, J. Electrical field enhancement in guild-mode resonance filters. *Opt Lett* **31,** 1223-1225 (2006)

174. Zhang, W., Ganesh, N., Mathias, P. C. & Cunningham, B. T. Enhanced Fluorescence on a Photonic Crystal Surface Incorporating Nanorod Structures. *Small* **4,** 2199-2203 (2008)

175. Jiang, C. H. et.al. Mechanical properties of robust ultrathin silk fibroin films. *Adv Func Mater* **17,** 2229-2237 (2007)

176. Jiang, P., Bertone, J. F., Hwang, K. S. & Colvin, V. L. Single-Crystal Colloidal Multilayers of Controlled Thickness. *Chem Mater* **11**, 2132-2140 (1999)